

ISSN 1880-8468

Technical Report of  
International Development Engineering  
国際開発工学報告

TRIDE-2007-01

February 1, 2007

Abstracts of Master Theses  
Presented in February 2007

Department of International Development Engineering,  
Graduate School of Science and Engineering,  
Tokyo Institute of Technology  
<http://www.ide.titech.ac.jp/TR>

# Technical Report of International Development Engineering

TRIDE-2007-01

## Table of Contents

Effect of preparation condition applied by Chevrel phase sulfides synthesis on the hydrosulfurization activity of new developing catalysts .....	Masakazu KURATA	1
Introduction of ICT (information and communication technology) to the world heritage site in developing countries – Case study of Luang Prabang Lao PDR – .....	Nobuo OOKA	5
Study of text classification with statistical pattern recognition method .....	Yusuke WATADA	9
Extraction of liquid organic multi-component mixture with ionic liquids as solvents .....	Kenya AKAISHI	13
Moving picture coding with wavelet transform .....	Takashi OHTA	17
Creation and evaluation of e-Learning materials for introduction of engineering .....	Masanori KANEKO	21
Study on applicability of steel slag hydrated matrix to steel reinforced members under marine environment .....	Tomonari KIMURA	25
A study on gas-liquid two-phase flow patterns in rectangular micro-channels .....	Shintaro KOBAYASHI	29
In-situ soil remediation by sedimentation method – Heavy metal ions' adsorption characteristics on soil and adsorbents – .....	Ryoichi SUGA	33
The psychological effects of behavioral change caused by public works on place attachment .....	Haruna SUZUKI	37

<b>A procedure of determining parameters by adapting to the results calculated by MEAM' 92</b>	Kento TOKUMARU	41
<b>Long term prediction of strength deterioration due to Ca leaching from cement treated soil</b>	Katsufumi HASHIMOTO	45
<b>Analysis of turbulent organized structures at the urban outdoor scale model(COSMO)</b>	Satoshi HIROOKA	49
<b>Efficiency of the implicit finite element method of geotechnical engineering</b>	Takahiro FURUMURA	53
<b>Synthesis of zeolites from lake sludge</b>	Wei QU	57
<b>Influence of creep phenomenon on manipulation by shape control of rubber- elastic membrane</b>	Xuanxuan CHANG	61
<b>Development of a stored channel model for UWB link level system design and evaluation</b>	Huynh Thi thanh TRIEU	65
<b>Numerical simulation on temperature field for Newtonian fluid enclosed in concentric sphere</b>	Bian HU	69
<b>A Study on corrosion of paint-coated steel with defects in marine environment</b>	Aung Kyaw MIN	73
<b>Study on antennas embedded in mobile phone housing</b>	Jeonghoon HAN	77

# Effect of preparation condition applied by Chevrel phase sulfides synthesis on the hydrodesulfurization activity of new developing catalysts

Student number:04M18104 Name: Masakazu KURATA Supervisor: Hirofumi HINODE

## シェブレル相硫化物合成法を応用した新規水素化脱硫触媒の研究

倉田 雅一

本研究ではシェブレル相硫化物合成法を応用して調製したサンプルの水素化脱硫活性を評価した。750°C で水素化処理を行ったサンプルは水素化時間の増加と共に活性が減少したが、450°C で水素化処理を行ったサンプルは水素化時間の増加と共に活性が増大し、水素化 24 時間以上では市販の工業触媒を上回る活性を示した。XRD、BET、TEM の結果から水素化時間 750°C のサンプルでは熱劣化及び結晶化が起り、水素化時間 450°C のサンプルでは活性相である CoMoS 相の量が促進されたことが確認できた。

### 1. Introduction

Sulfur removal in gasoline and diesel oil is now strongly desirable because sulfur may adversely affect catalytic performance for exhaust emission treatment. So worldwide refiners are trying to provide clean transportation fuels to meet increasingly demanding environmental regulations. Hydrodesulfurization (HDS) is sulfur compounds removal process of petroleum feedstocks in petroleum refiners. Now numerous attempts have already been made to develop more active HDS catalyst.

In the last half centuries, alumina supported Co-Mo, Ni-Mo, Ni-W sulfides catalysts were widely used as HDS catalyst. Active site of conventional CoMo sulfides catalyst is the so-called CoMoS phase, in which Co is located on the edges of highly dispersed MoS<sub>2</sub> slabs<sup>1)</sup>. MoS<sub>2</sub> edge plane has two planes, rim plane and edge plane. Rim plane has both HDS and hydrogenation (HYD) ability, while edge plane has only HDS ability<sup>2)</sup>. There are two types of CoMoS phase, Type I and Type II. Type I is related to highly dispersed single MoS<sub>2</sub> slab maintaining their interactions with the support thus is less activity. Type II is related to less dispersed multi MoS<sub>2</sub> slabs with less interaction with support, resulting in high activity.

In this research, samples were prepared using methods applied by Chevrel phase sulfides (CPS) synthesis<sup>3)</sup>. CPS are ternary molybdenum sulfides and have the general formula M<sub>x</sub>Mo<sub>6</sub>S<sub>8-y</sub>, where M represents ternary metal, one of about forty metal<sup>4)</sup>. Previous study showed supported CPS had a high activity<sup>5,6)</sup>, and we presumed that CPS and M-Mo-S phase of active site for commercial catalysis is similar structure. On the other hand,

the hydrogenation of supported CPS needed to be done at high temperature for a few days.

In this research, the effect of preparation conditions, in particular, hydrogenating time and temperature, on HDS activity and the characterization of supported Chevrel phase sulfides have been investigated.

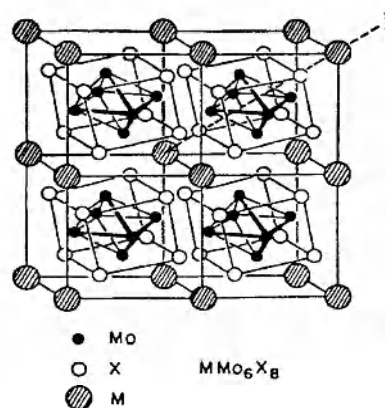


Figure 1 Structure of Chevrel phase sulfides

### 2. Experimental

Supported CoCPS catalysts were prepared by impregnation method. Precursors of the catalyst were Co(NO<sub>3</sub>)<sub>2</sub>·6H<sub>2</sub>O and (NH<sub>4</sub>)<sub>6</sub>Mo<sub>7</sub>O<sub>24</sub>·4H<sub>2</sub>O (Wako Pure Chemical Industries, Ltd.). JRC-ALO2 (Al<sub>2</sub>O<sub>3</sub>, Reference Catalyst, Catalysis Society of Japan) was used as a support. The Mo loading level was fixed at 15wt%. Co/Mo ratio was 0.28. In the first step, JRC-ALO2 was impregnated with precursors aqueous solution for 24h. Then, the impregnated sample was dried up, and calcined at 500°C for 4h. The sample was

pelletized, crushed, and sieved to 0.71~1.00mm in order to reduce pressure drop. In the second step, sulfurization was carried out at 400°C for 2h under 10% H<sub>2</sub>S/H<sub>2</sub> flow in order to prepare sulfides. The hydrogenation was then carried out under H<sub>2</sub> flow at 450°C or 750°C for 0-72h.

Commercial catalyst (Nippon Ketjen Co., Ltd., KF 752-1.5E) was pelletized, crushed, and sieved to 0.71~1.00mm, and then sulfurized at 400°C for 2h under 10% H<sub>2</sub>S/H<sub>2</sub> flow.

HDS reaction was carried out in a fixed-bed flow reactor under atmospheric pressure<sup>4)</sup>. 0.2g of the sample was packed in the reactor and the total flow rate of the feed mixture gas was fixed at 20ml/min. Thiophene was used as a target material of sulfur compounds. The concentration of thiophene in the feed stream was maintained at 2.1mol%. The reaction temperature was selected at 300 and 350°C. Thiophene was quantitatively analyzed by GC-MS (Shimadzu Corp., QP5050A), and HDS activity and selectivity of products were calculated.

The samples were characterized by XRD (Rigaku Co., MutiFlex), BET specific surface area measurement (COULTER Co., SA3100) and TEM (JEOL Ltd., JEM-2010F).

### 3. Result and Discussion

Figure 2 shows thiophene conversion of CoCPS/ALO<sub>2</sub> hydrogenating at 750°C with different hydrogenating time. Thiophene conversions of samples decreased with an increase in hydrogenating time. Thiophene conversions at 300°C and 350°C of not hydrogenated sample were 79.63% and 96.34%, respectively, and those of hydrogenated for 24h were 53.05% and 76.82%, respectively.

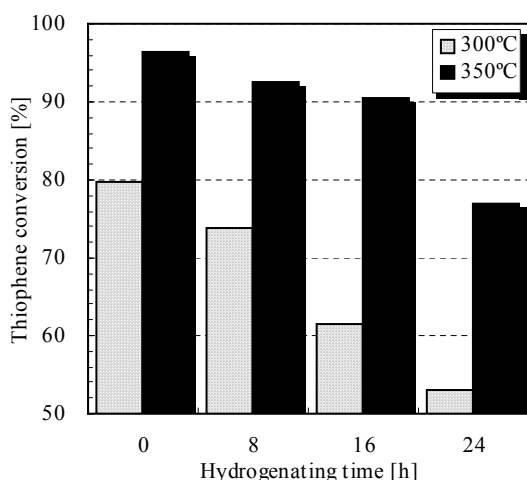


Figure2 Thiophene conversion of CoCPS/ALO<sub>2</sub> hydrogenated at 750°C with different hydrogenating time

Figure 3 shows thiophene conversion of CoCPS/ALO<sub>2</sub> hydrogenating at 450°C with different hydrogenating time. Thiophene conversion of the samples increased with an increase in hydrogenating time, and sample of hydrogenated for 48h showed thiophene conversion at 300 and 350°C of 96.4% and 99.4%, respectively. There was, however, a slight decrease in the thiophene conversion of sample hydrogenated for 72h compared to that of 48h.

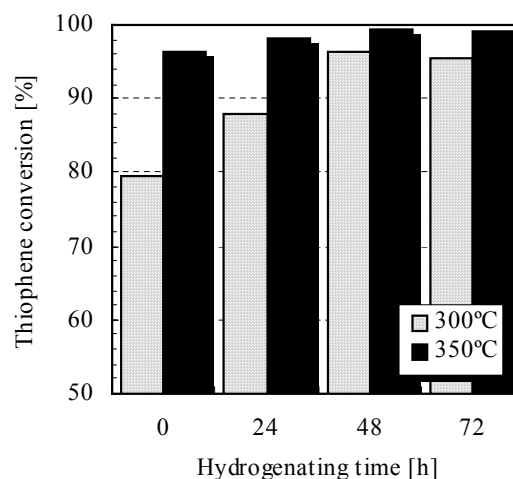


Figure3 Thiophene conversion of CoCPS/ALO<sub>2</sub> hydrogenated at 450°C with different hydrogenating time

Figure 4 shows thiophene conversion of commercial CoMoS catalyst samples with different hydrogenation temperature and time. H0 means not hydrogenated sample, and H450 and H750 mean hydrogenation for 24h at 450 and 750°C, respectively. Thiophene conversions of H450 sample were higher than those of commercial CoMoS catalyst.

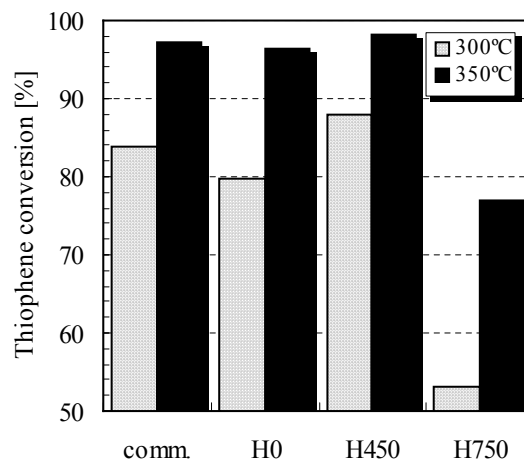


Figure 4 Thiophene conversions of commercial CoMoS catalyst and H0, H450, and H750

Figure 5 shows XRD patterns of H0, H450 and H750 samples. XRD pattern of H750 sample showed clearly peaks of  $\text{MoS}_2$  at  $2\theta = 14.38^\circ(002)$ ,  $32.68^\circ(100)$ ,  $33.51^\circ(101)$ ,  $58.33^\circ(110)$  or/and CoCPS at  $2\theta = 13.78^\circ(101)$ ,  $33.58^\circ(122)$ , and the peaks of JRC-ALO2 ( $2\theta = 38^\circ$ ,  $46^\circ$ , and  $67^\circ$ ). According to XRD patterns of H450 and H0 samples showed small peaks at  $2\theta = 33^\circ$  and  $58^\circ$ . From the XRD pattern,  $\text{MoS}_2$  or/and CoCPS well crystallized in H750 sample.

Figure 6 shows TEM image of H750 sample. 2 or 3 slabs and large  $\text{MoS}_2$  crystals were observed in this image.

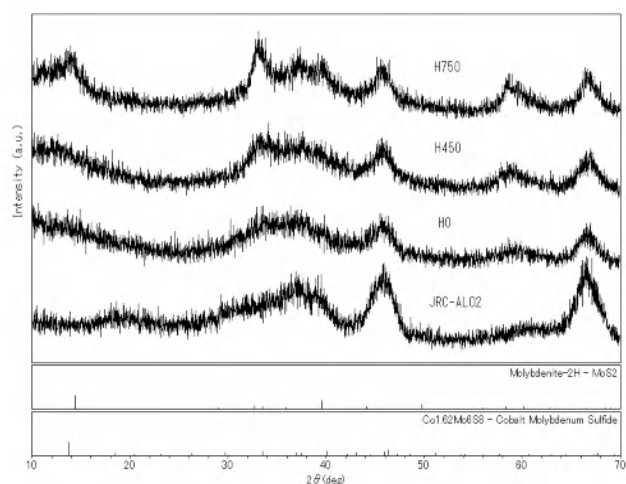


Figure 5 XRD patterns of H0, H450, and H750 samples and JRC-ALO2

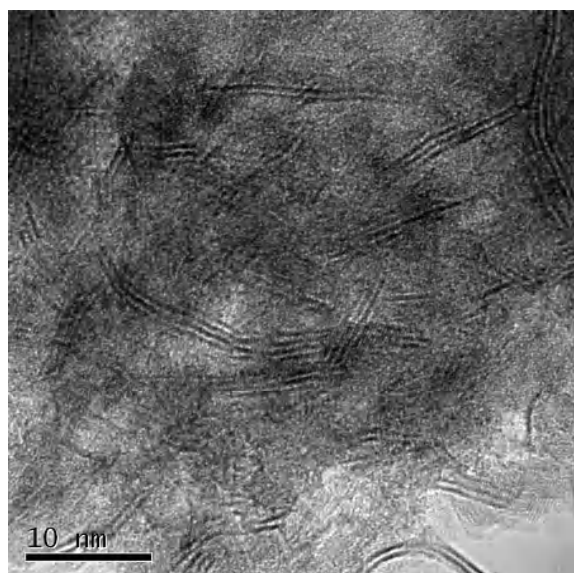


Figure 6 TEM image of H750 sample

Table 1 shows specific surface area of H0, H450 and H750 samples. Specific surface areas of H0 and H450 were almost the same, while that of H750 sample was significantly smaller than those

of other samples. Due to hydrogenating at high temperature, specific surface area of H750 sample considerably decreased.

Table 1 Specific surface area of H0, H450 and H750

Sample	Specific surface area
H0	202.18m <sup>2</sup> /g
H450	197.72m <sup>2</sup> /g
H750	154.31m <sup>2</sup> /g
JRC-ALO2	280.10m <sup>2</sup> /g

For these reason, low activity of H750 sample was attributed to increased crystallinity and decreased specific surface area.

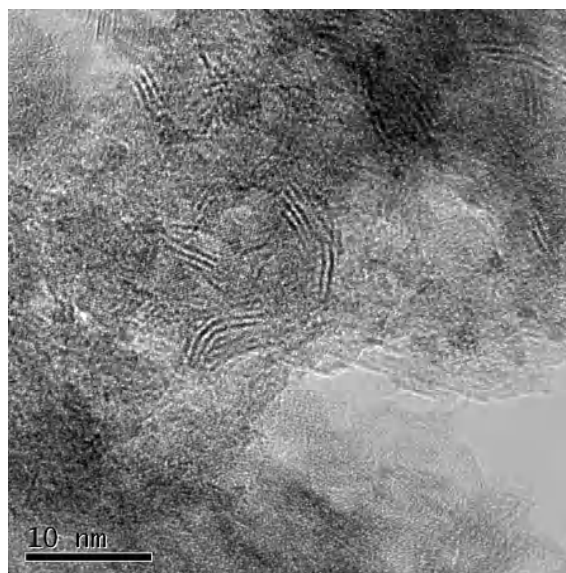


Figure 7 TEM image of H0 sample

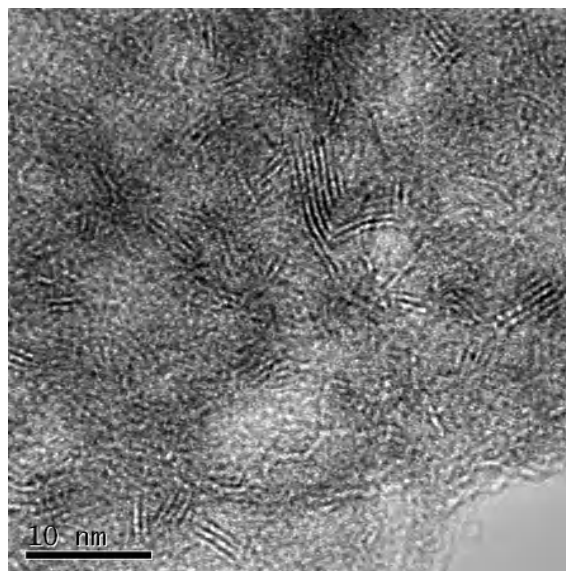


Figure 8 TEM image of H450 sample

Differences between H0 and H450 samples were not identified by XRD patterns and specific surface areas. On the other hand, TEM images of both samples, H0 in Figure 7 and H450 in Figure 8 show remarkable difference. H0 sample in Figure 7 had only 2-4 slabs, so CoMoS phase of H0 sample was mainly Type I and had less activity. As shown in Figure 8, H450 sample had 3-8 slabs, so CoMoS phase of H450 sample was mainly Type II and had high activity. For this reason, hydrogenating at 450°C promoted the formation of CoMoS Type II phase.

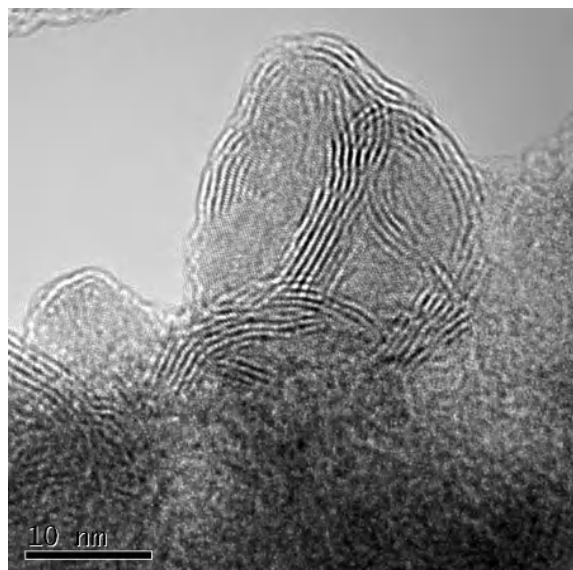


Figure 9 TEM image of commercial CoMoS catalyst<sup>8)</sup>

In order to measure the HYD activity of the samples, selectivity of the products was measured. 1-butene, trans-2-butene, cis-2-butene and n-butane were detected. Table 2 shows selectivity for H0 and H450 samples. H450 sample was higher HDS activity than H0 sample, and also H450 sample was higher HYD activity than H0 sample. These can be explained according to the particle size of MoS<sub>2</sub> slabs, since MoS<sub>2</sub> particle size is correlated with the amount of rim and edge planes<sup>7)</sup>. H450 sample in Figure 8 showed small particle size of MoS<sub>2</sub> slabs compared to commercial CoMoS catalyst shown in Figure 9<sup>8)</sup> indicating formation of rim plane mainly. Therefore, H450 sample had a high HYD activity.

Table 2 Products selectivities of H0 and H450 samples

Sample	Butane	Butenes
H0	71.80%	28.20%
H450	75.36%	24.64%

#### 4. Conclusion

Thiophene conversion of hydrogenated at 750°C samples decreased with an increase in hydrogenating time, due to increased crystallinity and decreased specific surface area of the sample. On the other hand, thiophene conversion of hydrogenated at 450°C samples increased with an increase in hydrogenating time, due to the formation of CoMoS Type II. Hydrogenated at 450°C samples had higher HDS activity than commercial CoMoS catalyst. H450 sample has a high HYD activity because of the formation of rim plane mainly.

#### Reference

- [1] H.Topsøe et al., *Bull.Soc.Chim.Belg.*, **90**, 1189 (1981)
- [2] M.Daage et al., *J.Catal.*, **149**, 414 (1994)
- [3] R.Chevrel et al., *J.Solid.State Chem.*, **3**, 519 (1971)
- [4] G.J.Dudly et al., *J.Solid.State Chem.*, **32**, 259 (1980)
- [5] V.Harel-Michaud et al., *J.Alloys.Comp.*, **317-318**, 195 (2001)
- [6] S.Ooi et al., *React.Kinet.Catal.Lett.*, **82**, 89 (2004)
- [7] A.Nishijima et al., *Sekiyugakkaishi*, **32**, 35 (1989)
- [8] H.Zhang. Master's thesis, Tokyo Institute of technology (2006)

# Introduction of ICT (Information and Communication Technology) to the World Heritage Site in developing countries - Case study of Luang Prabang, Lao PDR -

Student Number: 04M51248 Name: Nobuo OOKA Supervisors: Jun-ichi TAKADA, Shinobu YAMAGUCHI

## 開発途上国の世界文化遺産地域における情報通信の導入

### -ラオス、ルアンパバーンにおけるケーススタディ-

大岡信夫

本論文では、ルアンパバーンにおいて現地政府・UNESCO との協働のもと行ってきたニーズアセスメントおよび、それをもとに実施したデータベース開発・現地人材育成・ICT センターの設置運営などの活動について報告する。また、実施を通して実現した、開発途上国の世界文化遺産を核にした持続可能な地域開発への ICT 分野での貢献を評価するとともに、その経験から持続可能性に対する留意事項を抽出した。

## 1 Introduction

Many development projects have been implemented in the developing countries, but in 1980s, many assistance projects faced the difficulties on the sustainability of their implementation. Then, sustainable development has been receiving a lot of attention. In other word, experts, government, and international organizations are very much concerned how development activities can be continued as a locally owned implementation. Through the experiences on the actually implemented activities in Luang Prabang, Lao PDR, this thesis presents the case study as one of the applicable example to contribute to the sustainable development in developing countries.

The town of Luang Prabang, inscribed into the UNESCO World Heritage Site in 1995, has experienced regional economic growth due to the increasing tourism. In order to promote sustainable regional development, it has been discussed how different sectors can be well-integrated for the regional development in Luang Prabang, such as transportation and infrastructure and communication technologies, education and health, commerce, agriculture and forestry and so on.

In the meanwhile, ICT development in developing countries has been considered as one of the important factors in the regional development since 1980s [1]. Based on the request from Lao government, since 2003 Tokyo Tech team has been taking a role on technical assistance to identify and provide appropriate and applicable ICT application in Luang Prabang. While the author has been involved in the needs assessment and its implementation at the local site, it has been focused how ICT can contribute to the heritage conservation and development.

In this thesis, chapter 2 covers the background information, and chapter 3 describes the current difficulties and needs in ICT area identified through the field survey. Then chapter 4 highlights actually implemented activities. According to the implementation, chapter 5 shows the observed impacts in the

field, and chapter 6 touches upon the further issues. Finally, chapter 7 discusses on the sustainability of the development activities through the experiences of the involvement in the field activities.

## 2 Background

### 2.1 Regional background

Lao PDR is a landlocked country in the Indochinese Peninsula and regarded as one of the underdeveloped countries with low GDP per capita (PPP) of \$1,969US<sup>1</sup> and low HDI (Human Development Indicator) of 0.553<sup>2</sup> which is 133rd out of 177 countries. Luang Prabang is the provincial capital of Luang Prabang province which is located northern Lao PDR. In 1995, the town of Luang Prabang was inscribed into UNESCO World Heritage site, due to its well-preserved townscape and natural environment. After the inscription, the number of tourists has been remarkably increasing; an average of 50,000–60,000 visitors in 1995 and 1996 per year has increased to 196,106<sup>3</sup> in 2003. Since the town of Luang Prabang is the second largest city in Lao PDR and is facing rapidly growing tourism, regional development including surrounding area, putting the heritage at the core, has been expected. Generally, it is often the case that the World Heritage inscription brings not only the positive impacts, such as increased income from tourist, more employment opportunities, improved infrastructure, promotion of community identity, and international cooperation and subsidy, but also negative impacts such as rapid and unplanned construction, environmental destruction, and increase of income gap. Therefore, in order to maximize the positive impacts with reducing negative impacts, it has been concerned to promote comprehensive approach integrating the various development components, such as economic development,

<sup>1</sup> Source: CIA, "The World Factbook – Laos", <https://www.cia.gov/cia/publications/factbook/geos/la.html>

<sup>2</sup> Source: UNDP, "Human Development Report 2006"

<sup>3</sup> Sources: ADUC, SCOT, November 2004; Luang Prabang, Provincial Tourism Office, 2004



environmental protection, human development, social development and so on.

## 2.2 Collaboration framework on the activities

In order to promote comprehensive approach in Luang Prabang, the Inter-institutional committee, so-called Local Heritage Committee (LHC) is organized. La Maison du Patrimoine (MdP) is one of the focal institutions in LHC, created in 1996 according to the UNESCO recommendation, mainly taking the role on rehabilitation and management of the cultural heritage property and natural heritage, development of market-place, and coordination of international projects. Meanwhile, the tripartite collaboration among Lao government, Tokyo Tech, and UNESCO has been held on ICT development area since late 2003, when Tokyo Tech participated in the inter-government symposium in Luang Prabang according to the request of UNESCO. The role of Tokyo Tech is to identify and provide the appropriate and locally applicable ICT application to contribute to the sustainable regional development in Luang Prabang. Especially in the field activities, Tokyo Tech has been in cooperation with MdP.

## 3 Needs analysis

### 3.1 Needs analysis

Based on the request from the local government, Tokyo Tech team conducted needs assessment in Luang Prabang in 2004. Through the field survey, the following five needs for ICT development were identified.

**Long-term storage of data:** There was abundant information accumulated through the heritage conservation and development, which was not only given the worth as heritage data, but also regarded as the valuable resource of the experiences in heritage management and urban development. However, most of information was not kept in good condition, being stored in paper-based. The appropriate condition to enable long-term storage was needed as the fundamental for effective information management.

**Utilization of stored information:** The stored paper-based data has had disadvantages in searching, updating, and sharing data. Recently, the effort to integrate DBMS (Database Management System) has been made by the local stuffs, but it was not so actively used as they expected because of lack of strategy and human resource. The effective tools which could enhance the utilization of stored data were needed.

**Information sharing:** In Luang Prabang, network infrastructure and information sharing framework were insufficient. In order to promote the comprehensive approach, the means to encourage intercommunication among institutions were required.

**Information provision to the public:** There was no facility where the population and visitors in Luang Prabang can access to the reliable information of the town, although awareness and

participation of local communities have been regarded as an important factor to promote the sustainable development. Also, having no official web site, Luang Prabang would have missed the potential interest of the global public including tourists, researchers, fund agency, business people and so on. Therefore, effective means to disseminate the public information to the various target groups were expected.

**Active reuse of restored architecture:** There have been a number of restored heritage architectures in Luang Prabang, but some of them have been under utilized. Not only conservation but also innovative reuse of heritage architectures was vital to promote benefits for the local communities and people.

### 3.2 Identified component for ICT development

According to the needs mentioned above, the following five components for ICT development shown in Figure 1 were proposed.

**1. Development of database application:** With well-structured database of digitalized data to enable long-term storage of data, and effective interfaces to fully utilize stored data.

**2. Establishment of network infrastructure:** To encourage the information sharing among institutions.

**3. Creation of Web sites:** To give the effective means to disseminate information to global public.

**4. Development and management of ICT centers:** To provide information to the public in Luang Prabang, and to promote reuse of the restored architectures.

**5. Human resource development:** Human resource is one of the essential factors to realize sustainable development [2]. Since there were no ICT professionals in Luang Prabang, continuous human resource development was required to implement and sustain the activities.

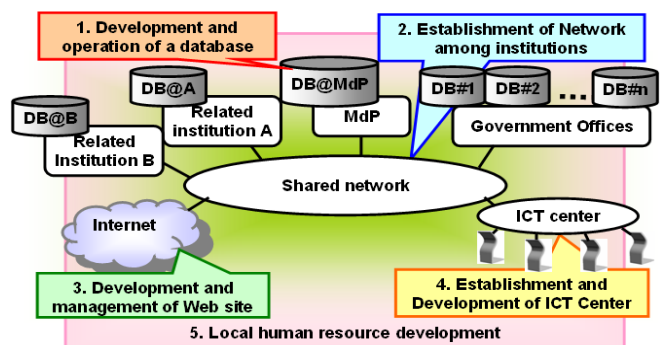


Figure 1 Components of ICT development [4]

## 4 Implementation of the pilot activities

In the implementation phase, the author has been mainly involved in local human resource development, development of database application, and development of ICT center out of the five components mentioned above.

### 4.1 Development of prototype database

## application

Since the development of database application was the first trial in Luang Prabang, the prototype database application, so-called “HeritageDB”, was created in Jan 2005, in order to show the example and clarify the requirements at the local site. The prototype contains data on the heritage architectures, wetlands, roads, drawings, and maps. Some data had been previously managed using Microsoft Access, but there were some problems, such as lack of regularization in data structure, buggy macros left due to the leave of the developer, and difficulty in sharing via the network. Therefore, the prototype was implemented to solve the problems of the existing database with some extension.

The prototype system was composed with Debian GNU/Linux as OS (Operating System), PostgreSQL as DBMS (Database Management System) and Zope as Web application server, having the following three features; web-based interface to promote sharing and dissemination of data, use of FOSS (Free and Open Source Software) to keep the legality and cost efficiency, and multi-language support of the interface for the local population and various target groups who use different languages.

### 4.2 Local human development

According to the requirement for local human resource, the local ICT team was organized with six Lao staffs from the government institutions, who have been equipped with insight on heritage conservation and urban development owing to the previous works.

The training workshops have been conducted with the following two features; one is needs based practical training which provides not only ICT skills but also the productions which are actually desired from the institutions. The other is the usage of FOSS in order to promote understanding on legal use of software and to save the cost.

### 4.3 Further development of database application

After the training was started, further development of database application has been conducted with the local ICT team based on the skills learned.

The database of the photos collected in MdP on the culture and on the natural environment in Luang Prabang, so-called “PhotoDB”, was created with thousands of photos which have been stored as the films or prints. The photoDB has been equipped with photo management interface to enable the search by various criteria from number of photos, of which detailed profiles are input and updated.

Also, further improvement of the user-interface of HeritageDB was implemented utilizing the graphical documents such as maps and drawings, in order to promote usability both for internal and external use.

### 4.4 Setting up the pilot ICT center

The database applications created in 4.1 and 4.3 were opened

to public in the first pilot ICT center established in July 2006. For the sustainable operation, self-sustainable financial cycle has been required by reducing the initial/running cost and promoting income generating activities. Also, involvement of the local communities was appreciated such as employment the local staff, encourage the communities’ participation in the discussion, and the promotion of the business by local people in the site.

The center was established in the site of the representative heritage of Lao wooden architecture. It has been equipped with the five PCs to access to those two prototype databases and web site of MdP, browsing space of the books, CDROM, brochures, posters and goods of Luang Prabang, of which parts are also for sale in order to earn the operation cost of the ICT center.

In the first sixteen weeks, 1,500 people have visited the center, of which 73% were tourists from foreign countries. According to the feedbacks from the visitors, most of visitors regard the database application as the attracting resource of information, and they were satisfied with the well-equipped center. On the other hand, also quite some comments for the required improvements were given. For the technical aspects, the enhancement of multi-language support, the more user-friendly graphical interface, and accessibility to the database application from Internet were suggested. Also for the contents, more information about the Luang Prabang history, and frequent update were requested.

## 5 Impacts from the activities

Through the implementation, the following impacts were observed at the local site.

1. Trained local ICT team members have become well-recognized ICT engineers in Luang Prabang. For instance, the governor’s office requests some technical support by the ICT team and it has increased motivation for the local ICT team to contribute to Luang Prabang
2. Introduction and training of FOSS raised awareness on legal use of the software, giving the options besides illegal copy of the commercial software.
3. Motivation of the organizations to participate in database creation has been increased. Some institutions have been motivated to provide their information to the ICT team for database creation, and some other institutions have interest to create their database application for their work.
4. The local communities have become more aware of public information, by visiting ICT center and participating in giving suggestion and discussion on the contents as public information.
5. The activities have gathered attention from International organizations and Media. For instance, the activity on the ICT

center was featured by the booklet, “Stay Another Day”<sup>4</sup>.

## 6 Further issues

### 6.1 Lack of Internet environment

Since the technical documents, technical supports, and updated programs of FOSS are available mainly in Internet, lack of Internet has made difficulties on human resource development and operation and maintenance of the system. Rapidly improving Internet connectivity in Luang Prabang hopefully will solve this problem.

### 6.2 Difficulty in multi-language support

Lao language support of the system is currently insufficient to obtain the maximum benefits from the database application. Input and display of Lao characters are possible on Microsoft Windows XP with additional software and fonts. Also, due to the lack of human resource for translation among languages, the multi-lingual contents development has been in the difficult situation.

### 6.3 Difficulty in self-sustainable financial cycle

The operation cost of ICT center was higher than expected. It was revealed that not only the cost for expensive ICT equipments, but also the running cost including employment of the security guards to save the expensive equipments are significant. Also, the number of visitors was not sufficient to get the sufficient amount income by selling goods and by the advertisement.

## 7 Discussion on sustainability

Through the experiences of this international development project, the author has tried to clarify important issues in the context of sustainable development. The identified issues are listed as follows:

**Integration:** Sustainability cannot be realized only by focusing on the area of expertise. When introducing appropriate ICT, it is necessary to consider the various related aspects, such as human resource, economics, logistics, politics and laws, technology, and culture.

**Adoption to change:** Since the local situation is rapidly changing, especially in developing countries it is also required to continuously observe and adapt to these changes. Technology is not an exception, and available and affordable hardware/software and infrastructure in locality should be followed up.

**Needs based development activities:** Any development project can be truly effective only when it is based on the local needs of communities and government. Therefore, careful needs assessment is a pre-requisite to the development project.

**Information sharing:** It is true that many development

activities are operated vertically. In order to promote the sustainability of ICT development, close communication among institutions is necessary. Especially, in the case multi-institutional project, it is necessary to continuously promote consensus by sharing information and mind, since different institutions might have different interest based on different scopes and culture.

**Local ownership:** It is often the case that the ownerships of the activities belong to experts, government, or agencies. But it is inevitable to enhance local ownership to effectively continue the development activities.

## 8 Conclusion

According to the needs assessment based on field survey, the proposed components for ICT development activities have been implemented, especially the author has been mainly involved in the local human resource development, development of database application and ICT center. Through the implementation, the activities have contributed to give the basis and view for the further ICT development in Luang Prabang. Especially, the local ICT team members who are equipped both with ICT skills and insight of heritage conservation and development can contribute to enable the ICT development in the context of heritage centered regional development.

Furthermore, five important issues for sustainable development were identified through the experience of this case study in particular attention to ICT field. Those issues hopefully contribute to promote the sustainable development in further activities in Luang Prabang and in other places in the world.

## References

- [1] The Independent Commission for Worldwide Telecommunications Development, (1984) “Missing Link”, ITU, CH-1211 Geneva 20, Switzerland.
- [2] N. Ooka, S. Yamaguchi, J. Takada, (2004) “Construction of telecommunication network for rural development: Feasibility study of ICT application to the World Heritage Site of Luang Prabang”, 3rd Great Asian Street Symposium, Singapore.
- [3] S. Yamaguchi, J. Takada, N. Ooka, J. Abe, (2005) “ICT contribution to promote sustainable development, Case study in the World Heritage site of Luang Prabang”, 8th World Symposium of the Organization of World Heritage Cities, Cusco, Peru.
- [4] S. Yamaguchi, M. Mochizuki, N. Ooka, (2005) The presentation slides of Tokyo Tech Team in Ministry of Information and Culture, Vientiane, Lao PDR

<sup>4</sup> Stay Another Day: <http://www.stay-another-day.org/>

## Study about Text Classification with Statistical Pattern Recognition Method

Student Number: 04M51254 Name: Yusuke Watada Supervisor: Yukihiko Yamashita

## 統計的パターン認識手法を用いた文書分類に関する研究

和多田 佑介

「文書分類タスク」は従来、自然言語処理の分野で研究されてきたが、近年では統計的パターン認識による手法も用いられている。String Subsequence Kernel(SSK)を用いた文書分類もその一つである。ところが、この手法の計算コストは非常に高いため、近似的な手法を用いる必要がある。そのために、特徴選択に工夫が必要となる。本研究では、特徴選択の方法を改良し性能向上を試みる。またSSKの特徴である言語に依存しないという点を利用し、スパムメール分類においても有効であることを実験で示す。

## 1 Introduction

The growth of the World Wide Web brings us the information society. A huge amount of information is generated, and we should process it every day. However, today we get so huge amount text data such as e-mails, web pages, and so on that we cannot process them manually. Therefore we require a good method to process them more quickly and automatically.

Natural Language Processing has been studied so many years to solve such a problem that we can process natural language automatically with computers. For example, asking computers of some questions by speaking natural language or interpreting a text written in foreign language into another automatically. However, generally it is very difficult for computers to solve like these kinds of problems, because natural language has so much variety and requires a lot of vocabulary.

“Text classification” has traditionally been studied in Natural Language Processing field. Recently it has also been studied in Statistical Pattern Recognition field. String Subsequence Kernel(SSK) is one of such methods, but it takes too high calculation cost. Although we suppose approximated methods, another problem occurred that we should select appropriate features. In this paper, we modify the feature selection method to improve the performance. And we adapt SSK to the Spam mail filter it never depends on any languages.

This paper consists of 6 Sections. In Section 1 we explain introduction of study. In Section 2 we explain Text classification. In Section 3 we explain Support Vector Machine. In Section 4 we explain SSK and provide a new feature selection method. In Section 5 we show computer experiments and its results. In Section 6 we provide conclusion.

## 2 Text Classification

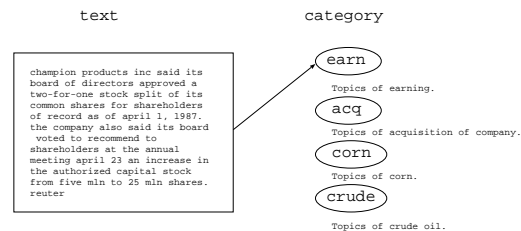


Figure 1: Text classification

“Text Classification” is a problem to map a certain input text to a category which is defined in advance. Traditionally, this kind of problem is solved by Natural Language Processing methods. At first, input texts are split into a sequence of smaller units, such as words or  $n$ -grams, and in each unit, we can calculate the probability of appearance from its appearance count. For example, bayesian classifier is one of the famous text classifiers. Naive bayes is the simplest bayesian classifier, and its expression is following:

$$\arg \max_i P(C_i|S) = \frac{P(C_i \cap S)P(C_i)}{P(S)}$$

$$= \frac{\prod_j P(w_j)P(C_i)}{P(S)}.$$

$S$  is an input text, and  $C_i$  represents the classes for each  $i$ .  $w_j$  represents words which appeared in  $S$  for each  $j$ .  $P(C_i|S)$  means the probability where we get  $S$  as input text and  $S$  map to  $C_i$ . To determine the class which  $S$  map to, we calculate  $P(C_i|S)$  for each  $i$ , and we select the most probable class of  $i$ .

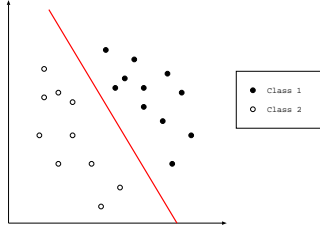


Figure 2: Linear Classifier

Support Vector Machine(SVM) is a 2-class classifier which uses the feature vectors and a hyperplane classifier with a kernel function. In this kind of methods, we previously transform training/test patterns into feature vectors, and using training vectors, learn the parameter in the following linear classification function:

$$d(x) = \langle w, x \rangle + b.$$

$x$  represents the input vector,  $w$  is a weight vector constant, and  $b$  is a scalar constant. If this function returns positive, then  $x$  map to class 1, and negative, class 2. If we may divide feature vectors into two groups by hyperplane, we have many possible hyperplanes. So we would like to determine the most proper one by using training vectors. This means we determine  $w$  and  $b$ .

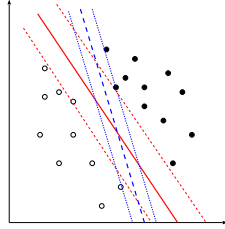


Figure 3: Margin Maximization Principle

One of the most proper strategies for classification is to determin constants so as to maximize its margin. Margin is the minimum distance between hyperplane to the most neighbor samples for each class. This strategy is called Optimal Hyperplane Classifier(OHC) and it is good at classifying unknown samples. However some problems are still remained. Primary, if we have no hyperplane which can divide the samples, we cannot use this kind of method. Secondary, when we calculate classification function, we have to obtain the inner product of an input vectors. Generally, the dimension of feature vectors is very high, and calculation cost of inner product is also high. Thus, we cannot treat high dimensional vector spaces in this method.

Then, we adapt the following kernel function. (H. D. 2007/08, February 22, 2008 (ISSN 1880-8468))

$$\langle \phi(x), \phi(y) \rangle = K(x, y).$$

We can replace the kernel function from the inner product. If we use the kernel function, we can cut down the calculation cost.

As kernel functions, generally used like followings.

$$\begin{aligned} K(x, y) &= \langle x, y \rangle && : \text{Identical.} \\ K(x, y) &= (\langle x, y \rangle + c)^p && : \text{Polinomial.} \\ K(x, y) &= \exp(-\frac{\|x-y\|^2}{2\sigma^2}) && : \text{Gaussian.} \end{aligned}$$

## 4 String Subsequence Kernel

In kernel method, we only have to calculate a kernel function but the inner product itself. Then, we suppose a new kernel function what we call String Subsequence Kernel(SSK). This kernel provides the similarity of two input texts by retrieving the feature quantity based on following expression.

$$\begin{aligned} K_n(s, t) &= \sum_{u \in \Sigma^n} \phi_u(s) \phi_u(t) \\ &= \sum_{u \in \Sigma^n} \sum_{i: u=s[i]} \lambda^{l(i)} \sum_{j: u=t[j]} \lambda^{l(j)} \\ &= \sum_{u \in \Sigma^n} \sum_{i: u=s[i]} \sum_{j: u=t[j]} \lambda^{l(i)+l(j)}. \end{aligned}$$

Lefthand means SSK of length- $n$  between text  $s$  and text  $t$ .  $\Sigma$  is a set of all alphabets, and  $\Sigma^n$  means a set of all substring of which length is  $n$ .  $i$  and  $j$  are substring index vector. For example, if substring  $s$  consists of first, third and fourth letter from original string,  $i = (1, 3, 4)$  and  $s[i]$  means substring consists of  $i$ . If we get the two string  $s$  and  $t$ , we retrieve all capable substrings from  $s$  and  $t$ , and compare with each other. If the substrings are same, we calculate and add the feature quantity.  $\lambda$  is a decaydane parameter, and  $l(i), l(j)$  are length of each substring. This means the longer the substring is, the lower the feature quantity.

	c-a	c-t	a-t	b-a	b-t	c-r	a-r	b-r
$\phi(cat)$	$\lambda^2$	$\lambda^3$	$\lambda^2$	0	0	0	0	0
$\phi(car)$	$\lambda^2$	0	0	0	0	$\lambda^3$	$\lambda^2$	0
$\phi(bat)$	0	0	$\lambda^2$	$\lambda^2$	$\lambda^3$	0	0	0
$\phi(bar)$	0	0	0	$\lambda^2$	0	0	$\lambda^2$	$\lambda^3$

For example, this table describes the results of mapping of 4 strings, *cat*, *car*, *bat*, and *bar*, For each string

the feature values of length-2 substrings. c-a, c-t, a-t, b-a, b-t, c-r, a-r and b-r are written in the table elements. In *cat*, *c* and *a* are first and second letter, so feature value c-a is  $\lambda^{2-1+1} = \lambda^2$ . All the same to bar, *b* and *r* are first and third letter, so feature value b-r is  $\lambda^{3-1+1} = \lambda^3$ . Then, we can calculate kernel value of SSK like followings:

- $K_2(cat, car) = \lambda^2 \times \lambda^2 = \lambda^4$ .
- $K_2(bat, bar) = \lambda^2 \times \lambda^2 = \lambda^4$ .
- $K_2(cat, bar) = 0$ .
- $K_2(car, bat) = 0$ .

*Cat* and *car* have common substring c-a, so its kernel value is  $\lambda^4$ . *Bat* and *bar* are similar. However, *cat* and *bar* or *car* and *bat* have no common substrings, so their kernel values are zero.

Furthermore, by improving the calculation form with dynamic program, we can much more reduce the calculation cost.

$$\begin{aligned}
 K'_0(s, t) &= 1, \text{ for all } s, t. \\
 K'_i(s, t) &= 0, \text{ if } \min(|s|, |t|) < i. \\
 K_i(s, t) &= 0, \text{ if } \min(|s|, |t|) < i. \\
 K_i(sx, t) &= \lambda K'_i(s, t) + \sum_{j:t_j=x} K'_{i-1}(s, t[1:j-1]) \lambda^{|t-j+2|}. \\
 i &= 1, \dots, n-1. \\
 K_n(sx, t) &= K_n(s, t) + \sum_{j:t_j=x} K'_{n-1}(s, t[1:j-1]) \lambda^2.
 \end{aligned}$$

Practically we uses the following normalized SSK because of not depending on input text length.

$$\hat{K}_n(s, t) = \frac{K(s, t)}{\sqrt{K(s, s)K(t, t)}}.$$

#### 4.1 Approximated SSK

As we mentioned above, SSK takes too high calculation cost. Then we use the approximated SSK. In this method, previously we select the substrings and for each input text, calculate the SSK with them. Generally, only a few features contribute the performance in classification but others are not so much. Therefore we can take approximate strategy in SSK. Each SSK value is the approximated feature value of SSK. Following expression is a function of approximated SSK.

$$K_n(x, y) = \sum_{s \in S} K(x, s) K(y, s).$$

*S* represents a set of substring as SSK such as  $S \subset \Sigma^n$ . In this strategy, we should determin a proper substring set *S*.

#### 4.2 Feature Selection

When we select features, we should consider what feature is proper to use. Feature selection effects the classification directly, so we should use a good feature select strategy. In existing studies, features are selected with its appearance count as substring. We propose a method that takes feature's inner class variance into account. That is we use the features which is large feature values in one class but small in others. This criterion is implemented by the following expression.

$$v_{ij} = f_{ij} - \left( m_{ij} + \sqrt{\sum_{k \neq i} \frac{(f_{kj} - m_{ij})^2}{L-1}} \right). \quad (1)$$

$f_{ij}$  is a mean of *j*th feature in *i*th class,  $m_{ij}$  is the averaged value of  $f_{ij}$  where  $i \neq j$ , and *L* is a number of classes. For each *i*, we calculate  $v_{ij}$  and enumerate them by descendant order of  $v_{ij}$ . Finally we choose the most largest *n* features of the class *i*.

### 5 Experiments

#### 5.1 Text Classification

In this problem, we use the 3000 training samples and 1000 test samples from Reuters-21578 data set. There are 4 categories, earn, acq, crude and corn in it.

class	data size	existing	proposed
earn	1759	<b>96.42</b>	96.35
acq	905	89.47	<b>91.95</b>
corn	104	56.61	<b>72.35</b>
crude	232	78.37	<b>81.69</b>

The table is the comparrison between the existing feture selection strategy and the proposed one. The results are expressed by *F1* value. *F1* value is calculated by the following expression where *p* is precision and *r* is recall.

$$F1 = \frac{2pr}{p+r}.$$

From this result, we can say that we get good performance in 3 data sets, acq, corn, crude.

#### 5.2 Spam Filter

Secondly, we adapt the approximate SSK to mail classification. Recently spammers make complex tricks on junk mails and we cannot classify them by simple spam filters which are based on word features. However, we consider that SSK will achive a good performance in junk mail recognition, because SSK can treat not only

continuous substrings but also noncontinuous substrings. In this experiment, we compare the performance among bsfilter and SSKs with the existing and proposed feature selection strategies. The bsfilter is the opensource bayesian filter software.

method	accuracy
bsfilter	$93.31 \pm 2.66$
Existing	$90.51 \pm 7.26$
Proposed	<b><math>97.12 \pm 1.21</math></b>

From this result, we can say proposed method achieve better performance than bsfilter.

## 6 Conclusion

In this paper, we explained about Text Classification, SVM SSK. SSK needs too high calculation cost to use practically. Then we use the approximation of SSK. In this strategy, we use a few features for classification. However, it brings another problem that we should select proper features from all. Existing work do this task by only selecting a set of  $n$ -grams depending on its appearance count. The new method we proposed is a new feature selecting method. And we showed its advantages by experimental result of text classification and spam filtering problems. As future tasks, we should verify the results more precisely, introduce orthogonalization methods such as GSO, KL-extraction, and reduce calculation cost.

## References

- [1] Text Classification using String Kernel. Huma Lodhi, Journal of Machine Learning Research 2(2002)
- [2] SpamCop: A Spam Classification & Organization Program, Patrick Pantel(1998)
- [3] David Haussler Convolution Kernels on Discrete Structures(1999)



# Extraction of liquid organic multi-component mixture with ionic liquids as solvents

Student ID: 05M18018 Name: Kenya AKAISHI Supervisor: Ryuichi Egashira & Sachio Hirose

イオン液体を溶媒とした液状有機系多成分混合物の抽出  
赤石 憲哉

吸収油中の同素環式化合物(ナフタレンなど)に比較して含窒素複素環式化合物(インドールなど)の、改質ガソリン中の飽和鎖式化合物(ヘキサン)に比較して芳香族化合物(ベンゼンなど)が選択的にイオン液体中に抽出された。従来用いられている抽出溶媒に比較して、イオン液体を溶媒とした場合においては収率が高く、分離の選択度は低かった。どちらの原料混合物においても、抽出相中からの抽出成分の分離に関して、イオン液体の分解点が抽出成分の沸点範囲より高いことから、蒸留を用いた分離操作が可能であった。

## 1. Introduction

Ionic liquids are organic salts that are liquid under 373 K. Ionic liquids have quite low volatility and flammability<sup>[4]</sup>, they are inactive against water and the oxygen.

It has been already reported that the nitrogen compounds and the aromatic hydrocarbons were separated with ionic liquids as solvents from nitrogen/homocyclic compound model mixtures<sup>[5]</sup>, aromatic/aliphatic hydrocarbon model mixtures<sup>[2]</sup> respectively. However there is no report of the separation from an actual multi-component mixture.

In this work, the ionic liquids were applied to the separation of the actual liquid organic multi-component mixtures as extraction solvents. This would be done by the confirmation of the thermal stability of the ionic liquids and the equilibrium extraction of the organic multi-component oil mixtures. And the separation process in which the extracted components were separated from the extract phase was considered.

## 2. Experimental

### 2.1. Material System

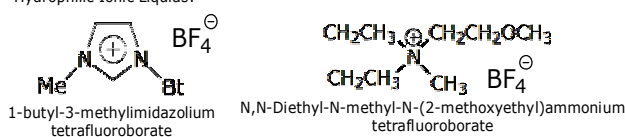
Four types of ionic liquids were selected as extraction solvents. 1-butyl-3-methyl-imidazolium tetrafluoroborate, [Bmim][BF<sub>4</sub>]; 1-butyl-3-methylimidazolium hexafluorophosphate, [Bmim][PF<sub>6</sub>], were purchased from Wako Chemical Co. Ltd.

N,N-Diethyl-N-methyl-N-(2-methoxyethyl)ammonium tetrafluoroborate, [Et<sub>2</sub>MeMeON][BF<sub>4</sub>]; and N,N-Diethyl-N-methyl-N-(2-methoxyethyl)ammonium bis(trifluoromethanesulfonyl)imide, [Et<sub>2</sub>MeMeON][Tf<sub>2</sub>N], were provided by Nisshinbo Ind. Inc. (Tokyo, Japan). The structure of these ionic liquids is shown in Figure 1. The actual organic multi-component mixtures were coal tar absorption oil (AO), reformat gasoline (reformat) and light cycle oil (LCO).

### 2.2. Thermal stability of ionic liquids

The thermal stabilities of ionic liquids were measured by thermogravimetry (TG8120, Rigaku Denki Co. Ltd.) (TG).

Hydrophilic Ionic Liquids:



Hydrophobic Ionic Liquids:

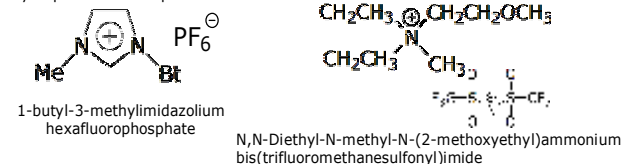


Figure1: The structure of ionic liquids used in this research

### 2.3. Equilibrium Extraction

All organic multi-component mixtures were brought into contact with each ionic liquid in a  $3.5 \times 10^{-6} \text{ m}^3$  vial. They were agitated intensely. After settlement, the miscibility between organic multi-component mixtures and the ionic liquids were observed. The immiscible combinations of organic multi-component mixtures and ionic liquids were employed in extraction experiments. The experimental conditions are shown in Table 1. The samples were stirred for 120 hours at room temperature to attain the equilibrium.

Table 1: Experimental Conditions

Feed, R <sub>0</sub>	[kg]	0.0010 - 0.0017
Solvent, E <sub>0</sub>	[kg]	0.0015 - 0.0023
E <sub>0</sub> /R <sub>0</sub>	[-]	0.5 - 1.0
Time	[h]	120
Temperature	[K]	296 ± 1

The compositions in the liquid phase were determined by gas chromatography (GC17A, Shimadzu) (GC) and Karl-Fisher Titration (Metrohm. Ltd.) (KF). Those in the extract phase were also determined by GC and KF after the reverse extraction was carried out with organic solvents.

## 3. Results and Discussion

### 3.1. Thermal stability of ionic liquids

Figure 2 shows the results of the TG analysis. The ionic liquids began to decompose around 600 K. All ionic liquids were thermally stable upto around 600 K.



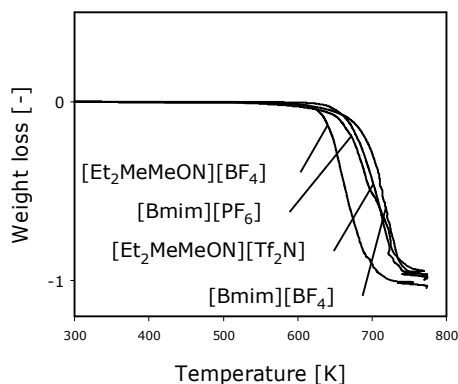


Figure 2: TG diagram of ionic liquids; the ordinate is the weight loss of samples and the transverse is the temperature.

### 3.3. Equilibrium Extraction

The results of the miscibility were listed in Table 3. The hydrophilic ionic liquids; [Bmim][BF<sub>4</sub>] and [Et<sub>2</sub>MeMeON][BF<sub>4</sub>] were miscible with water, while the hydrophobic ionic liquids; [Bmim][PF<sub>6</sub>] and [Et<sub>2</sub>MeMeON][Tf<sub>2</sub>N] were immiscible with water. All the ILs were immiscible with reformat and LCO.

Table 3: The miscibility Y<sub>i</sub> of ionic liquids with water, absorption oil, reformat and light cycle oil (O-miscible, X-immiscible)

cation	anion	H <sub>2</sub> O	AO	reformat	LCO	MeOH	EtOH	Acetone	nC <sub>6</sub>	Toluene
[BMIM]	[BF <sub>4</sub> ]	O	X	X	X	O	O	O	X	X
[BMIM]	[PF <sub>6</sub> ]	X	O	X	X	O	X	O	X	X
[Et <sub>2</sub> MeMeON]	[BF <sub>4</sub> ]	O	X	X	X	O	△	O	X	N.A.
[Et <sub>2</sub> MeMeON]	[Tf <sub>2</sub> N]	X	O	X	X	O	O	O	X	N.A.

The compositions of feed oils are shown in Table 2, and the gas chromatograms of feed oils are shown in Figure 3. The feed oils contain a lot of components. Among those, the components listed in Table 2 were selected to be identified and studied. And the mass fractions of water were 0.001 and 0.0005 in AO and reformat respectively.

Table 2: The compositions of feed oils; AO and reformat

Absorption Oil			Reformat		
constituent	abbrev.	mass fra.	constituent	abbrev.	mass fra.
Quinoline	Q	0.08	Benzene	B	0.05
Isoquinoline	IQ	0.02	Toluene	T	0.23
Indole	I	0.05	m-Xylene	X	0.19
Naphthalene	N	0.03	n-Hexane	H	0.04
1-Methylnaphthalene	1MN	0.11			
2-Methylnaphthalene	2MN	0.25			
Biphenyl	BP	0.07			
Dibenzofuran	DBF	0.12			

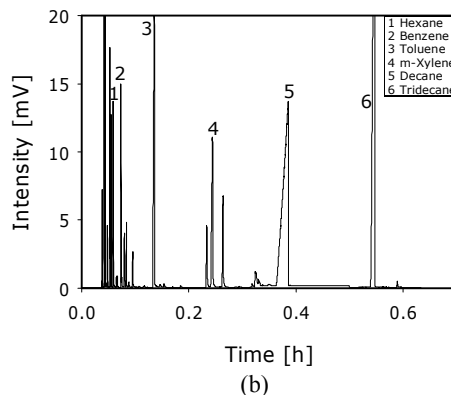
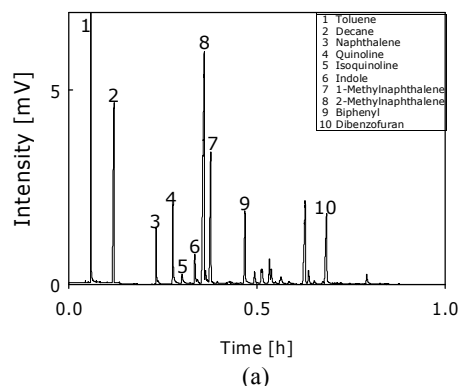


Figure 3: the gas chromatograms of feed oils (a) AO; (b) reformat

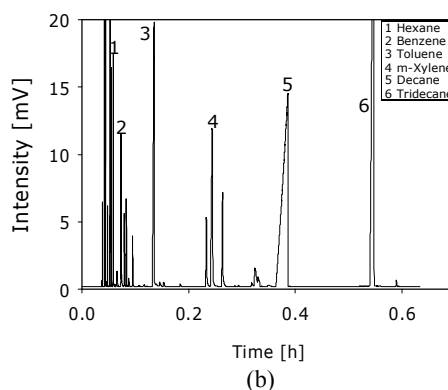
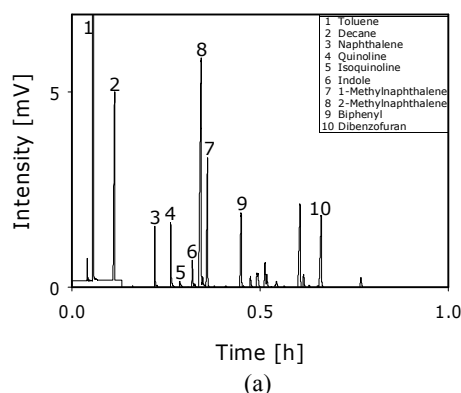


Figure 4: the gas chromatograms of the raffinate (a) AO; (b) reformat

The gas chromatograms of the raffinate are shown in Figure 4. Compared with the gas chromatograms of feed oils, the peaks of nitrogen compounds in AO and those of aromatic hydrocarbons in reformat became smaller, hence the nitrogen compounds and aromatic hydrocarbons preferentially transferred into the extract phase.

It was difficult to analyze the extract phase by means of reverse extraction method, because of the polarity, the structures of ionic liquids and so on, so that the material balance relationship during the runs was not sound. The discussion was based on the composition in the raffinate hereafter. Figures 5 and 6 show the yields of each

component,  $Y_i$ , plotted against solvent component in the case of AO and reformat respectively. The yield was defined by equation 1.

$$Y_i = 1 - \frac{R_{X_i}}{R_0 X_0} \quad \text{Equation 1}$$

In case of AO, the yields with the solvent of ionic liquids were higher than those with the aqueous methanolic solution<sup>[1]</sup>. The yields of indole with both ionic liquids reached up to 90 percents. In case of reformat, the yields of hexane using ionic liquids were much higher than using sulfolane<sup>[3]</sup>. The yields of aromatic hydrocarbons with ionic liquids were in the range from 30 to 50 percents.

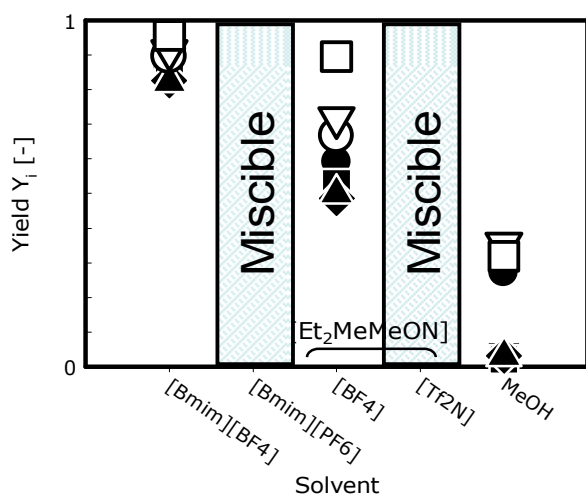


Figure 5: the yields,  $Y_i$  of AO compositions  
○-Quinoline, ▽-Isoquinoline, □-Indole,  
●-Naphthalene, ▼- 1-Methylnaphthalene,  
■-2-Methylnaphthalene, ◆-Biphenyl,  
▲-Dibenzofuran

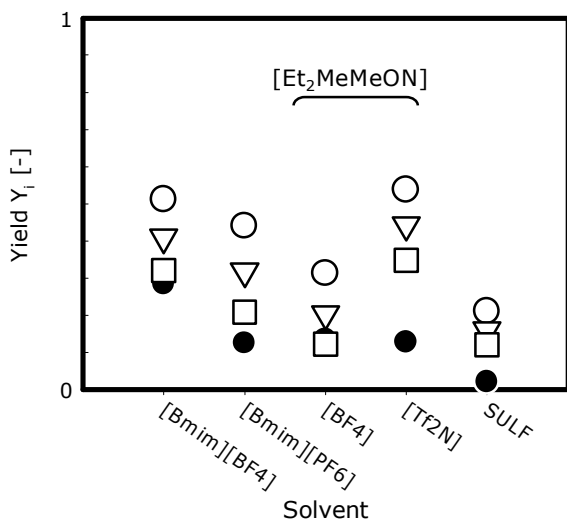


Figure 6: the yields,  $Y_i$  of reformat compositions  
○-Benzene, ▽-Toluene, □-m-Xylene, ●-Hexane

The definition of the separation selectivity is shown in equation 2. The separation selectivities of each compounds in AO and reformat are shown in Figure 7 and 8 respectively.

$$\beta_{i,j} = \frac{Y_i}{Y_j} \quad \text{Equation 2}$$

Since the separation selectivities of nitrogen compounds and aromatic hydrocarbons were higher than the unity in case of AO and reformat respectively, the nitrogen compounds and aromatic hydrocarbons could be separated selectively from AO and reformat respectively. The selectivities with ionic liquids were lower than those with conventional solvents. In AO, indole was extracted more preferentially into the extract phase than the other nitrogen compounds. The separation selectivities of the nitrogen compounds with the ionic liquids constituted a reversal unexpectedly from those with the aqueous methanolic solution, which means the indole had a higher selectivity than the others using the ionic liquids, on the other, hand it had a lower using the aqueous methanolic solution. In reformat, the selectivities with hydrophobic ionic liquids were higher than those with hydrophilic ionic liquids.

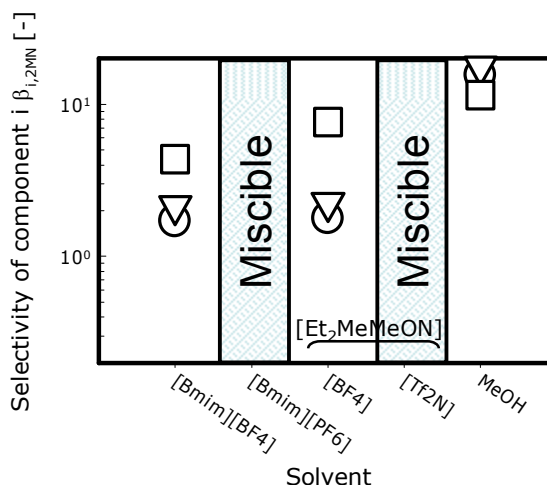


Figure 7: the separation selectivity in case of AO.  
○-Quinoline, ▽-Isoquinoline, □-Indole

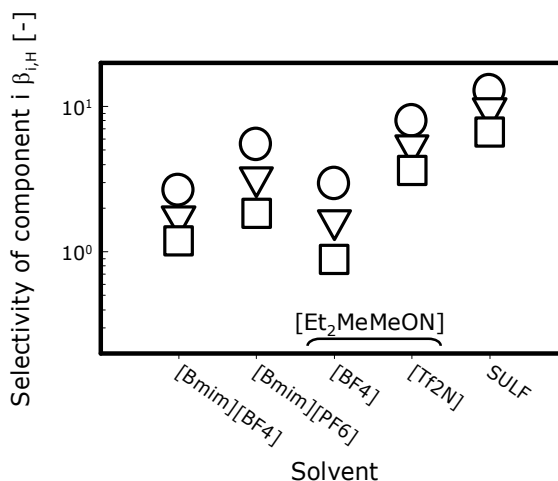


Figure 8: the separation selectivity in case of reformat  
○-Benzene, ▽-Toluene, □-m-Xylene

### 3.3. Extraction Process

The separation of the extracted components from the extract phase is required after the extraction. The simple scheme of the separation process is shown in Figure 8. The According to TG results, ionic liquids were remarkably thermally stable upto around 600 K. And there is the difference between the decomposition temperature of the ionic liquids and the boiling range of extracted components. The extracted components in extract phase could be separated from extract phase and the ionic liquid could be recovered by the distillation.

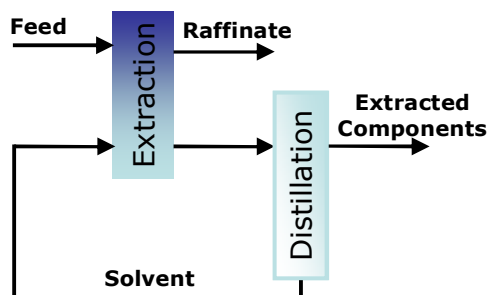


Figure 8: the simple scheme of the separation process

### 4. Conclusions

The nitrogen compounds and the aromatic hydrocarbons were separated from actual organic multi-component mixtures. The ionic liquids used in this research have the thermal stability upto around 600 K. The solvent extraction could be operated owing to the immiscibility of the ionic liquids. The nitrogen compounds and the aromatic hydrocarbons were separated preferentially from AO and reformat respectively. The yields with ionic liquids were higher than with the conventional solvents. The separation selectivities with ionic liquids were inferior to those with conventional solvents. The selectivities with hydrophobic ionic liquids were higher than with hydrophilic ionic liquids in case of reformat. After the extraction, it could be possible to separate the components in extract and to recover ionic liquids by the distillation

### 5. Acknowledgment

The author wish to thank Nisshinbo Co., Ltd., JFE Chemical Co., Ltd., and Idemitsu Kosan Co., Ltd. for providing the materials.

### 6. Nomenclatures

R:	mass of raffinate	[kg]
$R_0$ :	mass of feed	[kg]
$x_i$ :	mass fraction of component i in raffinate phase	[-]
$x_{0,i}$ :	mass fraction of component i in feed	[-]
$Y_i$ :	yield of component i	[-]
<subscripts>		
i:	component i	
j:	component j	
w:	water	
<greek>		
$\beta$ :	separation selectivity	[-]

### 7. Literature Cited

- [1] C. Salim  
*Doctoral thesis, Tokyo Tech, 2005*
- [2] G. Wytze Meindersma *et. al.*  
*Fuel Processing Technology*, **87**, 59-70, 2000
- [3] H. Habaki  
*Master thesis, Tokyo Tech, 1995*
- [4] Jonathan G. Huddleston *et. al.*  
*Chemical Communication*, 1765-1766, 1998
- [5] M. Matsumoto *et. al.*  
*Journal of Japan Petroleum Institute*, **49**, (5), 256-261, 2006

# Moving picture coding with wavelet transform

Student Number : 05M18024 Name : Takashi OHTA Super visor : Yukihiro YAMASHITA

## ウェーブレット変換を組み合わせた動画画像符号化に関する研究

太田 昂志

MPEG に代表されるブロック単位の動画画像圧縮方式には、復号した画像にブロック歪が現われる問題が生じる。この問題を解決するために「ウェーブレット変換を組み合わせた動画画像符号化」を提案する。この手法は復号画像のブロック歪みを減らすだけでなく、予測画像にデブロッキングフィルタを適用することにより、差分画像におけるブロック歪みも減らすことで、より効率的な符号化が期待できる。

## 1 Introduction

In recent years, the information communication technology called IT (Information Technology) is splendidly developed. Not only a document but also a picture, a sound, etc. are widely used for communication. However, the amount of information of the multimedia data which generally contains digitized pictures and sounds are huge. Therefore, in order to treat the information, the transmission way and the mass storage medium of a broadband are needed. Then, the research on reduction of the information by the data compression of pictures or sounds so-called compression coding came to be popular for the purpose of efficient use. Although the broadband communication can be used in wide area, narrowband communication is also used. Then, efficiency of image coding has to be increased.

Video coding is the method of compressing by reducing the redundancy included in video data. There are two kinds of redundancy of video data. One is the spatial redundancy and the other is time redundancy. The former is also used in still picture coding. JPEG (JointPhotographic Experts Group) which is an international standard system of still picture coding is a technique used very widely. And the algorithm called motion compensation prediction is used in the latter reduction. This is used in MPEG (Moving Picture Experts Group) which is the international-standard system of video coding. It became possible to code and compress video data at high efficiency by these two techniques compared with only the former. However, such algorithm had the problem in a decoding picture. Visual degradation called block distortion is produced from pro-

cess per block.

## 2 MPEG

MPEG is a standard of the multimedia coding for accumulation media, broadcast, communication, etc. It mainly consists of three regulations, such as the regulation on the coding method of a video signal, the regulation on the coding method of an audio signal, and for both integrated method.

Video data is realized by the set of the still picture located in a line on the time-axis generally called a frame. MPEG performs compression coding by reducing those spatial and time redundancies. Reduction of spatial redundancy is called the coding in a frame, and performs DCT (discrete cosine transform), quantization, and coding every  $8 \times 8$  [pixel] block. Moreover, reduction of time redundancy is called the coding between frames, and is performed using the technique of motion compensation prediction. This is extracting and treating the motion information on a certain domain in a picture in two near frames in time. Generally, block matching is performed by every  $16 \times 16$  [pixel] block. And the motion vectors which express motion information is extracted. The general procedure of motion compensation prediction is shown below.

1. Extraction of moving vector by comparing the frame for encoding with the reference frame
2. Generation of the prediction picture by the motion vector and the reference frame

3. Generation of the picture of difference by the subtracting of the prediction picture from the frame for coding
4. Coding of the motion vector and the picture of difference
5. Execution of 1. to the following two frames

The main coding parts of MPEG are realized with the combination of the coding between frames and inside of a frame. First of all as a basic procedure of MPEG, the frame of the beginning of video or the frame used as a starting point is coded in a frame. These frames are called I-picture. I-picture which had conversion-quantization performed here is reverse converged by the local decoder, and is temporarily memorized by the frame memory. Next, frames other than I-picture are coded between frames which uses motion compensation prediction. There are P-picture and B-picture in these frames. The obtained prediction picture which is made based on a vector and it, and the picture of the difference of a target frame are coded. This reduces time redundancy and more efficient compression is performed.

### 3 Moving picture coding with wavelet transform

In the coding using the block matching method represented by MPEG, the problem of producing block distortion which is visual lattice-like degradation appears in the reconstructed video. On the other hand, in the field of still picture coding, the coding which reduces block distortion using wavelet transform and subband conversion as a technique has been advocated. Then, in order to control block distortion produced in video, we try to apply the coding (wavelet coding) which uses wavelet transform. However, the conventional motion compensation prediction which uses block matching is not efficient. Then, we propose applying the deblocking filter to the motion compensation prediction.

#### 3.1 Deblocking filter

At first, we use the conventional block matching method to predict the latter frame. Next, we use the deblocking filter to the predicted image. Then we examine the

surroundings of the pixel which a target of the filter whether the area is an edge or not. And, in the predicted image we calculate the difference of the pixel values in which the boundary between blocks. By the result, we change the direction and the strength of the filter. The algorithm of motion compensation prediction with deblocking filter is as follows.

1. A target block is made to match with a reference frame using the block of  $16 \times 16$ [pixel].
2. the predicted image is created by the motion vector.
3. In the predicted image the deblocking filter to each pixels on the boundary of the block is applied. Except the boundary between two blocks that have the same motion vector.

For example, show the calculation for  $p_{0,0}$  in the Fig.1. Calculation flow of deblocking filter for  $p_{0,0}$  is as follows.

1. Start condition,  $state = 0, a, b, c, d = const$
2. *if*  $(|p_{0,-1} - p_{0,0}| < a, \text{ and } |p_{0,0} - p_{0,1}| < b)$ ,  
state+1
3. *if*  $(|p_{-1,-1} - p_{0,0}| < a, \text{ and } |p_{0,0} - p_{1,1}| < b)$ ,  
state+2
4. *if*  $(|p_{1,-1} - p_{0,0}| < a, \text{ and } |p_{0,0} - p_{-1,1}| < b)$ ,  
state+4
5. *if* state= 1,7  

$$p_{0,0} = (p_{0,-2} + p_{0,-1} \times 2 + p_{0,0} \times 2 + p_{0,1} \times 2 + p_{0,2} + 4) \div 8$$

$$p_{0,-1} = (p_{0,-2} + p_{0,-1} + p_{0,0} + p_{0,1} + 2) \div 4$$
6. *if* state= 2  

$$p_{0,0} = (p_{-1,-1} + p_{0,0} \times 2 + p_{1,1} + 2) \div 4$$
7. *if* state= 3  

$$p_{0,0} = (p_{0,-2} + p_{-1,-1} + p_{0,-1} + p_{0,0} \times 2 + p_{0,1} + p_{1,1} + p_{0,2} + 4) \div 8$$

$$p_{0,-1} = (p_{0,-2} + p_{0,-1} + p_{0,0} + p_{0,1} + 2) \div 4$$
8. *if* state= 4  

$$p_{0,0} = (p_{1,-1} + p_{0,0} \times 2 + p_{-1,1} + 2) \div 4$$
9. *if* state= 5  

$$p_{0,0} = (p_{0,-2} + p_{1,-1} + p_{0,-1} + p_{0,0} \times 2 + p_{0,1} + p_{-1,1} + p_{0,2} + 4) \div 8$$

$$p_{0,-1} = (p_{0,-2} + p_{0,-1} + p_{0,0} + p_{0,1} + 2) \div 4$$

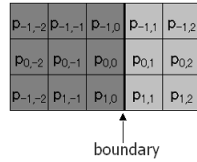


Fig. 1: Example of calculation

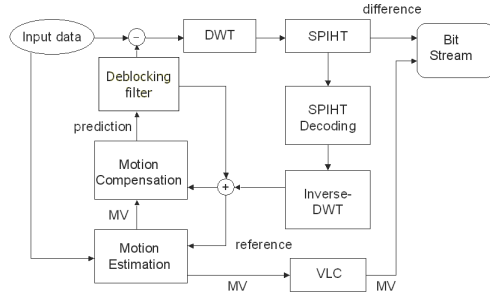


Fig. 2: Diagram of proposed encoding method

10. if state= 0,6 Don't apply filter.

### 3.2 Wavelet coding

Wavelet coding is used for the compression coding in the case of mainly inclining information for every frequency band. When especially energy inclines toward the low cycle, it is known that very efficient coding is possible. There is the coding method called SPIHT (Set Partitioning In Hierarchical Trees) which is specialized in the tree structure of wavelet. This coding method is used for the coding part of the proposal technique. Correlation will become high supposing the 2-dimensional motion vector obtained by motion compensation prediction of a pixel unit is extracting the motion correctly. Therefore, motion information inclines toward lower frequency domain. Moreover, the absolute value of the pixel of the picture of difference becomes very small. Therefore, both information is compressible at high efficiency using the above-mentioned wavelet coding.

### 3.3 Image coding experiment

In an experiment, two frames of the standard video sequence for assessment are used for I-picture and P-picture, respectively. And coding and decoding were performed by the proposal technique. The example of a frame is shown in Fig.3. Moreover, it is compared with



Fig. 3: Rotating disk

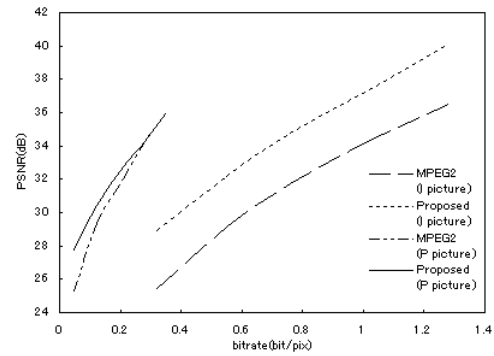


Fig. 4: PSNR for different bit rates

MPEG2 used as codec of Hi-Vision or standard quality-of-image television. And quality-of-image degradation of a decoding picture was evaluated numerically. PSNR is used for numerical assessment. PSNR is given by the following formulas here.

$$PSNR(dB) = 20 \log \frac{255}{MSE} \quad (1)$$

$$MSE = \sqrt{\frac{\sum_{x=0}^{W-1} \sum_{y=0}^{H-1} (f(x,y) - f'(x,y))^2}{WH}} \quad (2)$$

In coding of I-picture, the block distortion is produced by MPEG which performs block processing in a decoding picture. However, block distortion is not produced by the proposal technique. By comparison by PSNR, it turned out in the amount of marks with the same proposal technique that a picture better than MPEG is obtained. This result is shown in Fig.4.

In coding of P-picture, we compare the decoded images of MPEG2 and proposed. Fig.5 and Fig.6 are decoded images which are zoomed by four times. In the former image block distortion is seen, and in the latter is not. Deblocking filter disturbed that an unnecessary high frequency elements included in the difference image. And, Fig.4 shows the good result at proposed P

picture. Especially in the low bit rate condition.



Fig. 5: Decoded P picture of MPEG2



Fig. 6: Decoded P picture of proposed method

## References

- [1] Yoshinori Sakai , Toshiyuki Yoshida : “Image information encoding”, Ohmsha, 2001.
- [2] Sadayasu Ono , Junji Suzuki : “Achievement method of comprehensible JPEG/MPEG2” , Ohmsha, 1995.
- [3] Susumu Sakakibara : “Wavelet beginner’s guide” , Tokyo Electrical Engineering College Publications Service , 1995.
- [4] Amir Said, William A. Pearlman : “A New Fast and Efficient Image Codec Based on Set Partitioning in Hierarchical Trees” , IEEE Trans. Circuits and Systems for Video Technology, vol.6, pp.243-250, June. 1996.

## 4 Conclusions

In this paper, the video coding method using deblocking filter and wavelet transform was proposed, the computer experiment was conducted, and the good result was shown with the experiment especially in the low bit rate condition. For future work, we have to develop the block noise detection method that provides more highly efficient, and a more efficient coding method for the difference image.



# Creation and Evaluation of e-Learning materials for Introduction of Engineering

Student Number: 05M18030 Name: Masanori Kaneko Supervisor: Jun-ichi TAKADA

## 工学導入教育のための e-Learning 教材の作成とその評価

金子 昌永

最先端の科学技術研究は学問の深化・細分化を生んでおり、低学年の学部学生にとって、理数系基礎科目との関連性を理解するのは難しい。また、日常生活に浸透した最先端技術はブラックボックス化されており、使用者にとっての科学的興味の対象ではなくなっている。よって、高校の理数系教育から工学教育への橋渡しを行う「工学導入教育」を提案し、教材を作成した。また、教材の形態は web コンテンツとした。これは、主として学生の興味を喚起するリッチコンテンツを扱うためである。本学の初年度学生を対象として、作成した教材の試験評価を行った。教材の消化時間およびその理解度を解析し、学習前後の興味・意欲の変化をアンケート集計した。

## 1 Introduction

Since the latter part of the 20th century, there was a considerable growth in the various fields of engineering. As the latest scientific technologies are making remarkable progress and those corresponding academic fields are becoming more advanced and complicated, the gaps between the curriculum in senior high school and the curriculum for engineering course in university are expanding. Moreover, another gap between university education and practical business in company is also broadening. Furthermore, the scientific courses in university are at much higher levels than those of high schools to produce superior scientists or engineers, and it is considered an important problem.

For this reason, it is difficult for first year bachelor students to understand the relation between the current curriculum and the latest technologies. The effect is that first year bachelor students will find it difficult to be motivated in their study and to be interested in science and technology.

Therefore, new learning materials are needed for students to help them to become motivated and interested. The materials also aim in filling the gap between the current curriculum and the latest technology.

Creating web content as an auxiliary learning material is one of the best solutions. It is not a traditional teacher-to-student lecture style, but students can learn by themselves, anywhere, and at any time. For this reason, the contents should be more attractive than a class lecture. Sounds and moving images which are available in the web are persuasive and interactive contents which can make students actively participate can be used.

In this paper, our interest is to create effective e-Learning contents, and to analyze the effectivity. The outline of this paper is as follows. Section 2 describes the selected topics about this theme and introduce the supposed e-Learning contents in detail. Section 3 represents data fitting model, which shows the results of user test. And finally, conclusion and future works are made in section 5 and 6.

## 2 Selection of Study Topics

Requirements of topics are listed as below.

- The topics are familiar to students.
- The topics contains the subjects for 2nd year or later.
- A prerequisite is an understanding of math and science at the senior high school level.

For these reasons, the topic “Voice communication in cellular phone” has been chosen in this study. Since cellular phone is very familiar for students. It also contains the elements of the subjects for 2nd year or later. (Signal processing, digital radio communication). It is possible to describe this topic without any difficult mathematical explanation as well.

The e-Learning material of “Voice communication in cellular phone” has 9 sections.

### 2.1 Detail of Contents

(1)content type: text, PNG image

This section explains the difference between analog and digital values (Figure 1).



Figure 1: Samples of analog clock and digital clock



**(2)content type:** text, GIF animation

This section displays A/D conversion, sampling, and quantization. Students learn what is digital signal (Figure 2).

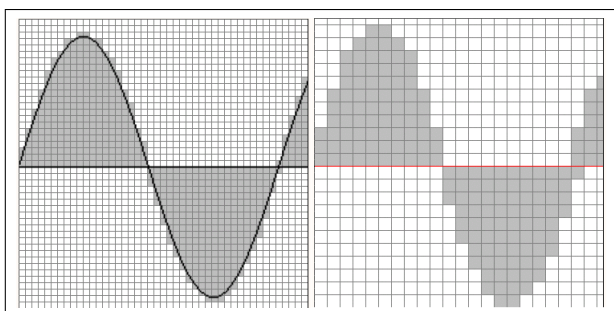


Figure 2: Sampling simulation of sine waves

**(3)content type:** text, GIF animation

This section explains that the quality of voice depends on sampling frequency and quantized bits. It also mentions about the Nyquist-Shannon sampling theorem, but not mathematically.

**(4)content type:** text, wave sound

Related to the previous section, this section shows several kinds of wave sounds (.wav), with each of them having different sampling frequency and quantized bits (Figure 3).

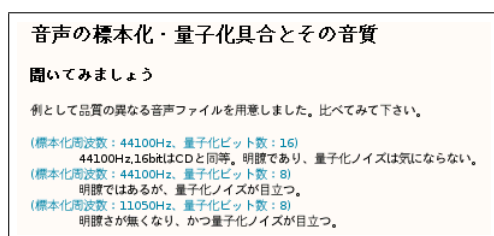


Figure 3: Samples on the difference of sound quality

**(5)content type:** text, Javascript

This section explains what is information quantity. Students can select sampling frequency and quantized bits and calculate the information quantity per a second by Javascript. These sampling frequencies and quantized bits take the realistic values for CD-Audio, DVD-Audio, MD-Audio, and telephone, to make this content more familiar (Figure 4).

**(6)content type:** text

This section explains an easy example of information compression. Students learn the redundancy of information data.

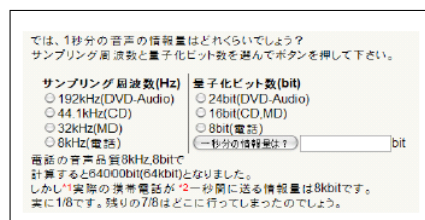


Figure 4: Samples on information quantity calculator

**(7)content type:** text, GIF animation

This section describes the non-linear quantization. The non-linear quantization for digital sound is one of information compression which can reproduce the characteristic of human ears (Figure 5).

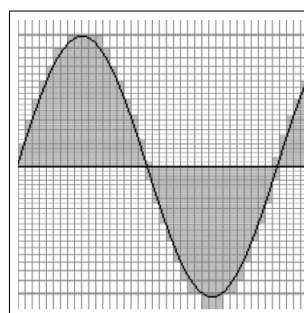


Figure 5: Non-linear quantization

**(8)content type:** text, Png image, sound

This section shows the waveform of a piano song, and makes its sound available (Figs. 6 and 7). Students learn that all the waves consist of various sine waves.

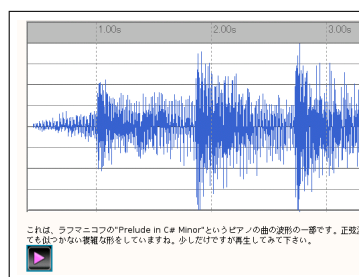


Figure 6: Time domain waveform

**(9)content type:** Java applet

This section has a Java applet which is persuasive for explaining Fourier expansion. It shows a waveform which consists of five sine waves. Amplitude and frequency can of each sine wave be edited independently.

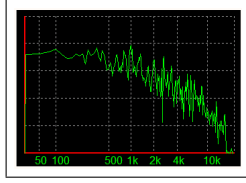


Figure 7: Frequency domain waveform

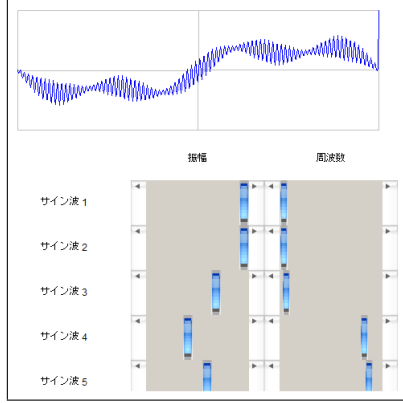
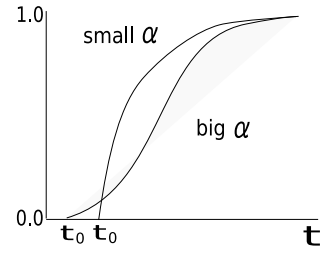


Figure 8: summed up sine waveform

Figure 9: the difference of elapsed time CDF  $F(t)$ 

After obtaining  $\alpha$  and  $\beta$  of each contents, they are normalized to get parameters  $\alpha^*$  and  $\beta^*$ . We can find contents characters by plotting  $\alpha^*$  and  $\beta^*$  in a 2D graph. In Table 1, the contents characteristics by  $\alpha^*$  and  $\beta^*$  are given.

$\alpha^* < 0, \beta^* > 0$ simple, difficult	$\alpha^* > 0, \beta^* > 0$ complicated, difficult
$\alpha^* < 0, \beta^* < 0$ simple, easy	$\alpha^* > 0, \beta^* < 0$ complicated, easy

Table 1: Contents characteristics by  $\alpha^*$  and  $\beta^*$ 

### 3 Analysis of Elapsed Time for Individual Contents

#### 3.1 Data Fitting Model

To analyze the test results, we introduce the Ueno's method [2]. According to Ueno's method, the appearance of elapsed time for studying a certain content follows the gamma distribution as follows (1).

$$f(t) = \frac{t^{\alpha-1}}{\beta^{\alpha}(\alpha-1)!} \exp\left(-\frac{t}{\beta}\right) \quad (1)$$

Where  $\alpha$  is a plain thinking process, and  $\beta$  is a required time for each process.

The parameter  $\alpha$  shows whether the content requires simple thinking or complicated thinking. The parameter  $\beta$  shows the difficulty of the content. Therefore, it can be shown as the equation (2)

$$\alpha\beta = \tau \quad (2)$$

where  $\tau$  is given as the mean of elapsed time for each student.

To fit the collected datas to the model, the CDF of elapsed time  $F(t)$  is

$$F(t) = \begin{cases} 0 & (t < t_0) \\ \int_0^t f(t)dt & (t \geq t_0) \end{cases} \quad (3)$$

Where  $t_0$  shows the theoretical minimum elapsed time of the target learning content.

Figure 9 illustrates the dependence on parameter  $\alpha$ .

Assuming the elapsed time as PDF  $f(t)$ , we can estimate  $\alpha$  and  $\beta$  which are best fit to  $F(t)$ .

#### 3.2 Data Analysis

Test Users	8 members of 1st year bachelor student in Tokyo Tech.
OS	MacOS X Leopard
Web browser	Safari 2.0.1
Sound player	iTunes 7
Java VM	J2SE 5.0 Runtime

Table 2: Environment of user test

Table 2 shows the environment of user test. All the contents do not depend on the platform.

section#	$\alpha$	$\beta$	$\tau(\text{sec})$	$\alpha^*$	$\beta^*$
1	9	8.56	77	0	-0.37
2	10	12.25	122.5	0.1	-0.09
3	14	7.1	99.38	0.5	-0.49
4	4	19.63	78.5	-0.5	0.48
5	13	7.14	92.88	0.4	-0.48
6	2	23.5	47	-0.7	0.78
7	19	3.51	66.63	1	-0.76
8	6	12.48	74.88	-0.3	-0.07
9	4	26.34	105	-0.5	1

Table 3: Result of elapsed time analysis

Table 3 shows the analyzed results of contents. As shown in Table 3,

- High  $\alpha$  appeared in section(3,5,7). These contents require more complicated thinking than other contents.

- High  $\beta$  is also seen in section(4,6,9). These contents requires more difficult thinking than other contents.

[2] Maomi Ueno, Keizo Nagaoka: “Online analysis of elapsed time for e-Learning material by using gamma distribution”, Japan Society for Educational Technology Journal 29(2) 2005.

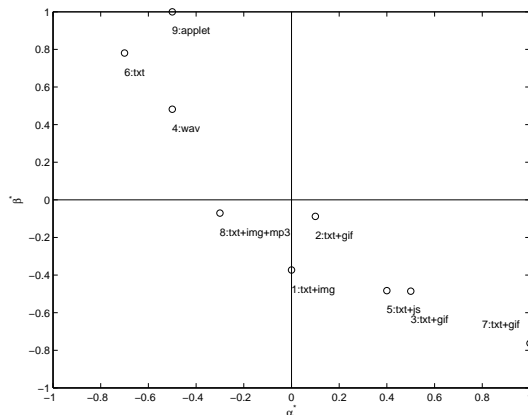


Figure 10:  $\alpha^*$ - $\beta^*$  chart

Figure 10 shows the  $\alpha^*$ - $\beta^*$  chart of all the contents. As shown in figure 10, there are no relation between content type and the parameter  $\alpha^*$  and  $\beta^*$ .

## 4 Summary

The e-Learning web contents which have multimedia and interactivity are created. And through the user test, these contents are analyzed and evaluated by using Ueno's method. The result of the user test revealed the difficulty and elapsed time for each contents.

## 5 Future Works

### More topics and contents

The chosen topic “Voice communication in cellular phone” is an alternative plan of the topics, and further subjects can be added (e.g. electro magnetic wave, introduction of antenna, etc).

### More test users

Because the number of test user is only 8, the data is considered not fully reliable. According to Ueno[2]'s user test, 78 is enough to have the gamma distribution CDF  $F(t)(3)$ , but 15 is not enough.

### Online analysis system

As the number of contents and test users become large, it requires much more time for analysis. But since these contents are on the web. It is able to calculate and analyze the elapse time on the server automatically in real time.

## References

- [1] Walter Dick, Lou Carey, James O. Carey: “The Systematic Design of Instruction”

# Study on applicability of Steel Slag Hydrated Matrix to steel reinforced members under marine environment

Student Number: 05M18047 Name: Tomonari KIMURA Supervisor: Nobuaki OTSUKI

海洋環境下における鉄鋼スラグ水和固化体の有筋部材への適用可能性に関する研究

木村 智成

鉄鋼生産において副産物として生じる製鋼スラグと高炉スラグ微粉末を主要原料とした、環境低負荷の鉄鋼スラグ水和固化体が土木建設材料として開発された。しかしながらその適用領域は港湾土木構造物の無筋部材に限定されている。本研究では、この鉄鋼スラグ水和固化体を有筋部材に適用する為に、物質透過に対する抵抗性及び鉄筋腐食に対する抵抗性に関する検討を行った。その結果、現在使用されている港湾土木構造物の鉄筋コンクリート部材と同等の、①塩化物イオン浸透に対する抵抗性、②酸素透過に対する抵抗性、③固化体内部の鉄筋腐食に対する抵抗性が認められ、有筋部材としての適用可能性が示された。

## 1. Introduction

Recently, Steel Slag Hydrated Matrix (SSHM) has been developed as a construction material for reducing environmental problems. Its main ingredients are pre-treatment slag and blast-furnace slag powder which are by-products of steel making process. In SSHM, the corresponding substitute material for cement is the mix of blast-furnace slag powder, fly ash and slaked lime while the corresponding substitute material for the fine and coarse aggregate is pre-treatment slag. The process used in manufacturing SSHM (**Fig 1.1**) is the same as that for normal concrete.

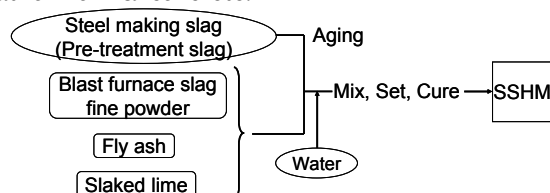


**Fig1.1 Manufacturing process of SSHM**

The application of this material is still limited but it possesses promising features such as ① manufacturing is possible using only by-products, ② good viscosity and high segregation resistance during fresh conditions, ③ high density, and ④ it is environmental friendly. When SSHM is applied to reinforced concrete, there should be a concern about the decrease in durability due to the corrosion of the reinforcement. This is because corrosive materials in SSHM move in a different way and also, the pH of the minute pore solution and the strength are rather low when compared to concrete. However, studies on the durability behavior of SSHM against penetration of

aggressive substances and corrosion are currently limited. Therefore, to clarify the applicability of SSHM in steel reinforced materials under marine environment, this research study presents the following objectives; ①to investigate the penetration of aggressive substances into SSHM, ②to investigate the corrosion resistance of reinforcement inside SSHM, and ③to evaluate the durability of reinforced SSHM.

## 2. Outline of experiments

In this section, the outline of the experiments for this study is presented.

### 2.1 Materials used

In this research, two kinds of pre-treatment slag (K & F) were used for SSHM. The designation names came from the place of origin. Furthermore, in this study, SSHM was compared with ordinary concrete. **Table 2.1** shows the experimental cases and **Table 2.2** shows the specified mix proportions of SSHM and normal concrete used.

### 2.2 Items for measuring the infiltration of substances (Cl<sup>-</sup>, O<sub>2</sub>, CO<sub>2</sub>) into SSHM

Firstly, for both SSHM and normal concrete, the following initial measurements were done; ① penetration depth and ② chloride ion content (JIS A 1154) which are needed to determine the resistance to chloride ion penetration. All these measurements were done after the specimens were subjected to accelerated test by repeated cycles of drying (temperature 40°C, relative humidity 35%) for 60

hours and wetting (soaking in 3% NaCl solution) for 24 hours. Moreover, to compare SSHM with normal concrete, the chloride ion diffusion coefficient was examined using the migration test (JSCE-G571-2003).

Second, to compare the rate of ingress of oxygen in SSHM to that of normal concrete, the limiting current density was measured and the oxygen permeability was calculated.

Lastly, to compare the CO<sub>2</sub> resistance of SSHM with normal concrete, the carbonation depths (JIS A 1153) were measured.

**Table 2.1 Experimental cases**

Case	Binder	W/B (%)	Sand	Gravel	s/a (%)
SSHM (Sign : K40)	Blast furnace slag fine powder	40	Pre-treatment Slag (K)		45
SSHM (Sign : F40)	Fly ash Slaked lime		Pre-treatment Slag (F)		67.2
Normal concrete (Sign : NK40)	OPC	40	Sand	Gravel	45
Normal concrete (Sign : NF40)					67.2

Casting & Curing conditions

- ① temp of 20°C curing in water for 4 weeks
- ② temp of 30°C curing in water for 4 weeks
- ③ temp of 20°C curing in air for 3weeks

**Table 2.2 Specified mix proportions of SSHM and normal concrete**

Steel Slag Hydrated Matrix (Sign : K40)						
Specified mix proportion (kg/m³)						
W/P		40%		s/a		45%
Slaked lime	Blast furnace slag fine powder	Fly ash	Water	Pre-treatment slag (K) 5-20mm	Pre-treatment slag (K) 0-5mm	Admixture
53	297	100	182	1068	874	4.046
Steel Slag Hydrated Matrix (Sign : F40)						
Specified mix proportion (kg/m³)						
W/P		40%		s/a		67.2%
Slaked lime	Blast furnace slag fine powder	Fly ash	Water	Pre-treatment slag (F) 0-20mm		Admixture
53	297	100	182	1867		6.391
Normal concrete (Sign : NK40)						
Specified mix proportion (kg/m³)						
W/C		40%		s/a		45%
Original Portland cement			Water	Gravel 5-20mm	Sand 0-5mm	Admixture
450			182	1068	874	4.046
Normal concrete (Sign : NF40)						
Specified mix proportion (kg/m³)						
W/C		40%		s/a		67.2%
Original Portland cement			Water	Gravel 5-20mm	Sand 0-5mm	Admixture
450			182	609	1247	5.395

### 2.3 Items for measurement of corrosion of steel bar in SSHM

In order to examine the corrosion resistance of steel bar in SSHM, the anodic polarization curve, half cell potential and polarization resistance were measured using electrochemical techniques. Also, the corrosion area (JCI-SC1) and mass loss in the steel bars (JCI-SC1) were determined using destructive methods.

### 3. Examination results on the penetration of aggressive substances (Cl<sup>-</sup>, O<sub>2</sub>, CO<sub>2</sub>) into SSHM

#### 3.1 Results of chloride ion penetration into SSHM

**Fig 3.1** shows the results of the chloride ion penetration test while **Fig 3.2** shows the results of the test for total chloride ion contents. The calculated chloride ion diffusion coefficients from the migration test are shown in **Fig 3.3**.

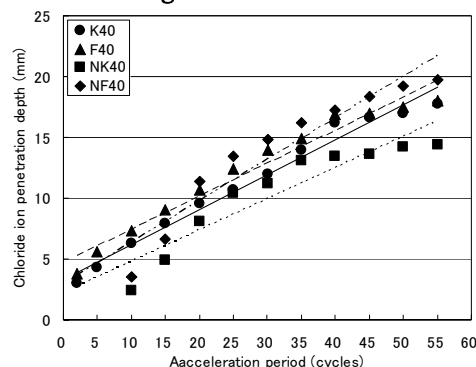


**Fig 3.1 The measurement result of the chloride ion penetration depth**

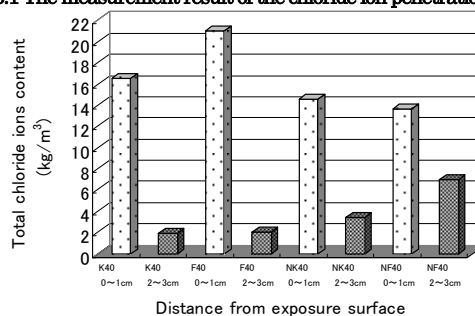


**Fig 3.2 The measurement result of total chloride ions content**

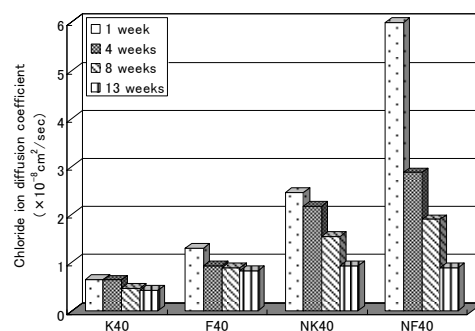


**Fig 3.3 The calculation result of the chloride ion diffusion coefficient**

In each of these examination results, the ingress of the chloride ion for F and NF in which the sand-aggregate ratio is high (67.20%) was large. However for the K and NK in which a lot of coarse aggregates existed and only little amount of mortar was present, the ingress was suppressed. Because it is considered that the chloride ion diffusivity of pre-treatment slag is lower than that of mortar.

The chloride ion content of SSHM is generally higher than concrete when measured near the surface (0-1cm) as influenced by the presence of fine particles of blast-furnace slag powder. However, SSHM exhibited improvement in water-tightness and long term strength at its inner portions (2-3cm). Also, the

chloride ion content at the interior of SSHM was less than that of concrete.

### 3.2 Results of oxygen permeability test in SSHM

**Fig 3.4** shows the calculation result of the oxygen permeability test while undergoing the accelerated exposure.

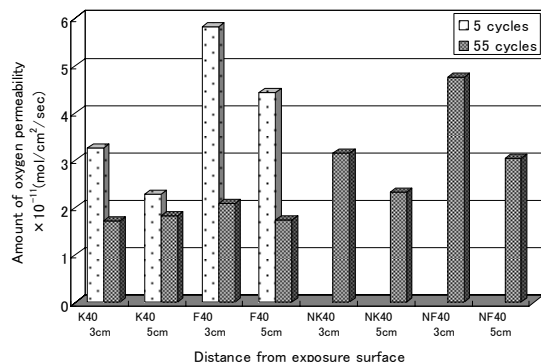


**Fig 3.4** The calculation result of the amount of the oxygen permeability

The values of oxygen permeability calculated after 55 cycles are much lower compared to those obtained after 5 cycles. This is caused by the decrease in the micro voids inside the SSHM as time passed by. This improved behavior in oxygen permeability can influence the corrosion of steel bar in SSHM as will be discussed in the following sections.

### 3.3 Results of carbonation test in SSHM

**Fig 3.5** shows the depth of carbonation versus elapsed time during the acceleration test. Resistance against carbonation for SSHM was usually lower than that of concrete. This phenomenon is due to the consumption of calcium hydroxide (supplied by slaked lime) by the blast-furnace slag powder and fly ash during the pozzolanic reaction. Therefore, it is necessary to take care of carbonation of SSHM especially in atmospheric zone.

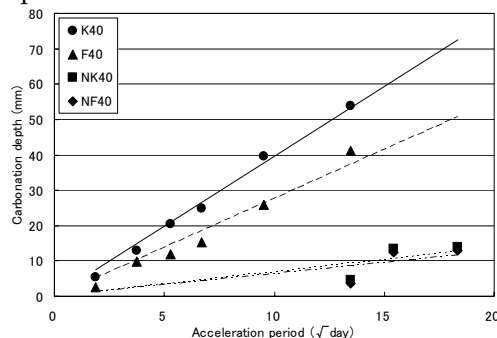


**Fig 3.5** The measurement result of carbonation depth

## 4. Examination results of resistance to corrosion of steel in SSHM

### 4.1 Results of steel bar corrosion by electrochemical

nondestructive test

**Fig4.1** shows the measurement result of the anodic polarization curve of SSHM (K40) and normal concrete (NK40) after 55 cycles of acceleration test. The state of passivity was judged by the grade of passivity according to past research [3] in terms of the anodic polarization curve. The higher grade indicates the better passivity.

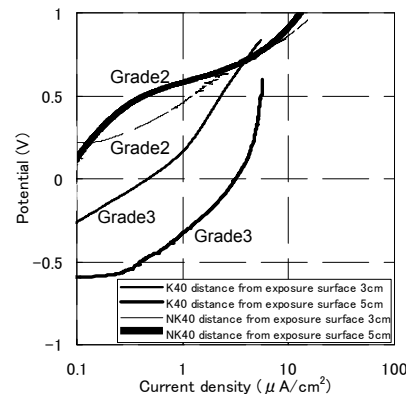


**Fig 4.1** The measurement result of the anodic polarization curve

The results indicated a better passive state existing in SSHM when compared with concrete. This can be explained by the following ① control of cathode reaction in steel bar by consumption of dissolved oxygen that infiltrated from surface of SSHM by the corrosion reaction of pre-treatment slag, ② control of dissolution reaction in steel bars by pre-treatment slag binding with chloride ions, ③ improvement of steel bars protection performance by demonstrating good viscosity and good material separation resistance of fresh SSHM.

On the other hand, an accurate value was not determined through the half cell potential and polarization resistance measurements for SSHM. This is because of the early corrosion of pre-treatment slag itself that occurred at the surface part which had some effects in the measurements.

### 4.2 Results of steel bar corrosion by physical destructive test

**Fig 4.2** shows the mass reduction ratio of steel bar by the acceleration test after 25 cycles has passed.

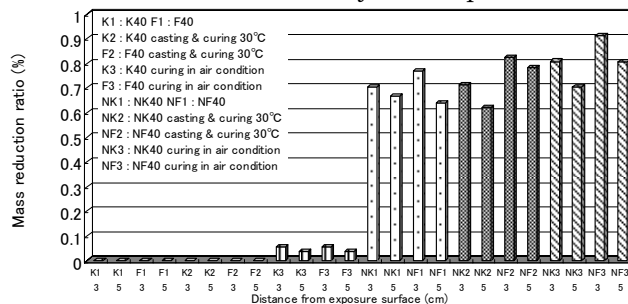


**Fig 4.2** The calculation result of the mass reduction rate

The specimen used for this experiment is a rectangular prism with horizontal steel bars. The specimens were dosed with  $10\text{kg/m}^3$  chloride ion before mixing. This was done to further accelerate the attack of chloride ion and shorten the infiltration time. The results show that after 25 cycles, the progress of corrosion was well controlled in SSHM specimens. The reason for this is similar to those already explained above.

### 5. Durability evaluation of SSHM as material with steel reinforcement under marine environment

In this chapter, the prediction of deterioration due to chloride attack when SSHM is used as material with reinforcing steel is discussed.

In order to predict the deterioration of steel reinforced members due to chloride attack, it is basic to determine the length of time for each deterioration stage: the incubation period, the propagation period, the acceleration period, and the deterioration period. Therefore this research tried to determine the incubation and propagation period using the results obtained above. The incubation period was calculated using the chloride ion diffusion coefficient of the specimens cured for four weeks (Fig. 3.3), the generalized equation of the Fick's second law and the chloride concentration limit of  $1.2\text{kg/m}^3$  around the steel bar (JSCE). While the propagation period was calculated by using results of mass reduction due to corrosion, the equation from JCI-SC1 for mass loss in  $\text{mg/dm}^2/\text{day}$  and the corrosion mass limit of  $10\text{mg/cm}^2$  which is generally used as the quantity of corroded mass of steel at the occurrence of crack(JSCE). Table 5.1 shows the calculation result of the average ratio of deterioration periods between SSHM and normal concrete.

**Table 5.1 The comparison of deterioration periods between SSHM and normal concrete**

	SSHM/Normal concrete
Incubation period	3.24
Propagation period	4.92

The results show that SSHM had longer periods of incubation and propagation compared with concrete. This shows that the use of SSHM as substitute to concrete in steel-reinforced structures under chloride attack is quite feasible and also the service life of the structure possibly becomes longer. Therefore SSHM can be a substitute material in existing reinforced structures such as caissons, cellular blocks, quays and mooring-posts which structures that are highly used in marine environments.

To further examine the application of SSHM

with reinforcing steel bar under marine environment, all examinations and tests in the future should be performed on specimens exposed to actual marine environments for longer periods of time. This can allow for a more quantitative evaluation of the long term durability of SSHM compared with existing concrete structures. And, also it is necessary to study the durability using other deterioration mechanisms besides chloride attack.

### 6. Conclusions

The conclusions of this research are shown as follows.

1. The resistance to chloride ion and oxygen penetration of SSHM is equal or even better than normal cement based materials having the same mix proportion and curing condition under marine environments. This result is clearer in the interior of the specimen. On the other hand, it is necessary to consider appropriate measures for the use of SSHM against carbonation, because the carbonation depth of SSHM is larger than normal concrete materials.
2. The state of passive film of the steel bars that influences corrosion in SSHM under marine environment is at least equal to or even better than the normal concrete materials having the same mix proportion and curing condition.
3. The duration of the incubation period and the propagation period of corrosion of steel in SSHM under chloride attack is over 3 times longer than normal concrete having the same mix proportion and curing condition. Therefore it can be selected for use as a substitute material for existing reinforced structures in regions where its supply is highly available and under marine environment.

### References

- [1] Coastal Development Institute of Technology, "Steel Slag Hydrated Matrix technical manual – Use of Effective Technology For Pre-treatment Slag -", Coastal Development Institute of Technology, 2003. (in Japanese)
- [2] The Japan port and harbor association, "Standards and explanations for the technology of facilities in harbors", The Japan port and harbor association, 1999. (in Japanese)
- [3] N. Otsuki, "Research on corrosion of reinforced concrete under marine environment", Tokyo Institute of Technology degree thesis, 1986. (in Japanese)
- [4] K. Kawata, S. Sakashita, Y. Hamazaki, and K. Sugimoto, "Corrosion prevention of reinforcement steel in mortar through small metal piece additions", Concrete Journal, Vol.38, No.2, pp. 29~33, Feb. 2000. (in Japanese)

## A study on gas-liquid two-phase flow patterns in rectangular micro channels

Student Number: 05M18053 Name: Shintaro KOBAYASHI Supervisor: Shiro YOSHIKAWA

### 矩形微小流路における気液二相流の流動状態に関する研究

小林 慎太郎

近年、微小流路を有するマイクロ化学プロセスにおける反応・分離に関する研究が盛んに行われている。流路内の流動状態を制御することはこれらの装置の設計上、重要である。本研究では、矩形微小流路に気体と液体を同時に流し、その流動状態を観察し、分類を行った。流動状態に関するパラメーターとして表面張力、粘度、流量、圧力を挙げ、流動状態を決定する重要な因子となる無次元数に基づいた流動状態図の作成を行った。さらに、操作条件と流動状態の間の関係について新たな知見を得た。

#### 1. Introduction

There are many kinds of equipment, where gas and liquid contact with each other, for instance a chemical reactor, a cooling tower, ink-jet systems, spray systems and so on. In the equipment, transport phenomena between gas and liquid phase should be important. The phenomena should be discussed on the basis of the pattern of the Gas-liquid two-phase flow.

Recently, various kinds of micro chemical process with micro channel have been studied. In a micro channel reactor, temperature and residence time are easily controlled. As a result, the selectivity of the reaction is expected to be high. Because of the high selectivity, the micro chemical processes would be utilized in the pharmaceutical industry and the cosmetic industry even if the amount of the products might not be so large.

Gas-liquid two-phase flow reactors would be important also in the micro chemical process and some devices have been studied. As described above, it is important to get information on the flow patterns in the Gas-liquid two-phase reactor in order to estimate the performance of the device. There is little information for controlling the flow patterns with the operational conditions though it would be indispensable for the process very useful. The purpose of this study is to discuss the

important dimensionless numbers for the transitions of the flow patterns and to get the flow pattern map of Gas-liquid two-phase flow using dimensionless numbers as coordinates.

#### 2. Experiments

Figure 1 shows the experimental apparatus schematically. Nitrogen gas was fed by a gas cylinder. Flow rate was controlled by a regulator and a needle valve. The gas piping was made of stainless steel. On the other hand, liquid was fed with a fixed quantity by micro-feeder. The water feeding pipe was made of PTFE. The liquid was deionized water or 10wt aqueous ethanol.

Figures 2 and 3 show the designs of the test sections. They are made of glass. The channel height of each test section was less than mm order. The channel length of each test section was enough long from the inlet length, so it is thought that the flow were fully developed flow. Test section was put horizontally, so it is thought that the influence of gravity was able to be ignored.

In the experiment, at first, the test channel was filled with liquid. After that, nitrogen gas was fed to the test channel. The experiments were carried out under the condition of various gas and liquid flow rate. The operation patterns are summarized in Table 1.



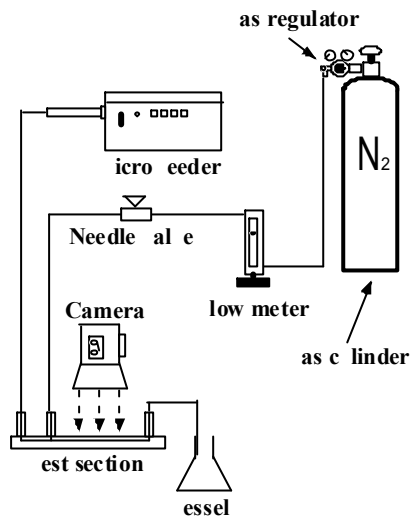


Figure 1. Schematics of the test apparatus.

Table 1. Operation patterns.

	Test section	Liquid inlet	Gas inlet
Experiment 1	type	A	B
Experiment 2	type	B	A
Experiment 3	type	A	B
Experiment 4	type	B	A

In Experiments 1, 2, and 4, it was difficult to get the stable flow pattern. In Experiment 3, three flow patterns were observed.

Figure 4(a) shows the Intermittent flow. It seems that there are large gas plugs in the liquid phase. Figure 4(b) shows the Separated flow. It seems that gas-liquid interface seems smooth. Figure 4(c) shows the Annular flow. It seems that gas-liquid interface becomes turbulent.

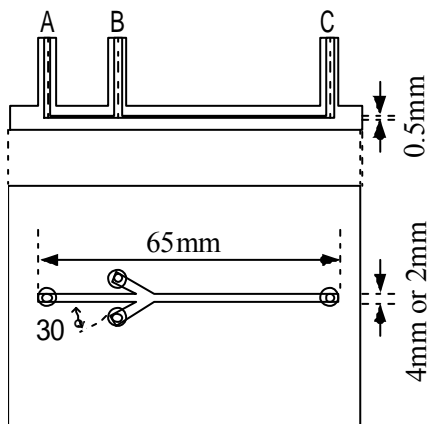


Figure 2. Test section type .

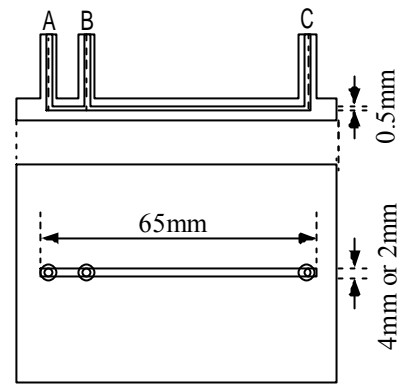


Figure 3. Test section type .

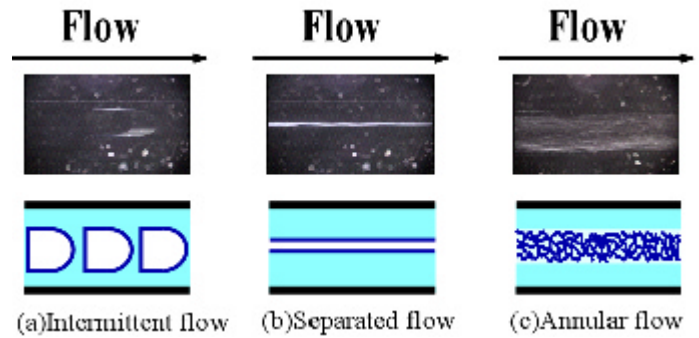


Figure 4. Schematics of the test sections.

### 3. low patterns and transition

There should be many factors, which influence the flow patterns. But, it is impossible to take all of the factors into account in making the flow pattern map. The most important ones were discussed in the following from three view points.

#### 3.1 elocit and inter als o plugs

Figure 5 shows transition from Intermittent flow to Separated flow. Thinking about such a state and assuming that the intervals of gas plugs  $l_g$  and the length of the plugs  $l_p$  are constant, the time interval of the plug  $T$  is expressed by the following equation.

$$T = \frac{l_g + l_p}{u_p} \quad (1)$$

$u_p$  shows the velocity of the plug. The superficial velocity of gas  $u_g$  and that of liquid  $u_l$  are defined as follows.

$$u_g = \frac{l_g}{T}, \quad u_l = \frac{l_p}{T} \quad (2)$$

$q_g$ ,  $A_l$  show the volumetric flow rate and  $A_l$  is the area of the cross section of the channel. A volume of a plug is expressed as follows.

$$V_g = q_g T \quad (3)$$

On the assumption that the shape of a plug is half spheroid, the volume of a plug is expressed as follows.

$$V_g = \frac{\pi}{12} x^2 L_g \quad (4)$$

$u$  shows the relative velocity between the plugs and superficial velocity of the two-phase mixture. So,  $u_p$  is written by

$$u_p = q_g / A_l = u \quad (5)$$

From Eqs. (1),(3),(4) and (5),  $A_l$  is expressed as follows.

$$A_l = \frac{\pi x^2}{12} \frac{q_g}{u} \quad (6)$$

It is necessary for the transition from Intermittent flow to Separated flow to be the condition  $A_l = 0$ . When  $A_l = 0$ , Eq. (6) becomes as follows.

$$0 = \frac{\pi x^2}{12} \frac{q_g}{u} \quad (7)$$

Eq. (7) means that  $\frac{q_g}{u}$  has significant effects for the transition

of flow patterns not to speak of  $q_g$ ,  $A_l$ .

### 3.2 Shear stress

It seems that the shear stress on the gas-liquid interface between gas and liquid has effects for the transition of flow patterns. Figure 6 shows the flow of gas and liquid between two flat plates. Thinking about such a state, the shear stress  $\tau_{yx}$  on the interface is written by the pressure gradient, the viscosity  $\mu$  and the thickness of gas phase and liquid phase  $a, b$ .

$$\tau_{yx} = \frac{1}{2} \frac{b^2 \mu_g}{b \mu_g} \frac{a^2 \mu_l}{a \mu_l} \quad (8)$$

Eq. (8) means that  $\mu$ , especially viscosity of liquid  $\mu_l$ , has significant effects for the transition of flow patterns.

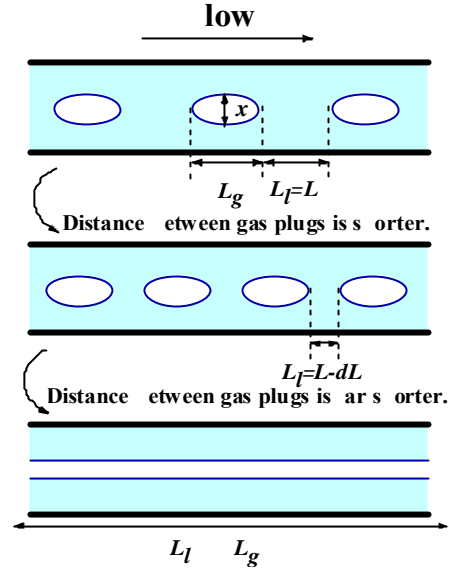


Figure 5. Transition from Intermittent flow to Separated flow.

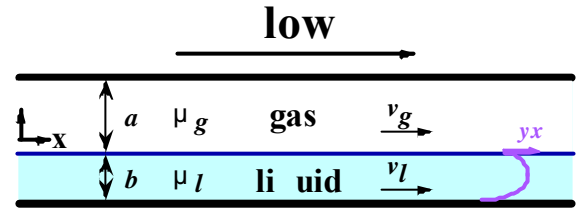


Figure 6. Flow of gas and liquid between two flat plates.

### 3.3 Surface tension

Figure 7 shows the growth of a plug. Thinking about such a state, according to the Laplace-Yang equation,  $P_{in}$  and  $P_{out}$  are the pressures inside and outside of a plug.

$$P_{in} = P_{out} + \frac{2\sigma}{r} \quad (9)$$

The pressure  $P$  may be written by the characteristic length and the characteristic velocity.

$$P_{in} = P_g + \frac{\mu_g}{2} \frac{v_g}{r}, P_{out} = P_l + \frac{\mu_l}{2} \frac{v_l}{r} \quad (10)$$

From Eqs. (9) and (10), the radius  $r$  of a plug is

$$r = \frac{2\sigma^2}{\mu_g v_g - \mu_l v_l} \quad (11)$$

Eq. (11) means that  $\sigma$  may have effects for the transition of flow patterns.

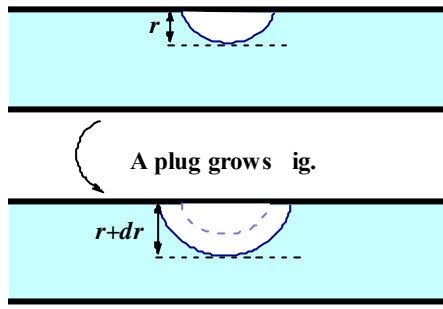


Figure 7. Growth of a plug

## 4. low pattern map

### 4.1 Dimensionless numbers

It seems that pressure  $P$ , density  $\rho$ , viscosity  $\mu$ , velocity  $U$ , surface tension  $\sigma$  and a characteristic length of the channel  $D$  are the important parameters for the transitions of flow patterns. With these parameters, the radius of a plug is described as follows.

$$\frac{P_g D}{\sigma}, \quad e, \quad Ca, \quad \frac{P_l D}{\sigma}, \quad e, \quad Ca, \quad \frac{\mu}{\rho U D} \quad (11)$$

$$e = \frac{\rho U^2 D}{\sigma}, Ca = \frac{\mu}{\rho U D} \quad (12)$$

$e$  shows the Weber number, and  $Ca$  shows the Capillary number. From Eq. (12), following equation is derived. There is the following relationship among  $e$ ,  $Ca$  and  $Re$ .

$$\frac{e}{Ca} = \frac{\rho U^2 D}{\mu} \frac{D}{\sigma} = \frac{\rho U D}{\mu} Re \quad (13)$$

$e$  shows the Reynolds number. By dimensional analysis, it is clear that  $e$ ,  $Re$  and  $Ca$  should be used in the flow pattern map.

### 4.2 Dimensionless low pattern map

Figure 8 shows the flow pattern map. The abscissa is  $e$  and the ordinate is liquid phase Reynolds number  $Re_l$ . As a result of some trials in making maps, it appeared that  $e$  was better than  $Ca$  in correlating the experimental results. This result suggests that the relationship between surface tension and inertia force is more important than the effect of viscous force in the range of the experimental in this study. The solid lines in the map show the boundary of the area of each flow pattern. The transitions from Intermittent flow to Separated

flow seems to depend on the inertia force of gas phase. The transition from Intermittent flow to Annular flow seems to depend on the inertia force of gas phase and liquid phase, respectively. In the size of this study, inertia force is still dominant. It seems that in the channel which is smaller than the channel of this study, viscous force is dominant. When viscous force is dominant,  $Ca$  might be better than  $e$ .

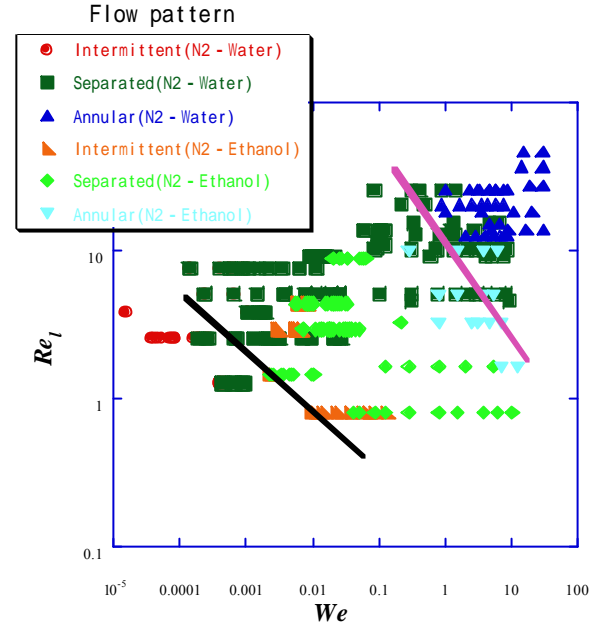


Figure 8. Dimensionless flow pattern map.

## 5. Conclusions

The important factors in the transition of the patterns of the Gas-liquid two-phase flow in a micro rectangular channel were discussed.

Though two-phase flow has various parameters, in this study, the flow pattern map was able to be made using  $Re_l$  and

$e$  as the coordinates. As a result, the effect of inertia force is more important than viscous force in the experimental conditions.

## 6. References

- [1] 岡本秀穂, 橋爪新太, 住友化学 2001 - マイクロリアクタの現状と展開 - 合成実験、分析、製造への新規アプローチ -, (2001), 32-45
- [2] 植田辰洋, 気液二相流 - 流れと熱伝達 - 第2版, 養賢堂(1989)
- [3] Tohru Fukano and Akira Kariyasaki, *Characteristics of gas liquid two phase flow in a capillary tube*, Nuclear Engineering and Design, volume 141, Issues 1-2, June 1993, Pages 59-68

# IN-SITU SOIL REMEDIATION BY SEDIMENTATION METHOD ~HEAVY METAL IONS' ADSORPTION CHARACTERISTICS ON SOIL AND ADSORBENTS~

汚染された砂質地盤の原位置攪拌洗浄

Student Number: 05M18076 Name: Ryoichi SUGA Supervisor: Hideki OHTA and Pipatpongsa THIRAPONG

菅 良一

土壌汚染対策法が施行されて以降、様々な浄化工法が提案されてきたものの、精度とコストの両面を満たす工法は数少ない。そこで、本研究では安価ですむ原位置地盤浄化工法の提案を目的としており、著者の研究はその基礎となるものである。まず人工的に重金属汚染させた土を、水、そして界面活性剤を加えた水とで洗浄することで、重金属の脱着特性を調べた。次いで、洗浄水中の重金属を活性炭とゼオライトで回収することで、それらへの重金属の吸着特性を調べた。その他、SSE, BETなどの化学的なアプローチにより、これらの重金属の吸着・脱着特性の実験結果を理論的に実証することに成功した。

**Key Words :** adsorption, desorption, in-situ, heavy metal, biosurfactant, activated carbon, zeolite

## 1. INTRODUCTION

In July 2004, Tokyo Ohta Ward, unacceptable level of contamination (lead, oil, and trichloroethylene) was detected from the ground owned by one of the factories which was dealing with automobile manufacturing. Ohta Ward is well known for the large number of small factories and therefore there is a possibility that contaminants are also detected from other areas in Ohta Ward, which is undesirable for both land owners and also residents near the sites. However not much effort has been made for prevention and remediation of soil contamination so far. What is worse, it is said that some of the land owners are hiding contaminated land and leave it even when they sell it to others. This is simply because the cost of remediation is unaffordable for them.

Therefore the purpose of this study is to propose a new affordable soil remediation method. To keep the cost low, the method should be performed on site and our target will be contaminated ground under small factories, especially the ones dealing with plating. Since the major contaminants detected from plating factories are heavy metal, our target contaminants in this paper will be limited in four Heavy Metals (HMs) (Copper, Lead, Zinc and Cadmium).

## 2. CHARACTERISTICS OF THE SEDIMENTATION METHOD

### (1) General Description

To make the remediation cost-effective, in-situ soil remediation method has been proposed. This sedimentation method can be divided into 3 parts: homogeneous adsorption, Sedimentation, Removal of

fine soil particles, Desorption and Collection of HM ions (See Fig.1).

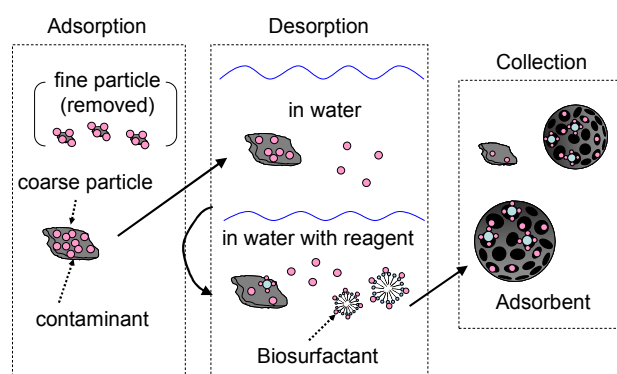


Fig.1 Process of the Sedimentation Method

### (2) Homogeneous Adsorption

Since HM ions generally exist only in the area around 3 to 5 meter from the ground surface (See Fig.2), HM concentrations in soil in the casing are not homogeneous. All the soil particles in the casing should attach to the HM ions homogeneously so that the adsorbed HM ions can be removed efficiently as explained in the following sections. In order that agitate the suspension in the casing for a while.

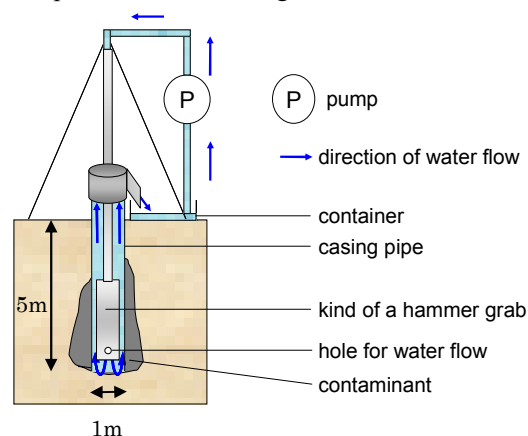


Fig.2 Overall View of the Apparatus

### (3) Removal of Fine Particles

Only the top layer of the sediment composed of fine particles holding high percentage of contaminants in the hole is taken out. According to the results of sieving and sedimentation analysis that the author has conducted (Results are as shown in Fig. 3), fine particles have far larger surface area per gram than coarse particles. See a red arrow in Fig. 3, representing diameter of 0.074mm which is the boundary diameter between fine and coarse particles in geotechnical fields. If removing only a part of the soil, namely 10 percent of soil in weight settled at the top of the sediment, it will be a great saving of time and cost (See Fig. 4)

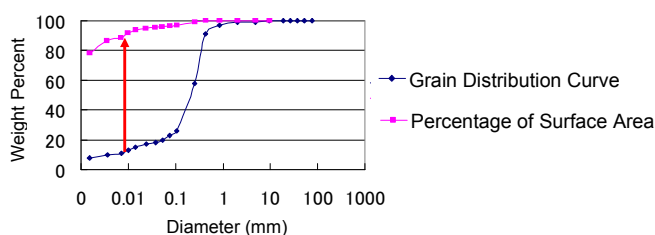


Fig. 3 Grain Distribution Curve

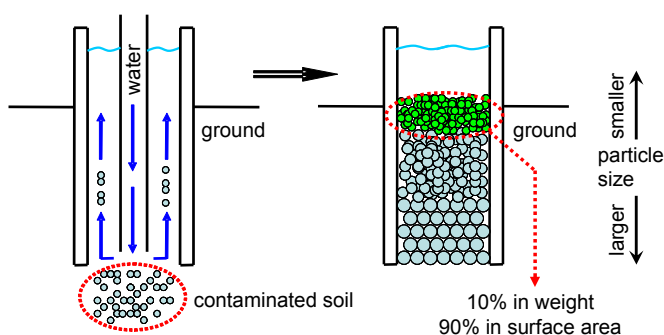


Fig. 4 Removal of fine particles in top layer

### (5) Desorption of HM Ions

it seems to be impossible to clear the environmental standard only with those processes. Hence, in this section, our focus is put on understanding of the HM desorption behavior from soil surface and in the next section, those released ions are going to be collected by using adsorbents. It is well known that biosurfactant is highly effective in removing oil from the surface of particular material as one can see in an advertisement of detergent. To enhance the desorption, therefore, we adopt biosurfactant.

### (6) Collection of HM ions

In this section, collect all the ions released into wash water in a proper way. There are several types of adsorbents suitable for this case. The most common adsorbent of all is "Activated Carbon (AC)", which is the material mainly made of carbon and has a lot of pores on its surface. AC is capable of collecting object

matter by holding them into the pores. There is no guarantee, however, that AC is able to collect all sorts of heavy metal, and therefore another type of adsorbent, zeolite, is also adapted.

## 2. EXPERIMENTAL RESULT AND DISCUSSION

### (1) Artificial Contamination of the Soil Sample

The uncontaminated soil sample was put into 20 mill molar (mM) solution of nitrate salts;  $\text{Cu}(\text{NO}_3)_2$ ,  $\text{Cd}(\text{NO}_3)_2$ ,  $\text{Pb}(\text{NO}_3)_2$  and  $\text{Zn}(\text{NO}_3)_2$ . According to Reuss and Johnson, the nitrate ion is not significantly adsorbed by soil fractures and is highly mobile. Hence, the presence of  $\text{NO}_3$  anion does not influence on the behavior of HM ions. The soil-nitrate suspension was aged in a reciprocating shaker for 16 days (See Fig. 5). The final concentrations of each HM ion after 16 days exposure in the reciprocating shakers are  $\text{Cu}=2225\text{ppm}$ ,  $\text{Pb}=5102\text{ppm}$ ,  $\text{Zn}=1101\text{ppm}$  and  $\text{Cd}=1393\text{ppm}$ .

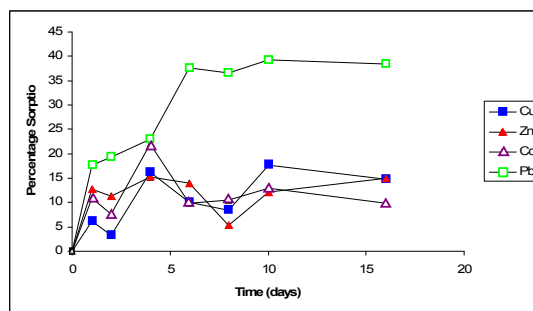


Fig. 5 Daily Changes in the percentage of HM adsorption

### (2) Removal of the Upper Layer

Agitate and mix the suspension composed of artificially contaminated soil and deionized water for several minutes and later leave the measuring cylinder, and then the double soil layer can be observed; fine particles on top and coarse particles at bottom (See Fig. 6).



Fig. 6 Two layers of sediment after agitation

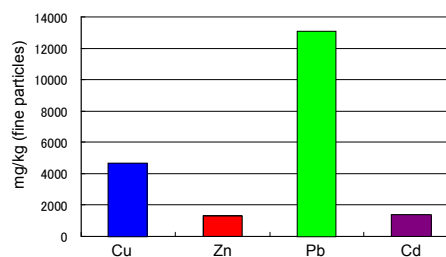


Fig. 7 Concentration of HM ions in fine soil

### (3) Water Wash and Biosurfactant Wash

In order to detach the HMs from soil surface, two methods were proposed. The first one is just simply add water and agitate the suspension with sufficient air applied by air pump. From now on, we call this process and water added “Water Wash” and “Wash Water”, respectively. The second method is add biosurfactant (in our experiment, saponin) and enhance the efficiency of desorption. The following graphs show the concentration in wash water.

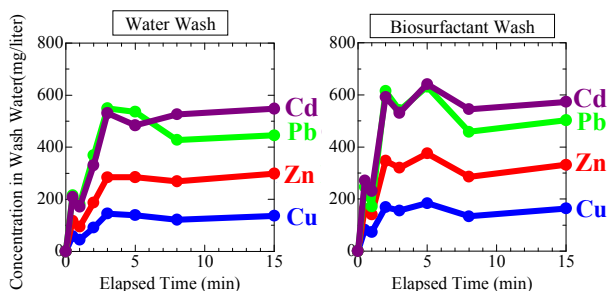


Fig. 8 HM concentration in wash water

1. Even after biosurfactant added, there is no distinct difference found in the concentrations.
2. The initial part of inclination of the graph in biosurfactant wash is steeper than that of water wash, which indicates that desorption process with biosurfactant can reach the equilibrium condition faster than without it

### (4) Collection Process

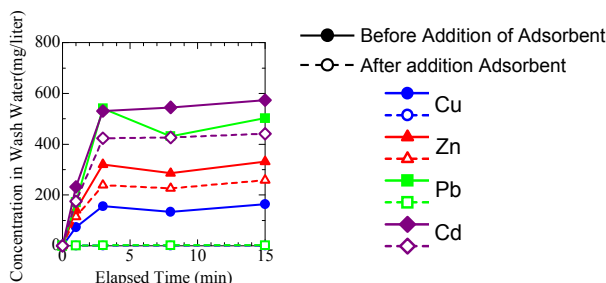


Fig. 9 HM concentration in wash water after adsorbent wash

The figure indicates each HM ions concentration after AC wash and how much AC is effective in the collection of HM ions. However, AC turned out to be effective only in the collection of  $\text{Cu}$  and  $\text{Pb}$  and any distinct changes in the concentrations of  $\text{Zn}$  and  $\text{Cd}$  ions were not found. It is possible to say that AC is effective only in  $\text{Cu}$  and  $\text{Pb}$  ions, which is consistent with the results from other studies, while only 10 to 20 % of the  $\text{Zn}$  and  $\text{Cd}$  ions were collected. Even after the addition of zeolite, the result did not change significantly.

### (5) Balance of HM transfer

At this moment, it seems that these laboratory results that are still higher than environmental standard may not live up to people's expectations, however, this research has just recently launched and at least we

found out which part of procedure can be and must be improved. For HM existing in coarse particles, all the fine particles cannot be removed with one time washing because in the sedimentation process, the degree of separation of coarse and fine particles is not perfect and not all fine particles settle on top of the sediment. Therefore, if the water wash is repeated and fine particles are taken out continuously for several times, it is expected that fine particles holding higher concentrations of HM ions in bottom layer transfer to top layer progressively, which will be removed and disposed. One more thing, for ions in wash water, is that zeolite, which is the adsorbent we adapted after AC, turns out to be ineffective in collecting HM ions at least Cu, Zn, Pb, and Cd. Hence, another effective adsorbent must be found.

Balance Sheet	Initial Condition
(mg)	total (mg)
Cu	44.5
Zn	22.0
Pb	102.0
Cd	27.9



(mg)	Coarse (mg)	Wash Water (mg)
Cu	25.2	0.02
Zn	5.3	10.33
Pb	48.2	0.07
Cd	1.8	17.67

Fig. 10 Balance of Heavy Metal transfer

## 3. SOIL CHARACTERISTICS

### (1) Carbon Content

Not only the surface area, but the presence of carbon content also highly influences on the adsorption and desorption characteristic. It is clear that fine particles have more ability for adsorption than coarse particles.

%	Fine Particles	Coarse Particles
H	0.73	0.18
C	1.9	0.08
N	0.18	0.04

$\mu$ gram	Fine Particles	Coarse Particles
Sample Weight	8781	12072
Content		
H	64	21
C	167	10
N	16	5

Fig. 11 Carbon content

### (2) BET Analysis

One of the main features of this remediation method is to take advantage of large surface area of fine particles. Hence, there is a need to determine how larger the area of fine particles per 1g than that of coarse ones. The result might be surprising. 1 gram of fine particles is corresponding to around 28  $\text{m}^2$  of surface area, while



around  $5\text{m}^2$  is for coarse particles. It is important to keep in mind that the surface area of fine particles can be much larger if the separation is more perfect.

Size	BET Surface Area
Fine Particles	$27.831\text{m}^2/\text{g}$
Coarse Particles	$4.964\text{m}^2/\text{g}$
All (Fresh)	$8.007\text{m}^2/\text{g}$
All (Contaminated)	$9.804\text{m}^2/\text{g}$

Fig. 12 The result of BET Analysis

### (3) SEM Analysis

Sequential Extraction Method (SEM) is usually conducted to evaluate the speciation of particulate metals. As a result of SEM analysis one can observe how large or small the bonding strength is, how mobile or immobile trace metals in soil are and how likely the trace metals influence on the environment.

Fig. 13 indicates that Cd ions can be easily released into water (soluble) or just never be adsorbed to soil surface. For Zn, besides exchangeable fraction, carbonate fraction and Fe-Mn matter fraction was also detected and accounted for 30 to 50% of all. The second fraction, namely carbonate fraction is still regarded as highly soluble. Hence, it can be said that Zn are still relatively soluble. For Pb, although exchangeable fraction is still dominant of all fractions, carbonate fraction and Fe-Mn Oxide fraction also constitute large share of all fraction. Fe-Mn Oxide is regarded as immobile part compared to other two above fractions. Therefore, Pb is partially soluble but some of ions possibly stick to soil surface. For Cu, Fe-Mn Oxide fraction is dominant and it accounts for around 70 to 80% of all. Soil bound to Fe-Mn Oxide and Organic matter is hardly released into water, that is, immobile. Therefore, it can be concluded that Cu is less soluble and hardly released into either water wash or biosurfactant wash.

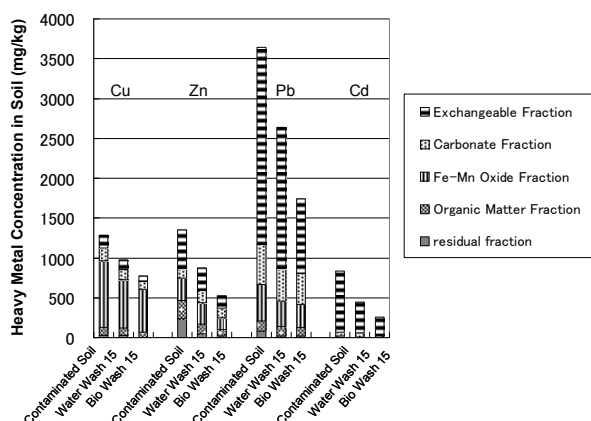


Fig. 13 The result of SEM analysis

## 4. CONCLUSION

1. According to the results from sieving and sedimentation analysis, it was discovered that 10% of all object soil in weight, which is mainly composed of

fine particles, accounted for 90% in surface area. If all the fine particles holding high concentrations of HM ions are removed, in the last result, around 90% of HM ions in target area can be removed.

2. Adsorption and Desorption characteristics of 4 HM were revealed as follows

**Cu:** mostly exists in soil particle meaning Cu has large adsorptive ability. However, Cu in coarse particles needs to be transferred to fine particles, otherwise most of Cu keep remain in coarse particles that we do not take out from the casing. Repeat the sedimentation process until perfect separation is achieved. As for AC wash, Cu ions were dramatically adsorbed to AC.

**Zn:** spread out averagely to soil and wash water. Any significant result was not obtained from water, biosurfactant, and AC wash, and therefore, perfect separation should be achieved and another effective adsorbent is needed.

**Pb:** The same tendency with Cu was observed.

**Cd:** It seems that Cd ions are easily and readily released from soil particles from the release efficiency obtained from water and biosurfactant wash, but actually it does not. Cd ions are apparently released, but in fact Cd ions never attached to soil surface and just stay in wash water all the time, that is, Cd does not have adsorptive ability to soil surface nor AC.

3. It is discovered that large amount of carbon content, which is deemed to be highly influential to HM adsorption, was detected in fine particle, moreover, 1 gram of fine particle possess  $28\text{m}^2$  of surface area. Consequently, these results indicate that focusing on fine particles for remediation is making a point and even fabulous idea. The result from SEM analysis was consistent with the adsorption and desorption characteristics mentioned above, and confirms the reasonableness of the laboratory experiment's results.

## 5. REFERENCE

- 1) BUDIANTA Wawan, SALIM Chris: LABORATORY EXPERIMENT ON THE REMEDIATION OF METAL-CONTAMINATED SOIL BY IN-SITU SOIL WASHING, 2006
- 2) Gillman, Sumpter: CEC Determination by the  $\text{BaCl}_2$  compulsive Exchange Method, 1986
- 3) Kyung-Jin Hong: Application of Plant-Derived Biosurfactant to HM Removal from Fly Ash and Soil, 2000
- 4) Tessier et al: Sequential Extraction Protocol for Analysis of HM Speciation in Soils and Sediments, 1979

# E C L I C A L E E C E A I R A L C A N E C A E D L I C R N L A C E A A C E N

Student Number: 05M18082 Name: Haruna SUZUKI Supervisor: Satoshi FUJII

## 土木事業による人々の行動の変化が地域への感情に与える影響に関する研究

鈴木春菜

人々がもつ地域への愛着の存在は、地域活動への協力を促すなど地域計画に大きな影響を及ぼすことが知られている。しかしながら、地域愛着の醸成過程、特に土木施策によってその過程にどのような変化がもたらされるかについては、十分に検討されていない。本研究では、心理学実験データに基づき、交通行動による「風土」への接触の程度の変化が長期的に地域愛着に与える影響、及び消費行動が地域風土との関わりや地域への感情に及ぼす影響について検証した。

## 1 Introduction

Many studies revealed that those who have positive attitude toward the place tend to have sense of responsibility to the place or the regional community and actively engaged in regional activities [1]. “Place attachment”, one of the major concepts of human emotion to the place, is studied in various fields. They showed that place attachment is affected by many factors, Individuality like age, sex and religion, surroundings like public safety, Individual behavior like daily activity[2].

Because Public works typically change people’s surroundings, place attachment may be indirectly influenced by public works. In turn, place attachment would affect people’s public opinion and public behavior that may have substantial effects on the content of public works. Thus, place attachment is essential for deep understandings of consequences and determinants of public works. In spite of such importance, place attachment has not yet well studied in planning of public works. With this recognition, this study focuses on place attachment. Especially, the effect of public works on building of place attachment was empirically investigated.

## 2 Effects

### 2.1 Previous studies

Hagihara & Fujii [3] focused on degree of encounters with neighbors and environments, and its difference by the usage of transportation mode. They hypothesized that travel behavior, especially car use, affects the degree of encounters with environment and neighbors, and place attachment. Their result showed the possibility of negative impact of car use to encounters with social and environmental climate. Although they also hypothesized that the degree of encounters with them affect to the degree of place attachment, they could not show it. They said that because building of place attachment takes a long time, it was difficult to explain by short term experiment.

### 2.2 Hypothesis of this study

To examine the view of Hagihara [3], I proposed hypothesis1.

*Hypothesis 1 When individuals encounters with environment and neighbors in their residential area increase, their place attachments to residential area are enhanced.*

While Hagihara [3] examined the effect of travel behavior on place attachment, I go on to consider about the effect of consumer behavior. Based on the concept of Hagihara [3], I proposed two hypotheses about consumer behavior and place attachment.

*In daily consumer behavior,*

*Hypothesis2 According to consumer behavior, encounters with environments and neighbors are different.*

*Hypothesis3 The more encounters with environments and neighbors individuals have, the higher their place attachment is.*

I implemented surveys for residents in Japanese local cities to examine hypotheses.

### 2.3 Definition of place attachment

Researches on place attachment have been in the various disciplines like a human geography, environmental psychology, and social psychology. There are also various definition and model of place attachment along each object. In this study, I follow the definition by Hagihara [3] that is ‘an affective bond or link between people and specific places’.

For the definition of the ‘place’ which people have attachment to, Hagihara [3] defined as ‘school district of elementary school or junior high school where resident live in’. Because this study also focuses on the role of place attachment as a determinant of region-supporting behavior, I use this definition of ‘place’.

## 3 The process of place attachment building



### 3.1 Method

In this study, I implemented a questionnaire survey to follow up to the survey conducted in 2004 by Hagihara [3] to collect panel data.

#### 3.1.1 Sampling and Data collection

Investigation areas are Hamamatsu city, Shizuoka pref. and Toyohashi city, Aichi pref. Questionnaire was sent and backed by mail. After data matching of two surveys, I got 117 samples in panel data. The response rate was 25.7% at first survey and 38.8% at second survey. Participants consisted of 51.3% men. Their average age was 57.2 years and average of resident years was 28.3 years (at 2<sup>nd</sup> survey).

#### 3.1.2 Measures

Questionnaire is consisted by contents about place attachment, encounter with environment and neighbors, stock of regional resources and Individual characteristic.

##### 1 Place attachment

To measure the place attachment, 13 questions shows in TABLE 1 were used in the survey questionnaire. These questions are made by Oya & Haga [4] and Hagihara [3]. Hagihara [3] classified them to three scales, Place attachment: emotion (PAE), Place attachment: sustenance desire (PAS), and Place attachment: preference (PAP). Their questions consisted of five-point Likert-type ranging from 'I don't think so' (1) to 'I think so' (5). Cronbach's  $\alpha$  of each scale was statistically sufficient level as shown in TABLE1.

##### 2 Encounters with environment and neighbors

To measure the degree of encounters with environment and neighbors, 5 questions shown in TABLE 1 were used. These are taken from Hagihara [3]. Their questions consisted of five-point Likert-type ranging from 'I seldom do so' (1) to 'I frequently do so' (5).

TABLE 1: Scales of place attachment and Encounters

Encounters with environment and neighbors ( $\alpha=.84$ )	
Each question asks 'In your travel behavior, you....'	
Hear insects and birds' singing	
Touch the outdoor air	
Greet neighborhoods	
Talk with neighborhoods	
Get a sniff of smell of nature, such as earth (soil) and flora.	
Place attachment: preference A ( $\alpha=.89$ )	
I think that the place is livable.	
I have the place which I love in the place.	
I feel good when I walk in the place.	
I prefer the ambiance and character of the place.	
I prefer the place.	
I feel relaxed in the place.	
Place attachment: Emotion AE ( $\alpha=.83$ )	
I think the place cherished (or important).	
I have an attachment to the place.	
I feel that I have my own place in the place.	
I feel the place is mine.	
I want to live in the place forever.	
Place attachment: sustenance desire A ( $\alpha=.91$ )	
There are things what I don't want to change.	
There are things what I would be sorry if I lose it.	

### 3 Amount of regional resources stock

To measure the amount of regional resources stock, 15 questions: "Are there (*Park, convenience store, supermarket, river and pond, shrine and temple, arable land, historical landscape, forest, tourist spot, family restaurant, arcade game, community centre, shopping centre, rail station, large shopping centre*) your place?" were used. Their questions consisted of three-point ranging, "nothing", "a little" and "multiple".

### 3.2 Analysis and Results

#### 3.2.1 Correlation analysis

I used correlation analysis to examine the relation between the change of encounters and change of place attachment, shown in TABLE 2. TABLE2 show that change of encounters and change of PAP were significantly positive correlated. But change of encounters and other two scale of place attachment (PAS, PAE) were not collated. PAP, PAS and PAE were significantly correlated with each other.

TABLE2: Coefficients of correlation

		Encounters	Place attachment		
			PAE	PAS	PAP
Encounters		-	-	-	-
Place attachment	Emotion (PAE)	r	.019	-	-
		p	.857	-	-
		n	94	-	-
	Sustenance desire (PAS)	r	.009	.304*	-
		p	.930	.001	-
		n	96	108	-
	Preference (PAP)	r	.179*	.507*	.234*
		p	.082	<.001	.015
		n	95	106	107

\*  $p < .100$

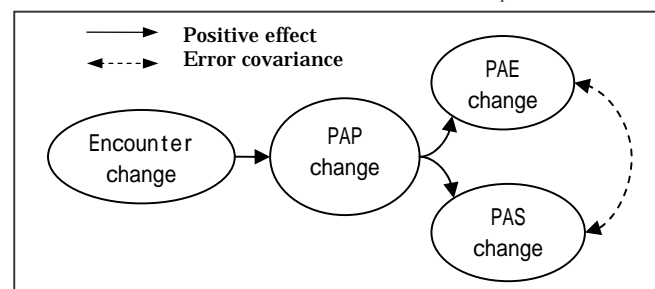


FIGURE 1: Estimated Structural Equation Model

TABLE 3 : Parameter Estimates from Structural Equation Modeling (B:standardized parameter)

		B	t-value
Encounter change	PAP change	0.12	2.02*
PAP change	PAE change	0.50	6.06**
PAP change	PAS change	0.42	2.55*
PAE change	PAS change	0.13	2.36*
NFI: 0.982 CFI:1.000 RMSEA:0.000 n=116			
		* $p < .100$ ** $p < .050$	

### 3.2.2 structural equation modeling

Following the correlations, I estimated a structure equation model shown in FIGURE 1. I presumed that it takes more time to build PAE and PAS than PAP, and there is unobserved common factors between PAE and PAS as shown by dot-arrow in FIGURE 1. The result shown in TABLE 3 indicates that all of estimates were statistically significant. This result support *ypothesis 1*.

### 3.2.3 actors which promote the place attachment building

The effect of encounter change on PAP that we empirically found may be dependent on regional attributes of the area. In order to investigate dependency on the regional attributes, dummy variables were created to denote attributes of the area. I used regression analysis to test interaction between encounters change and each dummy variable to test the dependency. As a result, only “multiple existences of shrine and temple” had significant positive effect on the PAP change. It was also shown that increase of encounter to environment and neighbors have significant effect on place attachment if there were some shrines and temples in the area, but such effect was not significant otherwise.

## 4 effects of consumer behavior on place attachment

### 4.1 method

In this study, I implemented questionnaire surveys to examine the effect of consumer behavior on place attachment to test Hypothesis.

#### 4.1.1 sampling and Data collection

Investigation areas were Takamatsu city, Kagawa pref., Toyohashi city, Aichi pref. and Kagoshima city, Kagoshima Pref. A questionnaire was sent by postal mail to those who were randomly selected from city directories. I requested a person who went for daily grocery shopping to answer. An answered questionnaire was also sent back by postal mail. I got 507 samples from 3 cities. The total response rate was 33.8%. Participants consisted of 83.2% women. Their average age was 51.0 years and average of resident years was 25.7 years.

#### 4.1.2 measures

Questionnaire was consisted of questions about place attachment, encounters with environment and neighbors

TABLE 4: Scales of Encounters with environment and neighbors during shopping

Communication during shopping C (α=.83)	
Greet neighborhoods	
Talk with neighborhoods	
Talk with store staffs	
Cognition and buying trend of local products C L (α=.70)	
I care about where products comes from	
I often buy local products.	

Note: Each question asks ‘In your shopping, you....’

during daily shopping, and consumer behavior.

### 1 place attachment

The same 13 questions as one used in 3.1.2(1) were also used as scales of place attachment.

### 2 Consumer behavior

The questionnaire includes questions asking about 10 daily-use shops, that is, shop name, shop size (small, large, extra large), shop type (shopping street, supermarket, convenience store, department store, others), shop location (urban area, suburb, near to station, near to home), transportation mode to shop (walk, bicycle, car, Train and Bus (PT).), and frequency to use the shop (times/week), average expenditure at the shop, attachment to the shop (four-point ranging) and amount of conversation with store staff (four-point ranging). I made two types of indicator for consumer behavior from responses of these questions that is, “modal share of each travel mode among all travel for shopping” and “shopping frequency at each shop type (times/week)”. I consider 8 categories as shop type as follows; 4 types (shopping street (SST), small supermarket(SSU), small [other] shop(SO), anything else(OT)) × 2 distances (near to home/ not near to home). Where [other] denotes shops except convenience store, shopping street, department store, and supermarket, anything else means shops except SST, SSU, SO.

### 3 Encounters with environment and neighbors during daily shopping

In this survey, I made 5 questions to measure encounters with environment and neighbors during daily shopping. After principle component analysis, they were separated into 2 components, i.e. “personal communication during shopping” and “cognition and buying behavior of local products” shown in TABLE4. There were some pertinent questions at encounters with environment and neighbors in question item of consumer behavior, like distance from the shop. So, these are not only question to show the degree of encounter. Their questions consisted of five-point Likert-type ranging from ‘I seldom do so’ (1) to ‘I frequently do so’ (5). Cronbach’s α of each scale was statistically sufficient level as also shown in TABLE4.

## 4.2 Analysis and Results

### 4.2.1 structural equation modeling

Following the concept by Hagihara [3], I presumed that consumer behavior has effect on encounters and place attachment. Based on this assumption, I estimate a structural equations model as shown in FIGURE2.

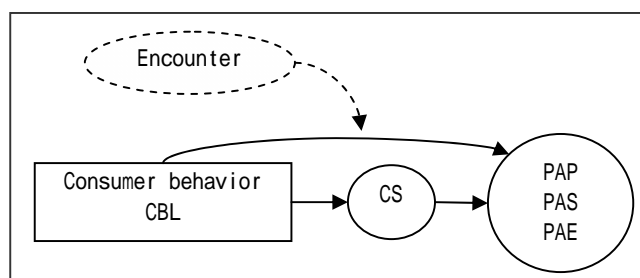


FIGURE 2: Estimated causal relation

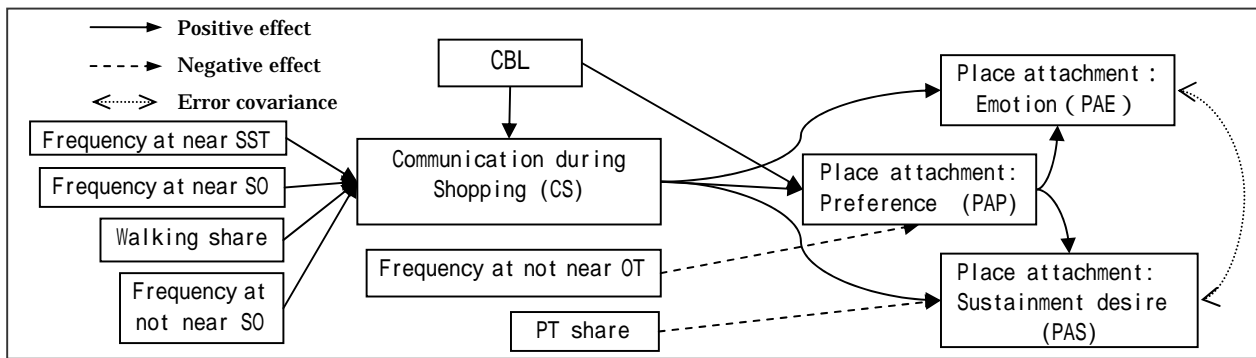


FIGURE 3: Estimated model of consumer behavior and place attachment

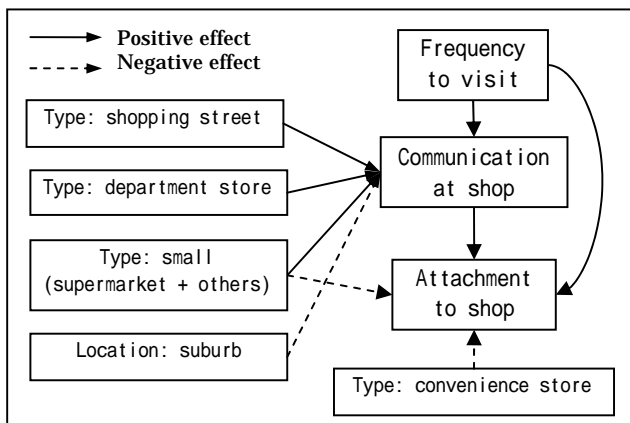


FIGURE 4: Estimated model of attachment to shop

As shown in this figure, I consider CBL as an Index of consumer behavior. In the result, relations which were statistically significant were shown in FIGURE 3. FIGURE 3 show that all of 3 variables of place attachment are positively affected by CS. This suggest that the more communication during shopping people have, the more place attachment toward residential place they have. FIGURE 3 also show; the more people go to shopping street or small shops near to home, the more shopping communication they have. These results support the *ypothesis 2* and *ypothesis 3*.

#### 4.2.2 Relation between place attachment and attachment to shops

CS used in the analysis shown in TABLE 4 was not limited to CS inside their residential place. But one may presume that only CS inside their residential place has direct effect on place attachment. For test this presumption, I calculated correlations of them, in both the case of shops near home ( $n=1266$ ) and shops not-near home ( $n=1296$ ). The result indicates that attachment to the shops near home had higher correlation with place attachment (PAP) ( $r=.207$ ) than attachment to the shops not-near home had ( $r=.096$ ).

#### 4.2.3 factors which promote the attachment to the shops

The analysis reported in 4.2.2 implies that factors of attachment to regional shops in an area would be important determinants of place attachment to the area. With this recognition, I tried to understand factors of attachment to

regional shops as an approach to understand place attachment to an area. I presumed that shop type (dummy variable denoting shopping street, convenience store, department store, small size supermarket and others and extra large supermarket and others), location of shop (dummy variance indicating urban area, suburb, near a station and near home) and frequency of visit to shop have effect on communication at shop and attachment to shop, communication at shop has also positive effect on attachment to shop. Structural equations model was again used for investigating structure of relations among these variables. The result indicates paths shown in FIGURE 4 were significant. As can be seen in FIGURE 4, communications at shop were relatively high in small supermarket and others, shopping street and department store and relatively low in shops located at suburb. It was also shown that the more communication individual had in a shop, the more attachment to the shop he/she has.

## 5 Conclusions

This study examined the hypotheses about process of place attachment building (*ypothesis1*) and that the consumer behavior affects the place attachment which was mediated by the encounters with the environment and neighbors (*ypothesis2,3*). To examine these hypotheses, two surveys for residents were implemented. The results imply that it takes a long time for place attachment to be developed and consumer behavior had influences on encounters and place attachment, as hypothesized in this study.

## References

- [1] Hidalgo, M. & Hernandez, B.: Place attachment: conceptual and empirical questions, *Journal of Environmental Psychology* 21, pp.273-281, 2001.
- [2] Brown, G., Brown, B. & Perkins, D.: New housing as neighborhood revitalization –place attachment and confidence among residents-, *Environmental and behavior*, vol.36 No.6, pp.749-775, 2004.
- [3] Hagihara, G & Fujii, S.: The psychological effects of car use on place attachment, the *Proceeding of infrastructure planning*, vol.33, 285, 2005 (in Japanese).
- [4] OYA, H. & HAGA, S.: The effect of preferred daily mode of transportation on elderly residents' feelings towards their neighborhood, *Rikkyo Psychological Research*, Vol. 45, pp.1-9, 2003 (in Japanese).

## A procedure of determining parameters by adapting to the results calculated by MEAM'92

Student Number: 05M18099 Name: Kento Tokumaru Supervisor: Kunio Takahashi

MEAM'92 の計算結果に適合させた  
二量体参照修正埋め込み原子法のパラメータ決定法

得丸 建人

本論では, MEAM'92 で使用されているスクリーニング関数の不連続性が起きる原因を明らかにしている. そこで, スクリーニング関数をはずして計算できる, 参照構造を二量体とした二量体埋め込み原子法(Dimer Reference Modified Embedded Atom Method; DR-MEAM)のパラメータ決定手法を提案している. その決定手法は, スクリーニング関数の影響が及ばない範囲で MEAM'92 の計算結果に DR-MEAM パラメータを適合させるものである.

### 1. Introduction

It is hoped that Modified Embedded Atom Method (MEAM) will be applicable for engineering field, because MEAM can calculate efficiently for large scaled simulation with including physical implication to some extent. Recently, the applicability is getting to expand to non-bulk systems, such as surface, cluster, however there are some issues. At first, the parameters have not been determined for many elements consistently since MEAM'92 that is the base of MEAM series, and arbitrary property is included during parameterization. These causes are attributed to that it has a difficulty to fill up reliable physical properties. Regarding arbitrary property, Yuan has solved to some degree by utilizing physical property of non-bulk systems. Secondly, "screening function" that has been introduced since MEAM'92 is considered to have discontinuity.

We demonstrate the application of particular cluster structure by MEAM'92, and clarify how the screening function has influenced on the discontinuity. Furthermore, we propose the

method of determining parameter with uniformity for many elements to expand the applicability of MEAM to non-bulk systems.

### 2. Screening function

Screening function has been introduced for simplification of calculation. Screening factor is determined geometrically. We assume the circumstance in Fig.2.1 to discuss discontinuity of the screening function. In case that the atom  $j$  moves towards atom  $i$ , screening factor  $S_{ijk}=0$ . Adversely, in case that the atom  $j$  moves away outside, screening factor  $S_{ijk}=1$ .

We investigate the influence of the screening factor geometrically by calculating cluster, as shown in Fig2.2. The 7 atoms at first layer are fixed. The 3 atoms at second layer are rotated, and fixed relative atomic position, and released only in the  $z$  direction. The discontinuity of the screening factor appears at the angle  $12^\circ$  to  $13^\circ$  as shown in Fig. 2.3. Then it is obvious that the relationship of distance between  $d_{12}$  and  $d_{28}$  changes suddenly, as shown in Fig2.4.

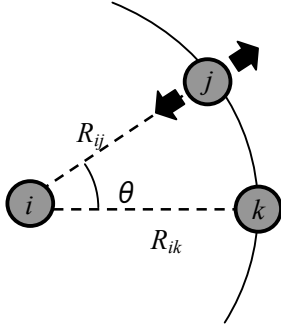


**Fig.2.1** Schematic in an example case of discontinuity

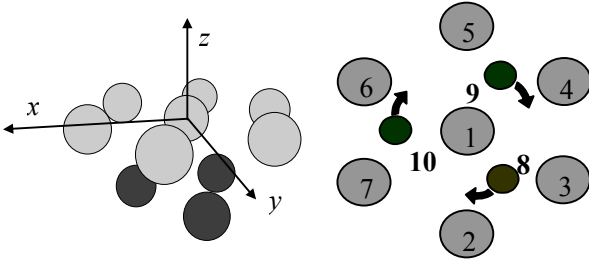


**Fig.2.2** Atomic position to demonstrate

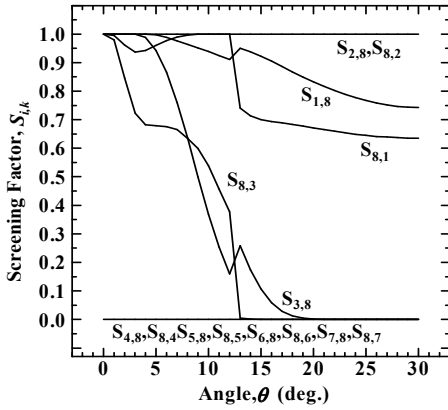


**Fig.2.3** Change of screening factor by rotating

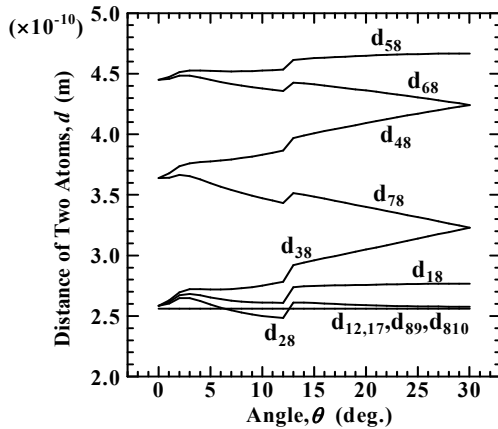


**Fig.2.4** Change of atomic distance by rotating

### 3. Theory of Dimer Reference Modified Embedded Atom Method (DR-MEAM)

Total energy is defined as followings in the MEAM theory.

$$E_{total} = \sum_i E_i \quad (1)$$

$$E_i = F_i(\bar{\rho}_i) + \frac{1}{2} \sum_{j(\neq i)} \phi_{ij}(R_{ij}) \quad (2)$$

where  $E_i$  is the energy of atom  $i$ ,  $F_i$  is the embedding function,  $R_{ij}$  is the distance between atoms  $i$  and  $j$ , and  $\phi_{ij}$  expresses the pair interaction between atoms  $i$  and  $j$ .

In former MEAM versions, in order to determine the pair interaction for type- $i$  atoms, a reference structure is used. The reference structure is usually selected as equilibrium crystal structure of type- $i$  atoms. By introducing cutoff or screening functions, the calculation of the pair interactions can be limited to the nearest neighbor atoms only. On the other hand, discontinuity of screening function exists, as described previously. In this work, we apply diatomic structure as a reference structure. Therefore, It needs not to introduce the cutoff or screening function.

The interaction term can be obtained from a universal energy function proposed by Rose *et al.* as the following.

$$E_i^u(R) = F_i(\bar{\rho}_i^0(R)) + \frac{1}{2} \phi_{ij}(R) \quad (3)$$

and then

$$\phi_{ij}(R) = 2E_i^u(R) - 2F_i(\bar{\rho}_i^0(R)) \quad (4)$$

where  $\bar{\rho}_i^0$  is the background ground electron density of dimer with distance of  $R$ .  $E_i^u$  is the energy per atom for the dimer reference structure as a function of the distance  $R$ , given by a universal energy function.

#### 4. Determination of DR-MEAM parameters

There are 13 parameters in DR-MEAM,  $Z_0$ ,  $E_0$ ,  $R_0$ ,  $\alpha_i$ ,  $A_i$ ,  $\beta_i^{(0)\sim(3)}$ ,  $t_i^{(0)\sim(3)}$ . Among those parameters,  $Z_0$  is the number of nearest neighbors at the dimer (=1).  $E_0$ ,  $R_0$ , and  $\alpha_i$  can be obtained from the properties of the diatomic molecule.  $t_i^{(0)}$  is a unit, just as MEAM'92.

The rests of 8 parameters,  $A_i$ ,  $\beta_i^{(0)\sim(3)}$ ,  $t_i^{(1)\sim(3)}$  are determined by utilizing some results calculated by MEAM'92.  $A_i$  is scaling factor for the embedding energy, and  $\beta_i^{(0)\sim(3)}$  are exponential decay factors for atomic densities, and  $t_i^{(1)\sim(3)}$  are weighting factors for the partial electron densities. Each optimized parameter is sought by fitting to minimum binding energy and equilibrium distance calculated by MEAM'92. Table.1 shows each atomic structure utilized in this work. We assume that the atomic position of the clusters, where the discontinuity of the screening function does not occur, is reliable.

Objective function is defined as,

$$F_{obj}\{A_i, \beta_i^{(0)\sim(3)}, t_i^{(1)\sim(3)}\} \\ = a_1 \left( \frac{E_{eq,DR} - E_{eq,92}}{E_{eq,92}} \right)^2_{tri.} + a_1 \left( \frac{R_{eq,DR} - R_{eq,92}}{R_{eq,92}} \right)^2_{tri.}$$

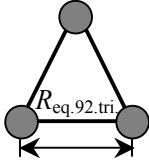
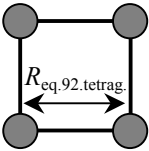
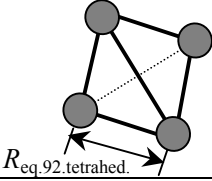
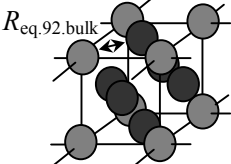
$$+ a_1 \left( \frac{E_{eq,DR} - E_{eq,92}}{E_{eq,92}} \right)^2_{tetrag.} + a_1 \left( \frac{R_{eq,DR} - R_{eq,92}}{R_{eq,92}} \right)^2_{tetrag.} \\ + a_1 \left( \frac{E_{eq,DR} - E_{eq,92}}{E_{eq,92}} \right)^2_{tetrahed.} + a_1 \left( \frac{R_{eq,DR} - R_{eq,92}}{R_{eq,92}} \right)^2_{tetrahed.} \\ + a_2 \left( \frac{E_{eq,DR} - E_{eq,92}}{E_{eq,92}} \right)^2_{bulk} + a_2 \left( \frac{R_{eq,DR} - R_{eq,92}}{R_{eq,92}} \right)^2_{bulk} \\ \rightarrow \min \quad (5)$$

where  $E_{eq,92}$  and  $R_{eq,92}$  stand respectively for minimum binding energy and equilibrium distance calculated by MEAM'92.  $E_{eq,DR}$  and  $R_{eq,DR}$  stand for the same results calculated by DR-MEAM. Additionally,  $a_1$  and  $a_2$  are weighting factors of clusters and bulk respectively. In order to maintain reliability in bulk, the value of  $a_2$  needs to be higher than that of  $a_1$ . The value of  $a_1$  is 1, the value of  $a_2$  is 4 in this work.

#### 5. Results and Discussion

Optimized parameters are listed in Table2, and the values are the most minimal in Eq. (5). It cannot be helped that there are some other candidates, because some of them could be locally minimal. However there is high possibility that the optimized parameter exists in the candidates. If the procedure in the same manner is implemented for other elements, the values of parameters can be determined for the same number of elements as MEAM'92.

**Table.1.** Figure of each regular atomic structure used for optimization of DR-MEAM parameters, and the values of equilibrium distance  $R_{eq,92}$  (Å) and binding energy  $E_{eq,92}$  (eV) calculated by MEAM92.

Regular Atomic Structure	Triangle	Tetragon	Tetrahedron	Bulk
				
$R_{eq,92}$ (Å)	2.55	2.39	2.64	2.56
$E_{eq,92}$ (eV)	5.45	8.01	7.19	3.54

Uncertainties of non-bulk systems, such as the surface properties, are one of the main reasons of the present study for a re-determination of MEAM parameters. We investigated the applicability of the DR-MEAM to the surface energies using optimized Cu parameters. The Cu surface energies of the three low-index surfaces, (100), (110), and (111), compared with the experimental results and the results calculated by 2NN-MEAM, are listed in Table 3. The surface energies calculated by this work are lower than experimental data. The results in this work indicate as valid values as those of 2NN-MEAM, considering the experimental results are extrapolated from adjacent melting point. DR-MEAM has possibility to provide a

good solution for surface properties, and other non-bulk systems.

## 6. Conclusion

A determination method of the DR-MEAM parameter values is proposed. The method utilizes minimum binding energy and equilibrium distance calculated by MEAM'92. The method can determine the parameter values for many elements consistently as MEAM'92. The surface properties of low-index surface energies calculated by using the optimized DR-MEAM parameters indicate reasonable results just as 2NN-MEAM. The DR-MEAM has the possibility to expand its applicability to non-bulk systems.

**Table 2.** One of the optimized parameters for the DR-MEAM.

	$E_i^0$	$R_i^0$	$\alpha_i$	$A_i$	$\beta_i^{(0)}$	$\beta_i^{(1)}$	$\beta_i^{(2)}$	$\beta_i^{(3)}$	$t_i^{(0)}$	$t_i^{(1)}$	$t_i^{(2)}$	$t_i^{(3)}$
Cu	1.01	2.22	4.42	0.64	4.77	4.35	5.25	5.25	1	1.09	1.09	1.11

**Table 3.** Comparison of surface properties by calculation methods. The parameters calculated by DR-MEAM are optimized values by this work, as shown in Table2.

Method	Surface Energy, $E_{\text{surf}}$ (mJ/m <sup>2</sup> )		
Experiment <sup>[Ref.1]</sup>	1770		
	$E_{(100)}$	$E_{(110)}$	$E_{(111)}$
2NN-MEAM <sup>[Ref.7]</sup>	1382	1451	1185
DR-MEAM	1404	1489	1341

## References

1. W.R. Tyson and W.A. Miller, *Surf. Sci.* 62, 267(1977)
2. M. I. Baskes, *Phys. Rev.* B46, 2727(1992)
3. M. I. Baskes, J. E. Angelo and C. L. Bisson, *Modeling Simul. Mater. Sci. Eng.* 2, 505 (1994)
4. M. I. Baskes, *Mater. Chemist. and Phys.* 50,152(1997)
5. T. Yamagishi, K. Takahashi, and T. Onzawa, *Surf.Sci.* 445, 18(2000)
6. X. Yuan, K. Takahashi, Y. Yin, and T. Onzawa, *Modelling, Simul. Mater. Sci. Eng.* 11(2003)
7. B. Lee, J. Shim, and M. I. Baskes, *Phys. Rev*, B68.144112 (2003)

# LONG TERM PREDICTION OF STRENGTH DETERIORATION DUE TO CA LEACHING FROM CEMENT-TREATED SOIL

Student Number: 05M18113 Name: Katsufumi Hashimoto Supervisor: Nobuaki Otsuki

## セメント系改良地盤からの Ca 溶脱に伴う強度低下に関する長期予測

橋本 勝文

本論文では、(1)粘土種類及び周辺環境中の  $\text{Cl}^-$  及び  $\text{H}^+$  が Ca 溶脱に及ぼす影響を定量的に把握すること、(2)(1)の結果を用いて、改良地盤からの Ca 溶脱に伴う化学的及び物理的変質に関する数値解析的長期予測手法を構築し、その妥当性を検証すること、(3)(2)で構築した長期予測手法を用いて、セメント系改良地盤の Ca 溶脱による化学的及び物理的変質に関する耐久性予測を行い、長期に亘る改良地盤の部材レベルにおける耐久性評価を目的とした。

### 1 Introduction

Cement-treated soil is a composite material whose strength and durability is improved by mixing soil with cement as a hardening agent. Cement-treated soil constructed by Deep Mixing Method is considered as highly durable material. However, previous researches indicate that there is a high possibility of strength deterioration occurring in cement-treated soil due to long term Ca leaching from Ca hydrates [1]. A characteristic of cement-treated soil is that soil particle itself has the pozzolanic reactivity, comparing with other cementitious materials, such as mortar or concrete. However, the influence of pozzolanic reactivity of soil on the deterioration due to Ca leaching is still not clear. Additionally as cement-treated soil is constructed by adding the hardening agent into the soft ground at the site, the surrounding environment is soft ground containing  $\text{Cl}^-$  and  $\text{H}^+$ . However, the influence of  $\text{Cl}^-$  and  $\text{H}^+$  in surrounding environment on the deterioration due to Ca leaching is also still not clear. The above influence on Ca leaching from cement-treated soil is not considered in the long term prediction method using numerical analysis in previous studies [2]. In addition, from the economic of view, prediction result of the deterioration due to Ca leaching should be considered during the design stage in order to reduce unnecessary cost of construction such as amount of cement or member size. From the above background, the objectives of this paper are set as follows. Objective 1 is to investigate on the influences of pozzolanic reactivity of soil,  $\text{Cl}^-$  and  $\text{H}^+$  in surrounding environment on the deterioration due to Ca leaching quantitatively. Objective 2 is to propose and confirm the validity of the long term prediction method considering the above influences. Objective 3 is to evaluate the long term

durability of cement-treated soil against Ca leaching by using the above method.

### 2 Outline of Experiment

In this section, outline of experiment is summarized as follows. Especially, experimental cases, outline of specimen and measurement items are described respectively.

#### 2.1 Experimental cases

Experimental cases based on objective (1) are summarized in **Table-1**. Experimental cases based on objective (2) are summarized in **Table-2**. The types of soil used in this paper are Daikoku, Tokuyama, Kawasaki, Ariake, Kaolin soil. The types of cement used in this paper are ordinary portland cement (OPC), low heat portland cement (LPC) and blast furnace slag cement (BFSC).

**Table-1** Experimental cases (1)

Soil type	w (%)	Ca(OH) <sub>2</sub> content (kg/m <sup>3</sup> )
Daikoku	100	30, 60, 90
Tokuyama		
Kawasaki		
Ariake		

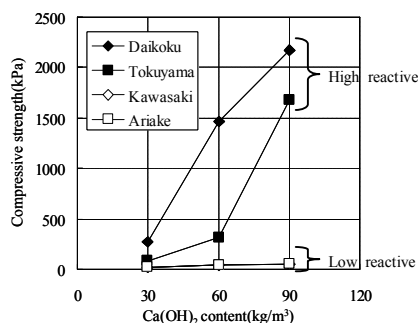
**Table-2** Experimental cases (2)

Soil type	Cement type	w (%)	Cement content (kg/m <sup>3</sup> )
Daikoku	OPC	87	42
			84
			125
	BFSC		84
Tokuyama	OPC	132	42
			84
			125
	BFSC		84
Kawasaki	OPC	110	42
			84
			125
	BFSC		84
Ariake	OPC	100	42
			84
			125
	BFSC		84



**Table-3** The amount of dissolvable silica and amorphous material in soil

	Daikoku	Tokuyama	Kawaskai	Ariake
Amorphous minerals ( )	17.9	17.4	9.8	8.5
Dissolvable silica ( )	7.5	9.4	3.8	4.2

**Fig-1** The relationship between soil type and compressive strength

## 2. 2 Outline of specimen

The specimens are cured for 24 hours under sealed condition with room temperature of 20°C. The specimens are exposed to the soil or solution for 24 hours after casting.

## 2.3 Measurement items

### a) Initial porosity

The initial porosity is measured and calculated after each curing period. The initial porosity is calculated from mass in condition of submerged, oven dried and saturated surface dried.

### b) Initial content of Ca(OH)<sub>2</sub>

The initial content of Ca(OH)<sub>2</sub> is measured by differential thermal analysis after each curing period. Raising rate of temperature is [40°C/min] and platinum cell is used in N<sub>2</sub> gas from 40°C to 1000°C.

### c) Initial compressive strength

Initial compressive strength is measured by compression testing machine. Rate of loading is 3[mm/min].

### d) Ca leaching ratio

Concentration of Ca in outer solution is measured using ion chromatography, and Ca leaching ratio was calculated. Outer solution is exchanged every 7 days for 26-week exposure.

### e) Ca content

Ca content is measured using energy-dispersible X-rays as the parameter of chemical deterioration after 13 and 26-week exposure.

### f) Ca/Si mole ratio

Ca/Si mole ratio of cement matrix is measured using energy-dispersible X-rays as the parameter of chemical deterioration after 13 and 26-week

exposure.

### g) Estimated compressive strength

Estimated compressive strength is measured using needle penetration test and the relationship between compressive strength and the slope of needle penetration as the parameter of physical deterioration after 13 and 26-week exposure.

## 3 Influences of Soil Type, Cl<sup>-</sup> and H<sup>+</sup> on Deterioration Due to Ca Leaching

In this section, specimens are exposed to soil and solution respectively to investigate the influences of soil type, Cl<sup>-</sup> and H<sup>+</sup> on deterioration due to Ca leaching.

### 3.1 Influences of the amount of dissolvable silica and amorphous material in soil on the pozzolanic reactivity

The amount of dissolvable silica and amorphous material in soil is shown in **Table-3**. The relationship between soil type and compressive strength is shown in **Fig-1**. From this figure, it is confirmed that the larger amount of dissolvable silica and amorphous material in soil, the higher pozzolanic reactivity of soil. Therefore, it can be said that Daikoku and Tokuyama soil is high reactive soil, Kawasaki and Ariake soil is low reactive soil in this paper. The relationship between distance from exposure surface and compressive strength after 26-week exposure is shown in **Fig-2**. From this figure, the inside strength after deterioration due to Ca leaching is the highest in case of using LPC. The relationship between exposure period and the deterioration depth after 26-week exposure is shown in **Fig-3**. The relationship between exposure period and the decreasing ratio of compressive strength at 5mm from exposure surface after 26-week is shown in **Fig-4**. From these figures, in the case of using higher reactive soil, it is confirmed that the deterioration more depthless. On the other hand, in the case of using higher reactive soil, it is confirmed that the decreasing ratio of compressive strength at 5mm from exposure surface is larger.

### 3.2 Influences of Cl<sup>-</sup> and H<sup>+</sup> on Ca leaching

The relationship between distance from exposure surface and compressive strength after 26-week exposure to NaCl and H<sub>2</sub>SO<sub>4</sub> solution is shown in **Fig-5**. From these figures, the higher the concentration of Cl<sup>-</sup> and H<sup>+</sup> in outer environment, the faster the progress of deterioration due to Ca leaching. In addition, it is confirmed that crack occurs at the exposure surface in case of exposing to H<sub>2</sub>SO<sub>4</sub> of pH3-4.

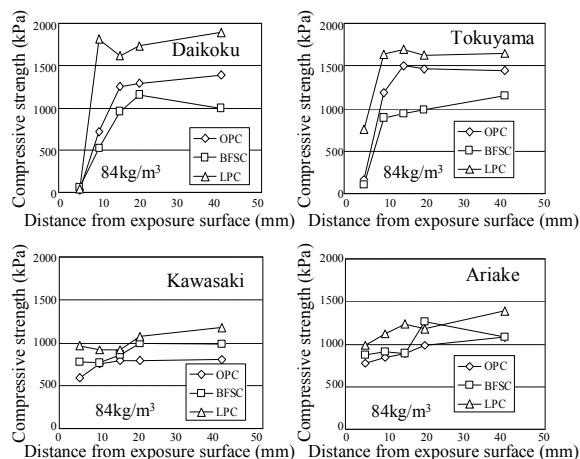


**Fig-2** The relationship between distance form exposure surface and compressive strength

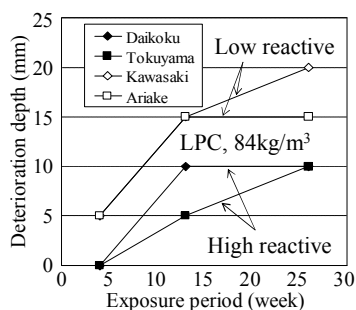


**Fig-3** The relationship between exposure period and deterioration depth

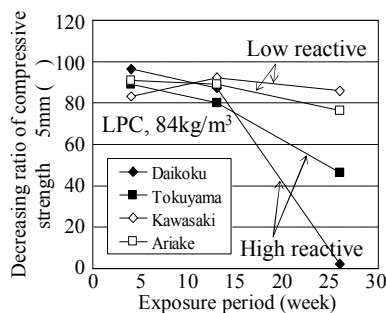


**Fig-4** The relationship between exposure period and decreasing ratio at 5mm from exposure surface

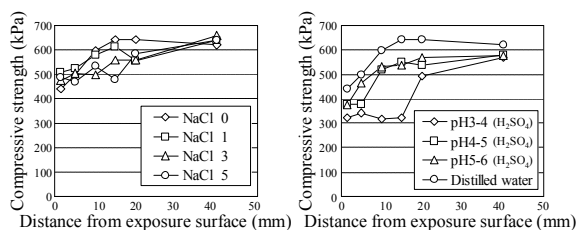
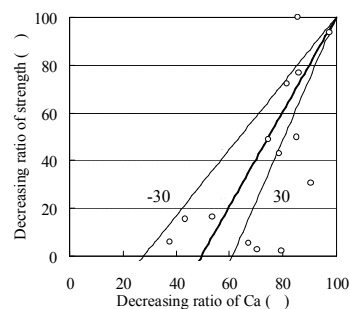


**Fig-5** The relationship between distance form exposure surface and compressive strength after 26-week exposure to NaCl and H<sub>2</sub>SO<sub>4</sub> solution

## 4 Proposal of Numerical Prediction Method for Ca Leaching



a: trend line passing through point (100 ,100 )

b: line whose slope is 30 of a

c: line whose slope is -30 of a

**Fig-6** Strength deterioration model

In this section, numerical prediction method for Ca leaching is proposed. In addition, the validity of the method is confirmed by comparing to the result of field investigation.

### 4.1 Models for numerical prediction method

#### a) Ion migration model

Ion migration model, which is proposed in previous study, Nernst-Planck equation considering Debye-Hückel theory and electrical neutrality condition, is used.

#### b) Ca adsorption model

Ca adsorption model, which is based on Freundlich adsorption equation, is used.

#### c) Ca dissolution model

Ca dissolution model of Ca(OH)<sub>2</sub> and C-S-H obtained from solubility test is used to consider the influence of Cl<sup>-</sup> and H<sup>+</sup>.

#### d) Fixation model of chloride ion

Fixation model of chloride ion considering Ca leaching, which is based on fixation model of chloride ion proposed in previous study [3], is used.

#### e) Deposition and dissolution model of CaSO<sub>4</sub>

Deposition and dissolution model of CaSO<sub>4</sub>, which considers the increase and decrease of pore volume, is used.

#### f) Deposition and dissolution model of CaCO<sub>3</sub>

Deposition and dissolution model of CaCO<sub>3</sub>, which considers the increase and decrease of pore volume, is used.

#### g) Strength deterioration model

Strength deterioration model, which is based on the relationship between the decrease of Ca content and that of strength obtained from exposure test, is used as shown in Fig-6.

### 4.2 Confirmation of the validity of numerical prediction method

The result of field investigation of cement-treated soil, which is in Daikoku pier, after 20years of service life is used to confirm the validity of

numerical prediction method proposed in this paper [4]. The investigation result and prediction result are shown in **Fig-7**. From this figure, it is confirmed that the prediction result shows a good agreement with the field investigation result.

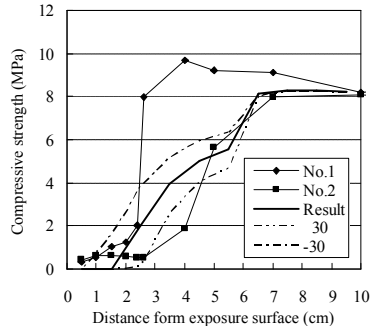


**Fig-7** The investigation result and prediction result

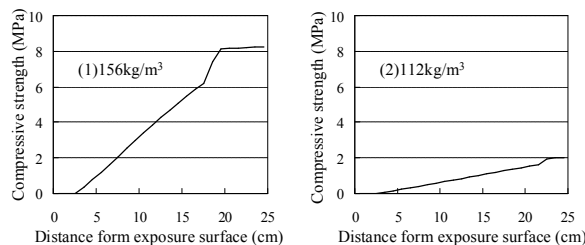
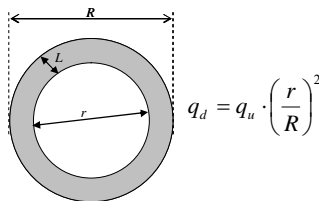


**Fig-8** The prediction results of case (1) and (2)



$q_d$ : Apparent compressive strength after deterioration

$q_u$ : Compressive strength before deterioration

$L$ : deteriorated depth

**Fig-9** Outline of deteriorated columnar cement-treated soil

## 5 Long Term Prediction of Durability of Cement-Treated Soil against Ca Leaching

In this section, durability against Ca leaching is predicted for cement-treated soil at Daikoku pier in service life for 100 years. As mentioned before, from the economic of view, prediction result of the deterioration due to Ca leaching should be considered during the design stage in order to reduce unnecessary cost of construction such as amount of cement or member size. On the other hand, there is a possibility that the deterioration due to Ca leaching can not be ignored in case of using less amount of cement or member size. Actually cement content of 156[kg/m<sup>3</sup>] is used at Daikoku pier, and it is confirmed that the strength in sound area (8.2[MPa]) is too higher than the design strength (2[MPa]) from the result of field

investigation after 20years of service life. Therefore, the durability against Ca leaching of columnar cement-treated soil for 100years is investigated by the numerical prediction method from the following view points. (1)In case of using the same cement content as cement-treated soil at Daikoku pier (156[kg/m<sup>3</sup>]). (2)In case of using the minimum cement content to fulfill the design strength (112[kg/m<sup>3</sup>]). The prediction results of case (1) and (2) are shown in **Fig-8**. From these figures, it is confirmed that the depth where the strength is less than 2[MPa] is 10[cm] in case (1) and 23[cm] in case (2). In addition, the apparent strength is 3.15[MPa] (>2. 0[MPa]) in case (1) and 0.58 [MPa] (<2[MPa]) in case (2) after 100years if it is presumed that the strength in deteriorated area is 0 (**Fig-9**). Therefore, when cement-treated soil is constructed, it is confirmed that it is necessary to use amount of cement content considering both design strength and deterioration due to Ca leaching.

## 6 Conclusions

As the results of this paper, the following conclusions are obtained. (1)The influences of pozzolanic reactivity of soil, Cl<sup>-</sup> and H<sup>+</sup> in surrounding environment on the deterioration due to Ca leaching are clarified. (2)The numerical prediction method for the deterioration due to Ca leaching is proposed and the validity is confirmed. (3)It is confirmed that it is necessary to set the amount of cement content considering deterioration due to Ca leaching as well as design strength when cement-treated soil is constructed.

## 7 References

- [1]Masaaki Terashi, Hiroyuki Tanaka, Tsukasa Mitsumoto, Sadakichi Honma, Terumi Ohashi, The Report of Port and Airport Research Institute, ol.22, No.1, pp.69-95, 1983.
- [2]Takahiro Nishida, Nobuaki Otsuki, Masakazu Ikeda, CHAMPAPHANH Bouavieng, Masaaki Terashi, Proceedings of JSCE, Journal of Construction Management and Engineering, No.784, I-66, pp.205-206, 2005.
- [3]Tsuyoshi Maruya, Somnuk Tangtermsirikul, Yasunori Matsuoka, Simulation of chloride movement in hardened concrete Proceedings of JSCE, Concrete Engineering and Pavements, No.442, -16, pp81-90, 1992.
- [4]Masaki Ikegami, Ichiba Takehiro, Ohishi Kanta, Terashi Masaaki, Long-Term strength change of cement treated soil at Daikoku Pier, Proceedings of Soft Ground Engineering in Coastal Areas, pp.241-246, 2002.

# Analysis of turbulent organized structures at the urban outdoor scale model (COSMO)

Student Number: 05M18120 Name: Satoshi HIROOKA Supervisor: Manabu KANDA

## 屋外スケールモデル (COSMO) における 乱流組織構造の解析

廣岡 智

本論文の目的は屋外スケールモデル COSMO における乱流の観測を行い、乱流組織構造の存在を確認し、その定量的把握をすることである。具体的には水平方向に熱電対と風速計を大規模に配置し、乱流観測を行った。そして、乱流構造の定量的解析に向け、OSIM(Organized Structure Identification Method)と呼ぶ乱流構造の抽出手法を開発した。これは乱流変動の連続点を構造として認識し、そのスケール、形状等を明らかにする方法である。この新しい方法で、風速の増加に伴い、より細長く筋立った構造になること、水平方向に大きな構造は時間方向にも大きい構造であること、正の温度変動をもたらす構造は負の温度変動をもたらす構造より筋立った構造であることが分かった。

## 1. Introduction

Asian Mega-cities have been faced on overpopulation. Overpopulated cities have significant negative environmental effects on atmosphere, such as heat island phenomena and localized heavy rain. To overcome these problems, it is necessary to clarify the exchange process between the urban canopy and the atmosphere.

Up to the present, the existence of the turbulent organized structure (TOS, Fig1.1) on air flow is clarified by various field's observations and wind tunnel experiments. It is recognized that TOS account for major heat transport and thus is a key to solve the atmospheric environmental issues. In real cities, due to the social restriction, only a few vertical observations have been done. Using wind tunnel experiments, Adrian proposed the figure of TOS (Fig.1.1), over a flat wall [1], however, TOS over real cities are still unknown.

In order to break through these gaps, I construct the scale model city called COSMO (Comprehensive Outdoor Scale Model experiment for urban climate, Fig1.2).

At the COSMO, I conduct the turbulent observation by using the 70 thermocouples and 30 sonic anemometers, in order to detect the spatial distribution of TOS. Moreover, for the quantitative analysis, I develop a new analytical way called OSIM (Organized Structure Identification Method). I applied it to COSMO data to investigate the TOS.

## 2. Observation setup

### 2.1 Scale Model site

The size of the urban scale model is 50 x 100m

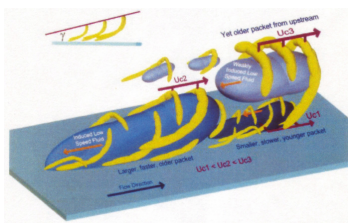


Fig1.1 TOS (by Adrian et al, 2000)



Fig1.2 COSMO

horizontal extent with 1.5m (=H) cubic roughness arranged uniformly(Fig2.1). The plan area index is 0.25.

### 2.2 Instruments

Instruments are set as shown in Fig.2.1. To observe the turbulent properties, 30 sonic anemometers (YOUNG model 81000) and 60 thermocouples are used. Sonic anemometers are arranged on upstream side and downstream side. All sonic anemometers' observation height are 3m (=2H) and horizontal resolution are 3m. 60 thermocouples are horizontally arranged on downstream side only. The observation height is 3m (2H) and horizontal resolution are 0.75m (0.5H).

### 2.3 Calculation

To detect the turbulent motion, I calculate the fluctuation of instantaneous wind velocity and temperature from their 1 minute averaged values. The data is only analyzed when the horizontal wind direction is less than 5 degree from the prevailing wind direction as shown on Fig.2.1.

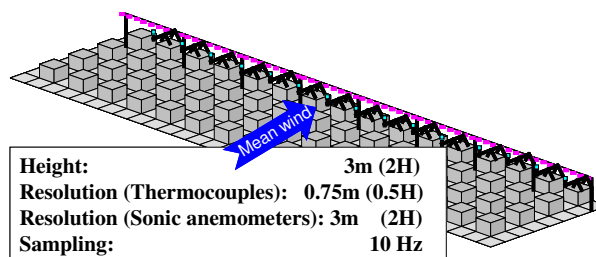
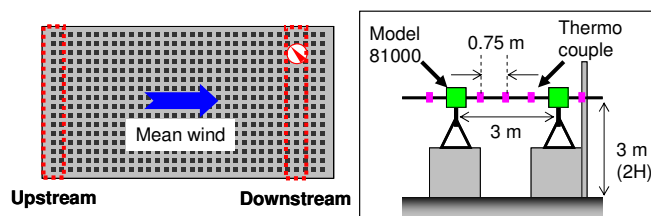


Fig2.1 Configuration of instruments

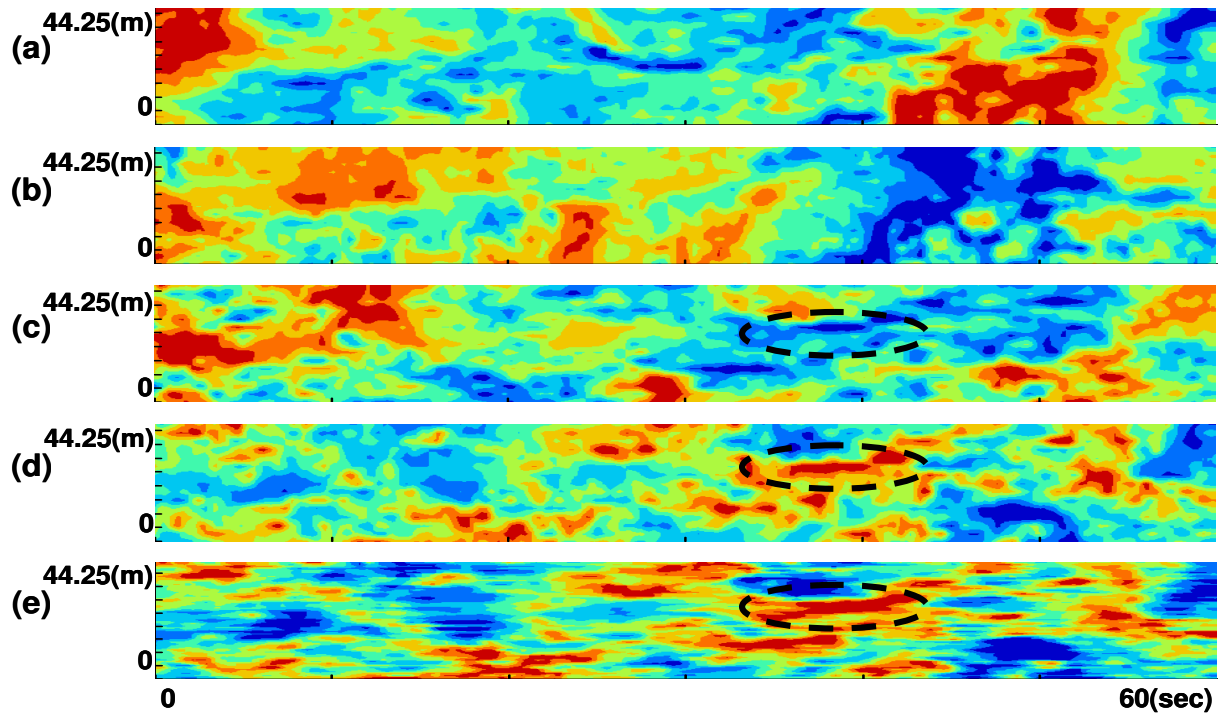


Fig 2.2 Horizontal distributions

((a): the fluctuation of stream wise velocity at upstream side, (b): the fluctuation of temperature at upstream side, (c): the fluctuation of stream wise velocity at downstream side, (d): the fluctuation of temperature at downstream side, (e): the fluctuation of temperature at downstream side by thermocouples)

## 2.4 Qualitative analysis

Fig. 2.2(a), (b), (c) and (d) show the horizontal distribution (vertical-axis) and time series (horizontal-axis) of the fluctuation of stream wise velocities on the upstream side, temperature on the upstream side, stream wise velocities on the downstream side and temperature on the downstream side by sonic anemometers, respectively. And Fig 2.2(e) is the horizontal distribution (vertical-axis) and time series (horizontal-axis) of the fluctuation of temperature by thermocouples.

In Fig.2.2 (c) and Fig.2.2 (d), the dotted circled area shows the area of relatively lower wind velocity (Fig.2.2(c)) and it corresponds to that of higher temperature (Fig.2.28 (d)). It is due to the coherent motion of low speed and high temperature air mass.

In Fig.2.2 (d) and Fig.2.2 (e), the horizontal temperature distribution by thermocouples and that by anemometers are well matched.

Hereby, I consider that horizontal distribution of temperature fluctuation by thermocouples at the downstream successfully captures TOS.

In Fig.2.2 (b) and Fig.2.2 (d). The difference between upstream observation data and downstream observation data are clearly differed. At the upstream, the higher temperature zone is relatively larger than its zone at downstream. If the turbulent organized structure is not produced by cubic roughness at COSMO, these figures must be same. Therefore, it is clear evidence that the downstream

For the quantitative analysis of temporal-spatial figure of TOS, OSIM has been developed. OSIM stands for Organized Structure Identification Method. OSIM detects the continuous grid points on time and space fields as Turbulent Organized Structure.

As the first step, the fluctuation of temperature is divided by standard deviations at each observation points (Dimensionless process). And I extract the grid points in which the temperature fluctuations are over the threshold (See 3.2). Secondly, these points are clustered if they are spatiotemporal continuous. As the final step, the cluster's characteristic values are output (See 3.3). Based on the outputs value, the results are statistically processed.

## 3.2 Threshold set up

### <Concept of Threshold>

I set threshold as a constant value. In addition, the threshold value ( $\alpha$ ) is set positive and negative ( $\pm\alpha$ ). Positive threshold value detect the low speed streaks (hereafter, I call it "the high temperature structure"), whereas, negative threshold value detect the sink of the cooler air (hereafter, I call it "the low temperature structure").

### <Sensitivity analyses of $\alpha$ >

It seems that based on the threshold value, the result of OSIM must be different, for example, the number of TOS or the size of TOS detected by  $\alpha$  might be different. In order to decide the appropriate  $\alpha$  value, I do two sensitivity analyses of  $\alpha$ . The first sensitivity analysis is focusing on the change of the number of TOS per 1min and the second sensitivity analysis is focusing on the change of temperature

## 3. New quantitative analysis (OSIM)

### 3.1 Algorithm of OSIM

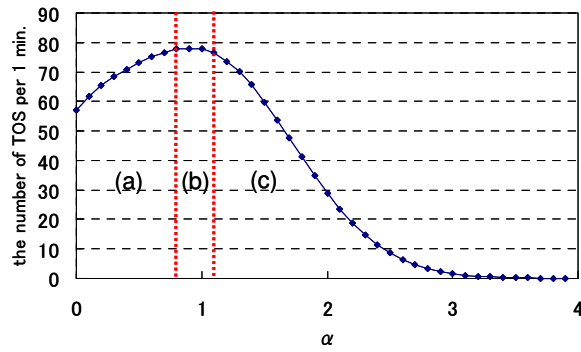


Fig3.1 the sensitivity analysis of  $\alpha$  in the number of TOS detected by  $\alpha$

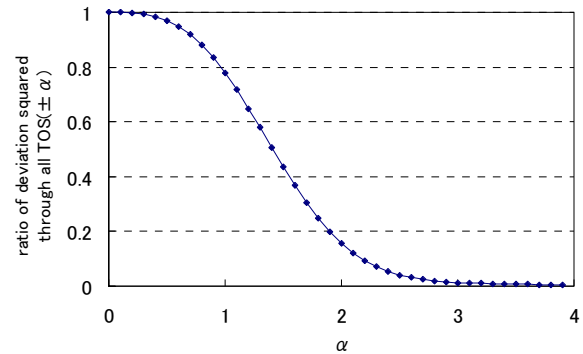


Fig3.2 the sensitivity analysis of  $\alpha$  in the total energy occupation by TOS detected by  $\alpha$

deviation squared through TOS detected by  $\pm\alpha$ .

Firstly, Fig 3.1 is the results of the first sensitivity analysis of  $\alpha$  in the number of TOS detected by  $\alpha$  through 81 hours. In Fig 3.1, horizontal axis is the range of  $\alpha$ , and vertical axis is the number of TOS per 1 min. Here, I'd like to divide this figure into three parts as shown. In zone (a), the number of TOS increases. This is due to the decoupling of TOS. And after reaching peaks ( $\alpha=0.8-1.1$ , in zone (b)), the number of TOS starts to decrease (in zone (c)). This is because too much strong threshold ignores some of TOS. I consider that  $\alpha$  should be set in peaks ( $\alpha=0.8-1.1$ ). In these regions, it seems that TOS is properly divided and not so many TOS are ignored.

As the second sensitivity analysis, I do the sensitivity analysis of  $\alpha$  in deviation squared through all TOS detected by  $\pm\alpha$ . Fig 3.2 shows the result of this sensitivity analysis. The horizontal axis is same of Fig 3.1 and the vertical axis shows the ratio of deviation squared through all TOS detected by  $\pm\alpha$  (shown Eq.1). This value means that the sum of TOS detected by  $\pm\alpha$  assume how much heat transportation. Here if  $\alpha$  is set as  $\pm 1.0$ , then, by all TOS detected by  $\pm\alpha$ , energetically about 80% of heat transportation are expressed. Hereby, I set 1.0 as a threshold and OSIM is operated.

### 3.3 Output values

For the determination of characteristic's TOS, I define

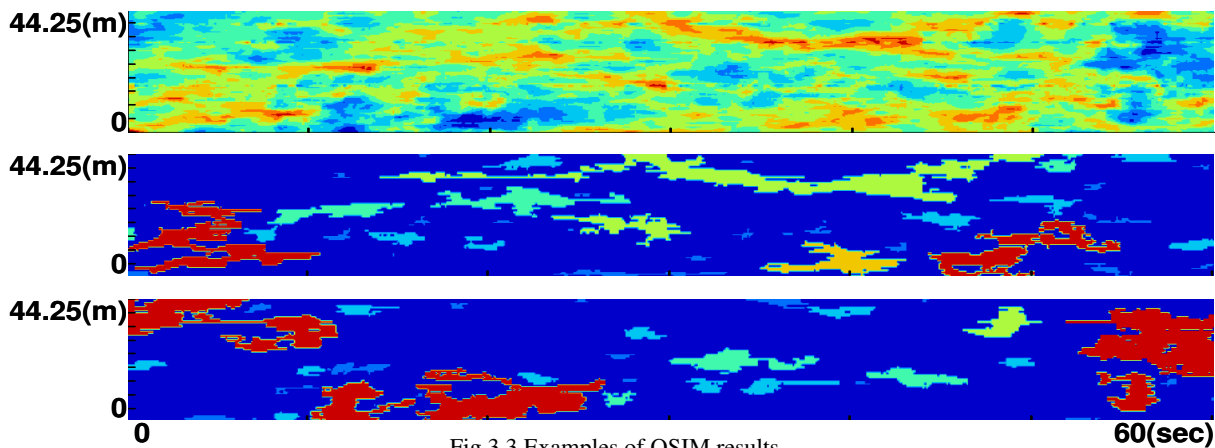


Fig 3.3 Examples of OSIM results  
(top: Raw data, middle: high temperature structures, bottom: low temperature structures based on mean span wise width, TOS are colored. )

(ratio of deviation squared through all TOS( $\pm\alpha$ ))

$$= \frac{\sum_{all\_TOS} (T')^2}{\sum_{all} (T')^2} \cdot \cdot \cdot \quad (Eq.1)$$

$all\_TOS$  : area occupied by TOS( $\pm\alpha$ )

$all$  : total area

some values as follows.

#### ID number

All clusters have their own unique No. for identification, called ID number.

#### Mean span wise width

This is the average of the difference between maximum value and minimum value of the span wise coordinate which a TOS has.

#### Mean time duration

This is the difference between maximum value and minimum value of the time coordinate which a TOS has.

#### Mean time scale length

This is the value multiplied mean time duration by mean wind velocity at downstream.

#### TOS area

This is the value multiplied mean time duration by mean span wise width.

#### Energy of TOS

This is the sum of temperature deviation squared through a TOS area.



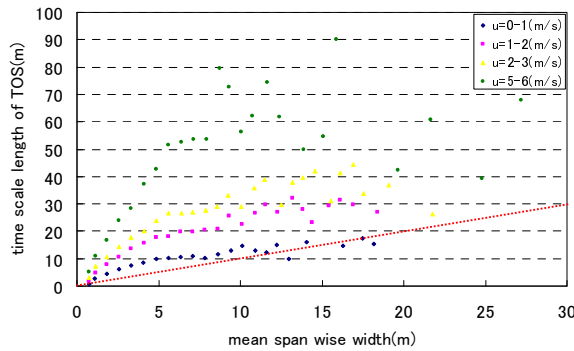


Fig4.1 mean span wise width and time scale length

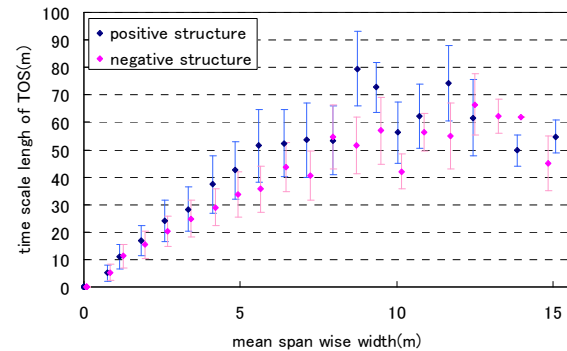


Fig4.2 high temperature structures and low temperature structures

### 3.4 Output example

Let me show two examples of OSIM results. Fig 3.3(a) shows the raw horizontal distribution data. And Fig 3.3(b) shows the result of mean span wise width of high temperature structures. Here, based on the mean span wise width, the TOS is colored. As Fig 3.3(c), the result of mean span wise width of low temperature structures is also colored.

## 4. Result and discussion

In order to understand the behavior of TOS with wind velocity changes, 51days observation data is analyzed by OSIM. Only  $\pm 5$  degree wind direction and unstable condition data is used. The data is categorized by mean wind velocities (from 0-1(m/sec) to 5-6(m/sec) every 1(m/sec)). And analysis follows these wind categories.

One of OSIM's accents is to analysis with keeping spatiotemporal information of TOS. So, all TOS is categorized by their mean span wise width. Each category is set every 0.75(m). Based on these span wise, the results are statistically processed. Here, results are shown.

First of all, in Fig.4.1, the statistics results on each span wise width categories are shown. Here, horizontal axis is the mean span wise width and vertical axis is the average value of the time scale length on each category. And the red line shows the aspect ratio equal to 1.0, then, the TOS figure is like a square. Four results are shown. In strong wind condition ( $u=5-6$ (m/s)), the dots are quite far from the red line. In contrast, in weak wind condition ( $u=0-1$ (m/s)), then dots are almost on the red line. This means, the strong wind tends to produce much slender TOS. Moreover, until the mean span wise width, 7m, the proportional relation is clear. With the mean span wise width increased, the time scale length of TOS also tends to become longer. Moreover, after reaching to the mean span wise width (7m), the time scale length has peaked. This means, there is the limitation of the time scale length of TOS.

Finally, the high temperature structure tends to have longer time scale length than the low temperature structure's time scale length. Fig.4.2 is the result analyzed by 5-6(m/sec) wind velocity data. The blue dots show the high temperature structure's relationship between mean span wise

and time scale length, and the pink dots show low temperature structure's relationship. For easy comparison, pink dots are just plotted at right side of blue dots. And the range of standard deviation of time scale length is shown as bars. This result means the high temperature structure must be the low speed streak and it tends to be much longer time scale than low temperature structure. In other words, its shape is streaky.

## 5. Concluding remarks

Using OSIM, the spatiotemporal figure of TOS is clarified. Concluding remarks are follows;

1. Strong wind velocity produce slender TOS.
2. Mean span wise width and time scale length is in proportion, until its mean span wise width (7m).
3. The time scale lengths have their limitation.
4. High temperature structure tends to have much longer time scale length than low temperature structure have. This means the high temperature structure's shape is streaky.

From now on, the observation instruments must be well developed and much more accuracy observation will be done. For such a situation, OSIM must be one of good ways to investigate TOS. Moreover, if I can define the quantification of the complex shape, like meanderings, wheals and so on, the method works better and better, and contribute to clarify the behavior of TOS. And in future, if the quantification of TOS is successfully done with various roughness experiments such as changes of the plan area index or the height of cubic blocks, environmental assessment will be done.

## 6. Reference

- [1] Adrian, R. J., Meinhart, C. D., Tomkins, C. D. : Vortex organization in the outer region of the turbulent boundary layer, J. Fluid Mech., Vol. 422, pp1-54, 2000.

# Efficiency of the Implicit Finite Element Method on Geotechnical Engineering

Student Number: 05M18136, Name: FURUMURA, Takahiro, Supervisor: OHTA, Hideki

応力積分に陰的積分法を用いた弾塑性・静的有限要素法と、陽的積分を用いた弾塑性・静的有限要素法を、精度や計算コストの面から比較した。弾塑性構成モデルには修正カムクレイモデルを用い、通常の弾塑性変形解析のほかに、地盤中の間隙水の移動を考慮する擬似静的土／水連成解析についても検討した。

## 1. Introduction

This paper discusses the applicability of the implicit finite element (FE) method to geotechnical engineering. The implicit FE method, proposed by Simo (e.g. [1]), has been considered to be more accurate and more stable than conventional explicit methods. Borja applied it to geomechanics with the modified Cam-Clay model in [2] and [3], and the implicit FE method showed good accuracy and stability.

Although the implicit FE methods have been expected to be numerically accurate, this method requires far more computational costs than the explicit method. Considering that the accuracy of the explicit method becomes more accurate as the increment step-size decreases, the efficiency of the implicit FE method is in question. Several researches have been made on a comparison between the implicit FEM and the explicit FE methods. For instance, Harewood et al. and Sun et al. compared several implicit and explicit algorithms on commercial FE software in [4] and [5]. However, the studies on geotechnical problems seem to be missing before now. In this paper, we compare these two methods on several practical examples about soil structures.

## 2. The implicit FE method on geotechnics

In elasto-plasticity, the stress-strain constitutive models are generally expressed with stress-rate and strain-rate. Since numerical methods deal finite time-step size, this

Strain resolution	$\dot{\boldsymbol{\varepsilon}}^p + \dot{\boldsymbol{\varepsilon}}^e = \dot{\boldsymbol{\varepsilon}}$
Elastic constitutive model	$\dot{\boldsymbol{\sigma}} = \mathbf{C}^e : \dot{\boldsymbol{\varepsilon}}^e$
Consistent requirement	$\dot{f} = 0$
Associated flow rule	$\dot{\boldsymbol{\varepsilon}}^p = \dot{\gamma} \partial f / \partial \boldsymbol{\sigma}$
Hardening rule	$p_c = p_c \dot{\boldsymbol{\varepsilon}}_v^p / MD$

∇

Rate-formed stress-strain relationship

$$\dot{\boldsymbol{\sigma}} = \left[ \mathbf{C}^e : \frac{\partial f}{\partial \boldsymbol{\sigma}} \otimes \frac{\partial f}{\partial \boldsymbol{\sigma}} : \mathbf{C}^e \right] : \dot{\boldsymbol{\varepsilon}} = \mathbf{C}^{ep} : \dot{\boldsymbol{\varepsilon}}$$

∇

Increment-formed stress-strain relationship

$$\Delta \boldsymbol{\sigma} = \mathbf{C}_{|n}^{ep} : \Delta \boldsymbol{\varepsilon}$$

**Fig.1** A formulation of the stiffness matrix for the explicit method

Strain resolution	$\Delta \boldsymbol{\varepsilon}^p + \Delta \boldsymbol{\varepsilon}^e = \Delta \boldsymbol{\varepsilon}$
Elastic constitutive model	$\Delta \boldsymbol{\sigma} = D(\Delta \boldsymbol{\varepsilon}^e)$
Consistency requirement	$f = 0$
Associated flow rule	$\Delta \boldsymbol{\varepsilon}^p = \Delta \gamma \partial f / \partial \boldsymbol{\sigma}$
Hardening rule	$p_{q n+1} = p_{q n} \exp(\dot{\boldsymbol{\varepsilon}}_v^p / MD)$

∇

Increment-formed stress-strain relationship

$$\boldsymbol{\sigma}_{|n+1} = D(\Delta \boldsymbol{\varepsilon}, \boldsymbol{\sigma}_{|n})$$

**Fig.2** A formulation of the stiffness matrix for the implicit method



constitutive model must be integrated with respect to time.

In the explicit FE method, we firstly determine the rate-formed stiffness matrix, then integrate it with explicit numerical integration as fig.1. The stiffness matrix  $\mathbf{C}^{ep}$  is updated every step using the current stress state, and the next stress state is calculated with it. Since the forward Euler numerical integration is commonly used, smaller increment step size is required for reliable results. On the other hand, we can introduce analytical solutions or more accurate numerical integration schemes if the implicit method is used. In this research, we used the analytical solution to integrate the elastic constitutive model and the Crank-Nicolson method for the associated flow rule.

The implicit FE method solves non-linear system of equilibrium equations, while the explicit FE method solves linearized equilibrium equations. Therefore, the implicit method require iterative nonlinear solvers. The Newton method is commonly used. The gradient matrix for the Newton method, also called the consistent tangential matrix, can be obtained by solving the following linear system of equations.

$$\left[ \mathbf{I} + \left( \mathbf{C}^e : \frac{\partial f}{\partial \boldsymbol{\sigma}} : \frac{\partial \Delta \gamma}{\partial \boldsymbol{\sigma}} + \Delta \gamma \mathbf{C}^e : \frac{\partial^2 f}{\partial \boldsymbol{\sigma}^2} \right) \right] : \frac{\partial \boldsymbol{\sigma}}{\partial \boldsymbol{\varepsilon}} = \mathbf{C}^e \quad [1]$$

This matrix would be updated every iteration if the standard Newton method is used.

After solving the global matrix, we need to determine the stress for updated displacement. The updated stress can be obtained by solving the following non-linear system of equations for the  $\boldsymbol{\sigma}_{n+1}$ :

$$\Delta \boldsymbol{\sigma}_{n+1} = \mathbf{C}^e : \left( \Delta \boldsymbol{\varepsilon} - \Delta \gamma \frac{\partial f}{\partial \boldsymbol{\sigma}'_{n+1}} \right) \quad [2]$$

It is not guaranteed that eq.[2] has a unique solution. Even if eq.[2] has a unique solution, the Newton method might fail to find it. Since the failure of the stress-update algorithm lead the failure of over all calculation, some techniques might be required according to the plasticity models. Despite these difficulties, as long as the initial value of the Newton method was equal to the previous

stress state, the stress update algorithm using the modified Cam-clay model gave a good stability and valid solutions on most cases.

### 3. Efficiency improvement of the implicit FE program

The standard Newton method would show a very rapid quadratic convergence, however, the calculation costs of the Jacobian matrix  $\mathbf{J}$  itself and  $\mathbf{J}^{-1}$  are significant. To avoid the calculation of  $\mathbf{J}$  and the inverse of  $\mathbf{J}$ , various modification of the standard Newton method have been proposed. A natural choice would be the use of the modified Newton methods that use the same gradient matrix for some or all iterations. This results a large reduction of the CPU time concerning the matrixes, while this method requires far more number of iterations. Matthies and Straing showed that a more drastic modification of the modified Newton method is possible ([7]), for instance, using elastic tangential stiffness matrix instead of elasto-plastic consistent tangential stiffness matrix. If we use the elastic tangential matrix for over all calculations, the global tangential matrix  $\mathbf{K}$  keeps constant. Therefore, we do not need to solve the matrixes at each step and the LU factorization is required just once. Matthies et al. also showed that the difficulty would arise when we apply the modified Newton methods including the line search method to unloading problems [7].

A comparison between the standard Newton method and the modified Newton method is shown in fig.3. The elastic stiffness matrix is used for the initial tangential matrix of the modified Newton method. While the standard Newton method showed a quadratic convergence, the convergence of the modified Newton method is linear rather than quadratic. Considering the implicit FE method requires high computational costs for non-matrix calculation, such as the stress-update algorithm, it can be say that the modified Newton method is not efficient for elasto-plastic FE problems.

Fig.4 shows how the tolerances affect the

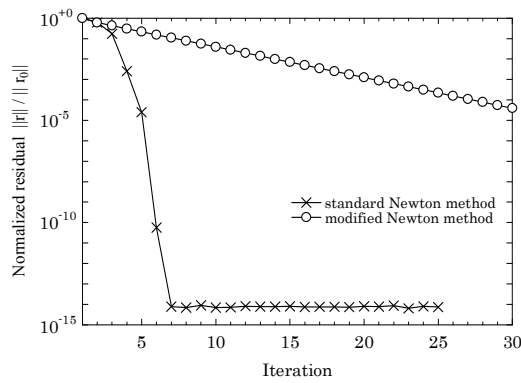
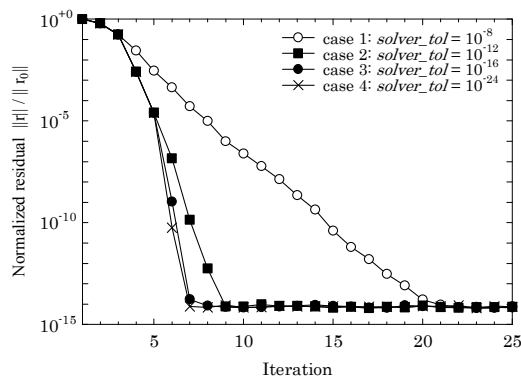


**Fig.3** Convergence of the Newton-type methods



	tolerance of the ILUBCG	tolerance of the stress-update algorithm
Case 1	$10^{-8}$	$10^{-7}$
Case 2	$10^{-12}$	$10^{-7}$
Case 3	$10^{-16}$	$10^{-7}$
Case 4	$10^{-24}$	$10^{-7}$

**Fig.4** Normalized norm of the global residual vector

convergence of the global equilibrium equations. The norm of residual vector normalized with the initial value is plotted. It seems that the tolerance of matrix-solver has much effect on the convergence, while the accuracy of the stress-update algorithm does not affect so much. The accuracy of the stress-update algorithm can reach enough level even if the tolerance is very loose because

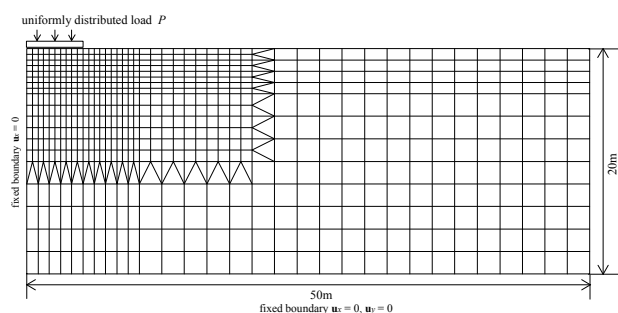


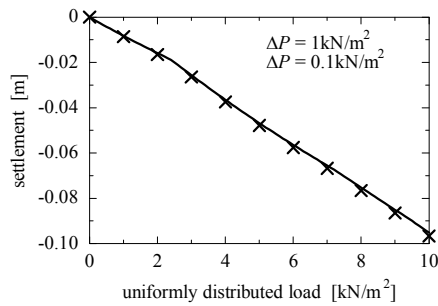
**Fig.6** Finite element mesh

its convergence is quadratic. The appropriate magnitude of matrix-solver tolerance seems to be  $10^{-12}$ .

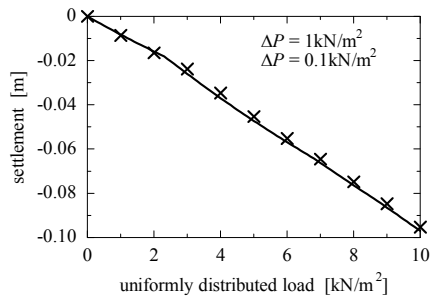
#### 4. Comparison with the explicit method

Fig.6 shows a 9m width surface foundation subjected to uniformly loading. Analyses were implemented with the implicit FE program and the explicit FE program. Although we expected that larger increment step-size led to less accurate results, no significant difference was observed between  $\Delta P = 0.1$  kN/m<sup>2</sup> and  $\Delta P = 1.0$  kN/m<sup>2</sup> in both the implicit FEM and the explicit FEM. Fig.7 indicates that the explicit FEM might be slightly inaccurate at the step when some elements yield, however, the error is not very large. From these results, we can say that the implicit FEM is completely not efficient for the problem on normally consolidated soil and has fewer advantages even in the problem on over consolidated soil. The explicit FEM would exhibit enough accuracy at a lower computational cost in this kind of practical problems.

The second example is an un-drained shear problem on axial symmetric strain condition shown in fig.8. An instable result was observed after  $q/p$  over the critical state parameter  $M$ . From the result of the implicit FEM are shown in fig.3.9, such instability was not observed but the calculation was failed when  $q/p$  over the critical state parameter. Clearly the stress state which satisfy  $q/p > M$  cannot be accepted because the model assume that the soil material shall fail when  $q/p = M$ . It can be concluded that the explicit scheme gives some solutions even in unrealistic situations and the solution is not always reliable. In contrast, the implicit FEM would stop in such situation but it does not provide unrealistic solutions.



**Fig.7.1** Settlement under the foundation (implicit)



**Fig.7.2** Settlement under the foundation (explicit)

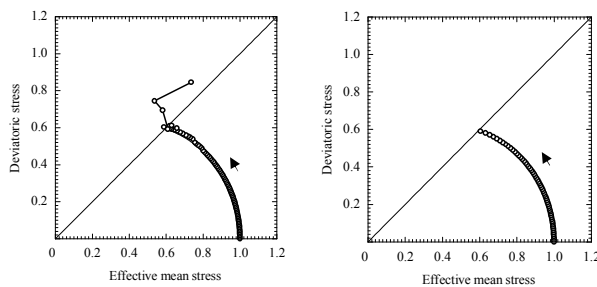


**Fig.8** Un-drained shear

## 5. Conclusion

A formulation of implicit elasto-plastic FE method for geotechnical problems was shown and compared with the explicit FE method. Although the implicit FE methods had been expected to be more accurate when larger step-sizes are used, no significant difference was observed in our research. The implicit method was slightly more accurate if the analysis includes yielding behavior, however, this advantage was not significant in practical analysis. In terms of computational costs, the implicit method required far more CPU time relative to the explicit method. Since we used the standard Newton method and it worked well, the convergence was quadratic. The required number of iterations was 3 or 4 for the tolerance we selected.

However, even if we could reduce the number of iterations, the computational cost of the implicit method can not below that of the explicit method which need not use iterative methods. Considering that the explicit method gave acceptable results even on larger step-sizes, it is doubtful that the implicit method is efficient in terms of accuracy and computational costs.

Some issues related to the efficiency improvement of the implicit FE method were also discussed. Firstly, the use of inexact Newton methods was discussed. The line search algorithm required more than 30 iterations to achieve the tolerance  $10^{-5}$  while the standard Newton method required 4. Considering the computational costs of non-solver processes, such as stress-update algorithm, are relatively high in implicit FE method. since inexact Newton methods reduces the CPU time for matrix-solver but does not reduces the other processes, it can be say that the standard Newton method should be used. The appropriate selection of tolerances was also discussed and it is shown that the optimization of tolerances can reduce the CPU time of analysis.

## 6. References

- [1] J.C. Simo and R.L. Taylor, "Consistent tangent operators for rate-independent elastoplasticity", *Computer Methods in Applied Mechanics and Engineering*, vol.48, 101-118 (1985)
- [2] R.I. Borja and S.R. Lee, Cam-Clay plasticity, part I: Implicit integration of elasto-plastic constitutive relations, *Computer Methods in Applied Mechanics and Engineering*, vol.78, 49-72, (1990)
- [3] R.I. Borja, Cam-Clay plasticity, part II: Implicit integration of elasto-plastic constitutive equation based on a nonlinear elastic stress predictor, *Computer Methods in Applied Mechanics and Engineering*, vol.78, 49-72, (1990)
- [4] F.J. Harewood and P.E. McHugh, Comparison of the implicit and explicit finite element methods using crystal plasticity, *Computational Materials Science*, (2006)
- [5] J.S. Sun, K.H. Lee, and H.P. Lee, Comparison of implicit and explicit finite element methods for dynamic problems, *Journal of Materials Processing Technology*, 105, 110-118, (2000)
- [6] A. Gens and D.M. Potts, Critical state models in computational Geomechanics, *Engineering and Computers*, 5, (1988)
- [7] H. Matthies and G. Strang, "The solution of nonlinear finite element equations". *International Journal for Numerical Method in Engineering*, vol.14, 1613-1626 (1979)

# Synthesis of Zeolites from Lake Sludge

Student Number: 05M18142    Name: Wei QU    Supervisor: Hirofumi HINODE

## 湖沼汚泥を原料としたゼオライトの合成

### 曲 巍

本研究では湖沼環境汚染の原因である湖沼汚泥の有効利用を目的とし、湖沼汚泥からアルカリ水熱合成によってゼオライト結晶への転換の可能性を研究した。アルカリ濃度、反応温度、反応時間および固液比の合成したゼオライトに対する影響について検討した。アルカリ水熱処理により、主に2つのタイプのゼオライトが生成した(ゼオライト NaP1、Analcime-C)。合成したゼオライトの陽イオン交換容量(CEC)および重金属吸着実験を行い、吸着性能について検討した。その結果、天然ゼオライトと同等の CEC 値を有することからゼオライトの用途である吸着剤また土壌改良剤としての利用の可能性を見出した。

## 1. Introduction

Lake pollution is serious because lakes are closed water systems and contaminants can accumulate easily. Discharge from households and factory flow to lake. Contaminants in the discharge accumulate on the bottom of lake, and they become lake sludge. Lake sludge causes deterioration of water quality and produces negative impacts on ecosystems and households using lake water. Therefore, it must be treated adequately.

Lake sludge is mainly treated by dredging method which remove sludge from the bottom of a lake using a dredging ship or machine. This method generate large amount of lake sludge that still need to be treated. Some methods to treat dredged sludge are landfill, incineration, but they have problems of the lack of space, cost, energy efficiency. Previous study showed that coal fly ash can be converted into zeolites by hydrothermal treatment<sup>[1]</sup>. Since the main components of lake sludge are silica and alumina which is similar to the chemical components of coal fly ash, it can be expected that lake sludge could also be used as raw materials for synthesizing zeolite .

In this study, hydrothermal synthesis of zeolite from lake sludge in alkali solutions was tried, and the synthesis reaction conditions and the application of the zeolite synthesized from lake sludge were

investigated.

## 2. Experimental

### 2.1 Synthesis of zeolites

#### (1)Materials

Lake sludges from Kasumigaura and Teganuma were used in this study. After being crushed to particle with size less than 150 $\mu$ m, the sludge was dried at 105°C for 24h. The sieved sludge was stored in a plastic bottle at room temperature as raw material for this study.

#### (2)Method

Lake sludge was mixed with sodium hydroxide solution (NaOH) and was shaken for 24 h in a 23ml Teflon reaction vessel. The vessel was then put inside autoclave and incubated at a temperature of 90 to 150°C in an oven. After the reaction, the slurry was filtered and the solid phases were washed several times with distilled water to eliminate the excess NaOH. The washed solid phase was air-dried and stored in the plastic bottle at room temperature as the products.

### 2.2 Characterization

The products obtained were characterized as follows. The identification of crystalline materials in sludge and synthesized zeolitic products was carried out by X-ray diffraction (XRD). The specific surface structure was observed by scanning electron

microscopy (SEM). The surface area was measured by using BET method.

### 2.3 Cation-exchange capacity(CEC) measurement

The cation-exchange capacity was determined by sodium acetate method<sup>[2]</sup>. The sample was saturated with NaOAc solution (pH 5.2), and then the  $\text{Na}^+$  was extracted by  $\text{NH}_4\text{OAc}$  solution. The amounts of released  $\text{Na}^+$  were measured using Inductively Coupled Plasma- Atomic Emission Spectrometry equipment (ICP-AES).

### 2.4 Heavy metal adsorption

The synthesized zeolites were evaluated on their capability to remove heavy metal in aqueous solutions. 50ml of solution containing different concentrations of  $\text{Pb}^{2+}$  or  $\text{Cd}^{2+}$  were poured into a glass bottle with 0.1 g sample and were shaken at 150rpm for 24h. After equilibration period, solid and liquid were separated by centrifugation and filtration (0.45 $\mu\text{m}$  membrane filter). The concentration of  $\text{Pb}^{2+}$  or  $\text{Cd}^{2+}$  in solution were determined by ICP.

## 3.Results and Discussion

### 3.1 The synthesis of zeolites( XRD analysis)

The results from XRD analysis of obtained products with various NaOH concentrations are shown in Figure 1. With NaOH concentration of 1M and below, the zeolite NaP1( $\text{Si}/\text{Al}=1.67$ )<sup>[1]</sup> was formed as shown in the XRD patterns. Quartz phase was also present. At 2M NaOH concentration, it appeared that the zeolite Analcime-C ( $\text{Si}/\text{Al}=2$ )<sup>[1][3]</sup> phase was formed. It is possible that zeolite type changes due to the Si/Al ratio in the liquid phase. At NaOH concentration greater than 2M, zeolite NaP1 and Analcime-C disappeared due to the formation of Unnamed zeolite.

Temperature is also an important factor affecting the formation of zeolite (Figure 2). Formation of zeolite NaP1 was observed at temperature of 90 to 120°C, while zeolite Analcime-C was formed at

temperature of 120 to 150°C. In addition, zeolite NaX peak appeared on the diffractogram at 90°C.

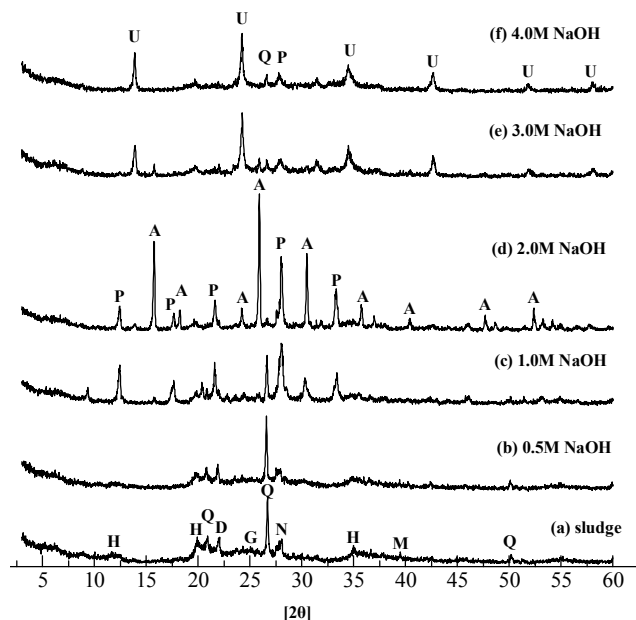


Figure 1. XRD pattern of the products obtained from various NaOH concentrations (L/S=5ml/g, 120°C-24h)

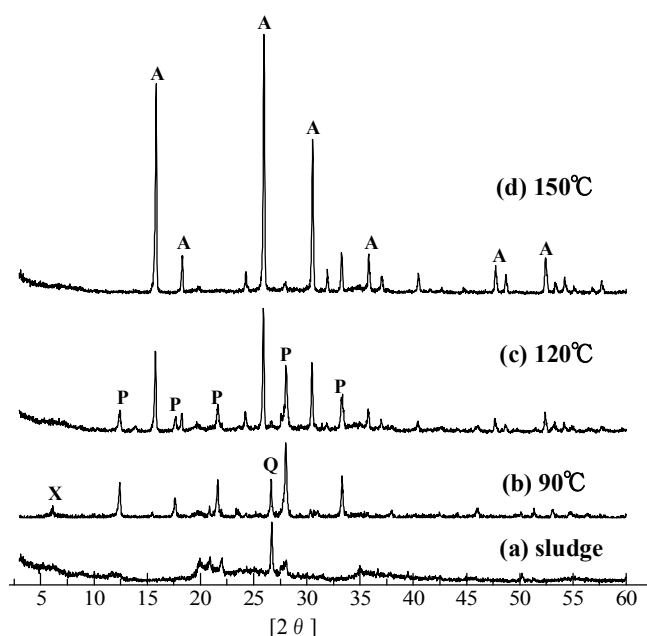


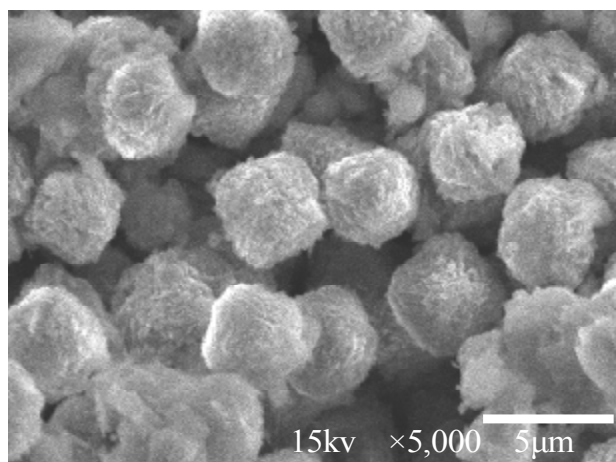
Figure 2. XRD pattern of the products obtained from Various reaction temperature(2M NaOH, L/S=5ml/g, 24h)

Q: Quartz ( $\text{SiO}_2$ )    H: Halloysite-7A ( $\text{Al}_2\text{Si}_2\text{O}_5(\text{OH})_4$ )  
 G: Greenalite-1M ( $\text{Fe}_6\text{Si}_4\text{O}_{10}(\text{OH})_8$ )    D: Dickite-2M1 ( $\text{Al}_2\text{Si}_2\text{O}_5(\text{OH})_4$ )  
 M: Quintinite-3T ( $\text{Mg}_4\text{Al}_2(\text{OH})_{12}\text{CO}_3 \cdot 3\text{H}_2\text{O}$ )    N: Albite ( $\text{NaAlSi}_3\text{O}_8$ )  
 P: Zeolite NaP1( $\text{Na}_6\text{Al}_6\text{Si}_{10}\text{O}_{32} \cdot 12\text{H}_2\text{O}$ )  
 A: Analcime-C( $\text{Na}(\text{AlSi}_2\text{O}_6) \cdot \text{H}_2\text{O}$ )  
 U: Unnamed zeolite( $\text{Na}_6(\text{AlSiO}_4)_6 \cdot 4\text{H}_2\text{O}$ )  
 X: Zeolite NaX ( $\text{Na}_2\text{Al}_2\text{Si}_2\text{O}_9 \cdot 6.2\text{H}_2\text{O}$ )

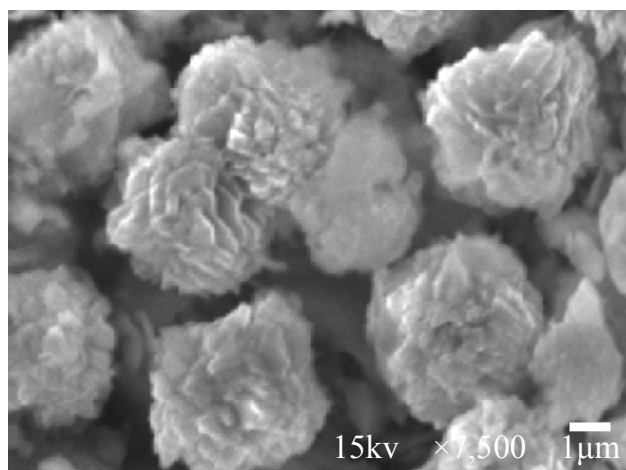
### 3.2 The synthesis of zeolites ( Observations by SEM)

SEM images of zeolite NaP1 obtained by hydrothermal treatment were shown in Figure 3. The formation of zeolite NaP1 as a fine crystal with a diameter of approximately  $5\mu\text{m}$  can be clearly observed.

SEM images of zeolite Analcime-C obtained by hydrothermal treatment were shown in Figure 4. At the condition of 2M NaOH and  $150^\circ\text{C}$ , the formation of zeolite Analcime-C with a diameter of  $10\mu\text{m}$  can be clearly seen.

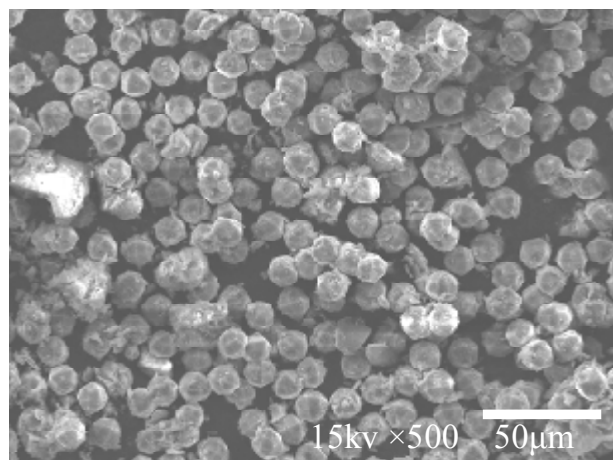


(a) 1M NaOH, L/S=6ml/g,  $120^\circ\text{C}$ -24h

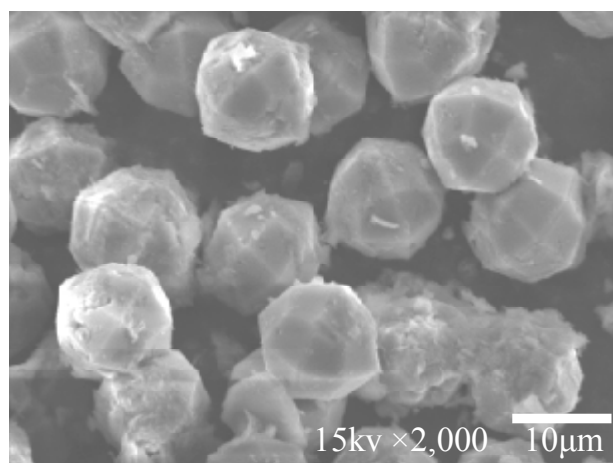


(b) 1M NaOH, L/S=7ml/g,  $120^\circ\text{C}$ -24h

**Figure 3. SEM images of zeolite NaP1 obtained by hydrothermal treatment.**



(a) 2M NaOH, L/S=4ml/g,  $150^\circ\text{C}$ -24h



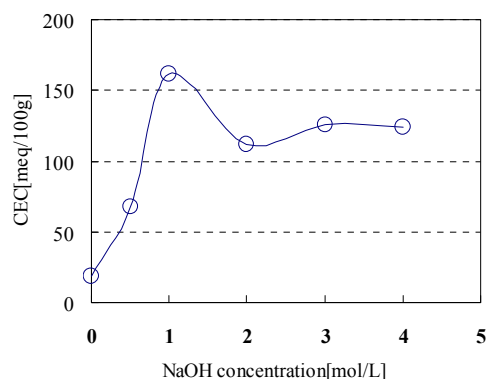
(b) 2M NaOH, L/S=5ml/g,  $150^\circ\text{C}$ -24h

**Figure 4 SEM images of zeolite Analcime-C obtained by hydrothermal treatment.**

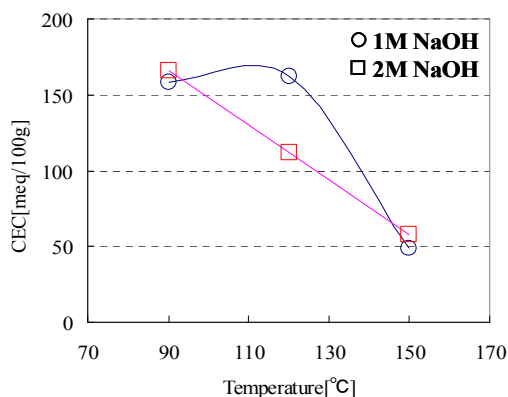
### 3.3 The Cation-Exchange Capacity(CEC)

Figure 5 shows the value of CEC of products obtained from different NaOH concentrations. The CEC was greatly increased until product with 1M NaOH, and then was decreased between 1M and 2M NaOH, and were constant after 3M. Based on the XRD results, the formation of zeolite NaP1 seemed to be responsible for the increase of CEC, and the formation of zeolite analcime-C caused the decrease of CEC. It is possible that changes in zeolite type lead to different CEC values. Figure 6 shows the value of CEC of products obtained from different temperatures. The CEC greatly decreased as the temperature increased to  $150^\circ\text{C}$ . Based on XRD

results, it indicated that zeolite Analcime-C has lower CEC value than zeolite NaP1.



**Figure 5. CEC of the products obtained from various NaOH concentrations (L/S=5ml/g, 120°C-24h)**



**Figure 6. CEC of the products obtained from various reaction temperature (L/S=5ml/g, 24h)**

### 3.4 Heavy metal adsorption

Table 1 shows the adsorption capacity of  $Pb^{2+}$  and  $Cd^{2+}$  for various synthesis conditions. These adsorption results demonstrated that the increase of BET surface area of treated lake sludge provided a better adsorptive capability toward Pb and Cd removal.

## 4. Conclusions

Lake sludge was successfully converted into zeolites. Zeolite NaP1 and Analcime-C was formed through the hydrothermal treatment in alkali solutions. Zeolite NaP1 was formed at 1~2M of NaOH solution and at 90~120°C. Analcime-C was identified at 1~2M of NaOH solution and at treatment temperature between 120 and 150°C. The cation exchange capacities of the products ranged from 49 to 173 meq/100g. The zeolitized products obtained from this study have the same cation-exchange capacities as the commercial natural zeolites (about 50 to 170 meq/100g). Obtained zeolites also have adsorptive capability toward  $Pb^{2+}$  and  $Cd^{2+}$  ions.

The zeolite synthesized from lake sludge in this study could be applied for several applications such as soil improvement or water purification.

## References

- [1] X. Querol, N. Moreno, J. C. Umaña, A. Alastuey, E. Hernández, A. López-Soler and F. Plana: 'Synthesis of zeolites from coal fly ash: an overview', *International Journal of Coal Geology*, Volume 50, Issues 1-4, May 2002, Pages 413-423
- [2] United States Environmental Protection Agency, [http://www.epa.gov/Method9081,Cation-Exchange Capacity of Soils \(Sodium Acetate\)](http://www.epa.gov/Method9081/Cation-Exchange Capacity of Soils (Sodium Acetate))
- [3] N. Shigemoto, S. Shirakami, S. Hirano and H. Hayashi, 'Preparation and characterization of zeolites from coal fly ash. *Nippon Kagaku Kaishi* 5(1992), pp.484-492

**Table 1. BET surface area, CEC, and adsorption capacity of  $Pb^{2+}$  and  $Cd^{2+}$  for various synthesis conditions.**

Zeolite Product	$S_{BET}(m^2/g)$	CEC(meq/100g)	$X_m(mg/g)$ for $Pb^{2+}$	$X_m(mg/g)$ for $Cd^{2+}$	Major phase
P1 (90°C)	93.522	166	54.945	39.841	NaP1+NaX(tr)
P2 (120°C)	59.407	173	42.194	35.336	NaP1
P3 (150°C)	29.724	58	35.546	19.531	Analcime-C

# Influence of creep phenomenon on manipulation by shape control of rubber-elastic membrane

Student Number:05M18159 Name:CHANG Xuanxuan Supervisor:Kunio TAKAHASHI

ゴム弾性膜の形状制御によるマニピュレーションに及ぼすクリープ現象の影響

常 軒軒

マニピュレーションを行う時に表面凝着力を調整できるなら簡単に操作が出来る。表面凝着力は、接触部分の等価曲率半径  $R$  によって決められる。それで、プローブの先端を変形させて、操作を行う方法を学部論文時に提案した。圧力によるゴム弾性膜の形状を制御する実験を行った。静電容量式変位計を用いて、弾性膜先端の変位を計測できた。しかし、圧力をかけると、クリープ現象が発生する。クリープ現象は、形状制御に対する影響を検討した。

## 1 Introduction

A tool such as a pair of tweezers that is designed to use with millimeter-sized or bigger objects, doesn't function effectively in the micro-manipulation of micro-scaled objects. In micro-manipulation, adhesion force becomes dominant rather than the gravitational force. In various manipulation methods, there is a mechanical method for manipulation by using the difference of adhesion forces between the object and the tool, and the object and the substrate. When we use the mechanical method, it is considered that we can advantageously manipulate objects by changing adhesion force. According to JKR theory[1], adhesion force can be determined by the equivalent radius of curvature  $R$  and the work of adhesion  $\Delta\gamma$ . Based on this theory, we can control the adhesion force in the micro-manipulation by controlling the equivalent radius of curvature. In earlier study, K. J. Obata et al. have investigated the manipulation using capillary force with a concave probe-tip[2]. In these two methods, it can be considered that the shape at the contact part can influence the manipulation.

A thin elastic membrane seems easy to change its shape (inflate or deflate). In this study, we focus on how to control the shape of a thin elastic membrane in order to use in the micro-manipulation by controlling the air pressure. An experiment was carried out to study the influence of creep phenomenon on the manipulation by shape control of the membrane.

But, because impurities are contained a lot in rubber, it is difficult to obtain rubber with high purity. So, the traceability is low. To solve it, we select 3 kinds of rubber, which are a natural rubber (250 $\mu$ m thick), a natural rubber excluding protein (100 $\mu$ m thick), and a nitrile rubber (100 $\mu$ m thick).

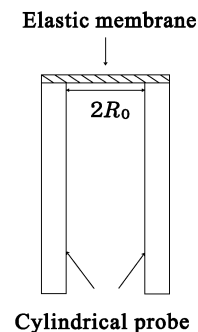


Fig. 1: Probe

In the experiment, the rubber membrane is stuck to one end of the cylindrical probe by bond, as shown in Fig.1. The membrane is then washed with the ethanol for ten seconds, and by pure water using an ultrasonic cleaner for three minutes.

## 2.2 Experimental system

The experiment system we designed to use in this study, as shown in Fig.2, consists of two main parts. The measuring part (Part A) is to measure the displacement of the center of the elastic membrane caused by the deformation, and the pressure-control part (part B) is to control the pressure, and consequently control the deformation of the membrane. Below, we are going into details of each part.

## 2 Experiments

### 2.1 Sample preparation

We selected rubber to be used as the material of the membrane, because rubber can have large deformation, and plastic deformation doesn't happen easily.



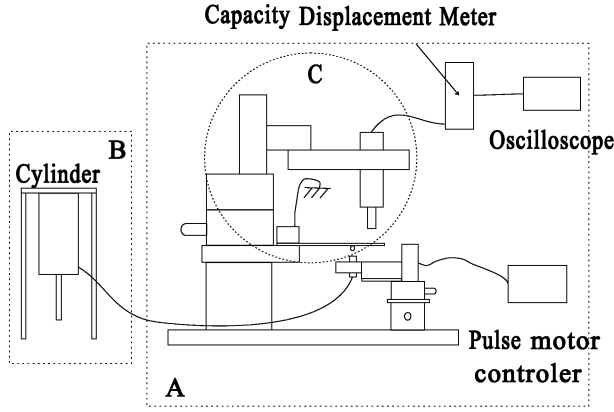


Fig. 2: Experimental system

### 2.2.1 Measuring displacement

Fig.3 illustrates the configuration of the force sensor (part C in Fig.2). A capacitive displacement meter (Iwatsu ST-0536A) equipped with a probe (ST-0536A) is used. This meter can measure the displacement of conductors, e.g. a cantilever for this study, using a non-contact method, and outputs voltage with high precision in proportion to the displacement. A cantilever (SUS304) is set right below the probe of manipulation, on which a glass ball ( $\phi = 2.1\text{mm}$ ), to be used as the manipulated object, is stuck at a distance  $a$ .

An elastic membrane (natural rubber), as the manipulator, is stuck to one end of the cylindrical probe of 4mm inner diameter, the other end of the manipulation probe is connected to the air-cylinder (part B) for which the shape of the membrane can be controlled by adding/reducing pressure. The membrane is set below the glass ball and can be driven up-down by a pulse motor controller (Suruga Seiki, Model D100) with a distance resolution of  $0.05\mu\text{m}$ .

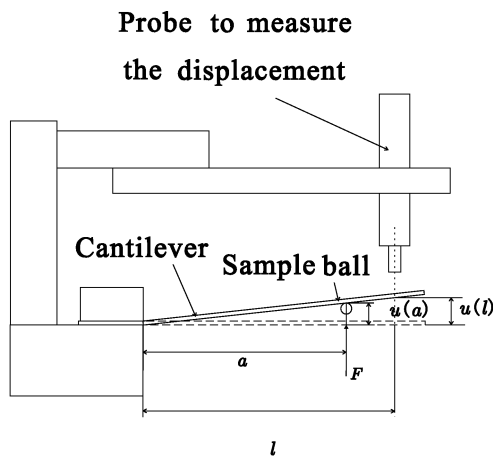


Fig. 3: System of the cantilever

By driving the membrane upward the glass ball, when they come in contact, a force  $F$  will be exerted

to the glass ball and make the cantilever bend. The corresponding displacement of the cantilever at distance  $l$   $u(l)$  (also  $u(a)$ ) will be measured by the displacement meter. The relation between  $F$  and  $u(l)$  can be express as,

$$F = \frac{6EI}{a^2(3l - a)}u(l) \quad (1)$$

where  $I$  is the cross-sectional moment of inertia and  $E$  is the Young modulus. According to this, we can measure the position where the probe and the ball come in contact. Therefore, the displacement of the center of the elastic membrane can be measured.

Since the force considered in this study is very small, it is necessary to design the measuring part to have sufficiently high resolution to measure it. We select a cantilever with the length  $l = 40\text{mm}$ , the width  $b = 2.65\text{mm}$ , and the thickness  $h = 0.15\text{mm}$ . The resolution of the displacement meter is  $\Delta u$  is  $1 \times 10^{-9}\text{m}$ . Although, the model of this study differs from those of the JKR theory, we attempt to roughly estimate the adhesion force to be  $47\mu\text{N}$ . Then, we initially determine the resolution as  $0.47\mu\text{N}$ ,  $1/100$  of that estimated by the JKR theory. When we determine the distance  $a=30\text{mm}$  as the position to stick the glass ball to satisfy the above-mentioned condition. The force resolution of this system is  $1.2 \times 10^{-8}\text{N}$ .

### 2.2.2 Pressure control

To control the deformation (shape) of the elastic membrane, we select an air cylinder (SMC, CDM30-200) which the inner diameter is 30mm, and the stroke is 200mm. The air cylinder is connected to the manipulation probe where the membrane is stuck to via a pressure meter (KEYENCE, AP-C30) with a resolution of  $0.1\text{kPa}$ , as shown in Fig.4.

Weight is loaded to the cylinder to compress or decompress the air, accordingly, the membrane will inflate or deflate. The pressure meter shows a positive value for the compressed pressure, and a negative value for the decompressed pressure. The experiment was carried out in atmosphere, hence the variation of pressure ranges from  $-0.1\text{MPa}$  to  $0.1\text{MPa}$ .

## 2.3 The process of the experiment

The process of the experiment:

1. Drive the membrane upwards to the sample ball.
2. When they come in contact, the change of the force will be measured.
3. The probe's displacement record, and this position are set up in 0.
4. Drive the membrane down.

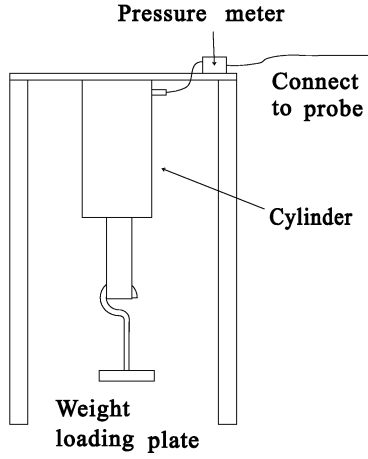


Fig. 4: Pressure control part

5. Repeat step 1,2 after a time interval.
6. Record the probe's displacement, and drive the membrane down.
7. Change the pressure, and repeat step 5,6.

By these processes, we can obtain the flexure of the center of the membrane.

### 3 The creep phenomenon of the deformation of the membrane

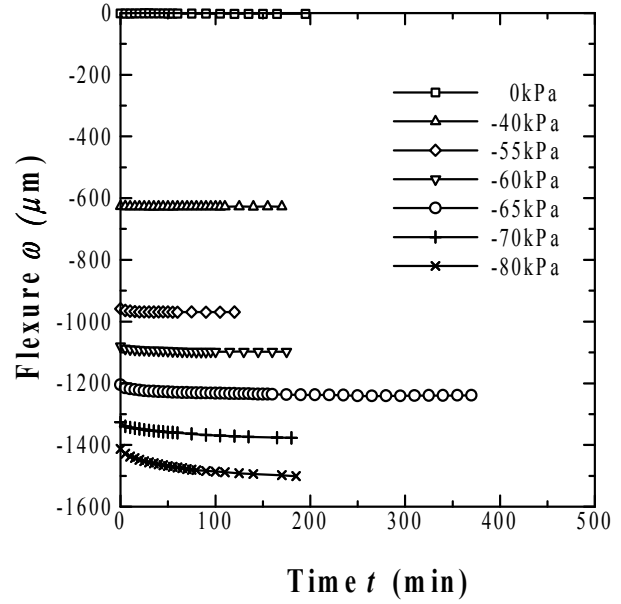
#### 3.1 Experiment result of deformation

The flexure  $\omega$  of the center of each membrane was measured. We use the probe of 4mm inner diameter  $R_0$ , and the sample ball is a glass ball of 2.1mm diameter. According to the measurement result in Fig.5 The thinner the membrane, the larger the membrane deforms.

#### 3.2 Influence of creep phenomenon

In the experiment, we found that the membrane, during a constant pressure is applied, keeps deforming with several speeds corresponding to the applied pressure .e.g. Fig.5 shows that, when the elastic membrane and the glass ball come in contact. The membrane deforms at a constant strain rate when time passes.

This can be considered as the creep phenomenon[3][4]. The phenomenon was observed and examined throughout the experiment. Because the thin membrane is used, we can suppose the center of the membrane is uniform equibiaxial tension[5]. Then, we use the natural rubber, so we can suppose the rubber's volume is constant[6]. By this assumption, we can calculate the strain at


 Fig. 5: Relationship between the pressure  $P$  and the strain rate  $\dot{\varepsilon}$  (Natural rubber ( $250\mu\text{m}$  thick))

the center of the membrane. The relation between strain  $\varepsilon$  and flexure  $\omega$  is (2).

$$\varepsilon = \left( \frac{3R_0}{4\omega + 2R_0} \right)^{-\frac{1}{2}} - 1 \quad (2)$$

The result of the change of the strain is shown in Fig.5.

Using the result, we can calculate the strain rate  $\dot{\varepsilon}$ . By the result of the experiments, we can know that pressure decreases, and the constant strain rate decreases.

As shown in Fig.7, the constant strain rate  $\dot{\varepsilon}$  becomes almost 0, when pressure becomes below a certain value. The constant strain rate has the relation when the material is metal[3].

$$\dot{\varepsilon} = k\sigma^n \quad (3)$$

$\sigma$  is stress,  $k, n$  are constants that depend at temperature. The constant strain rate approaches gradually 0, when the fitting is done by the least square method like the metal. Because the metal's  $n$  is 4~6, so we used  $n = 4, n = 6$ . It differs from the experiment result. So, we can be considered that the creep phenomenon that is different from the metal occurs, when the rubber membrane was deformed. And others material show the same tendency, as shown in Fig.8.

### 4 Conclusion

It has been realized to be able to control the deformation of an elastic membrane that stuck on the

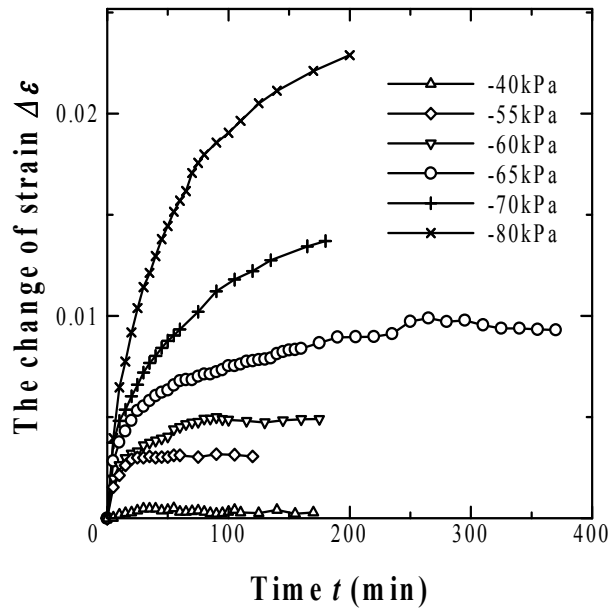


Fig. 6: Relationship between the change of strain  $\Delta\epsilon$  and time  $t$  (Natural rubber (250 $\mu$ m thick))

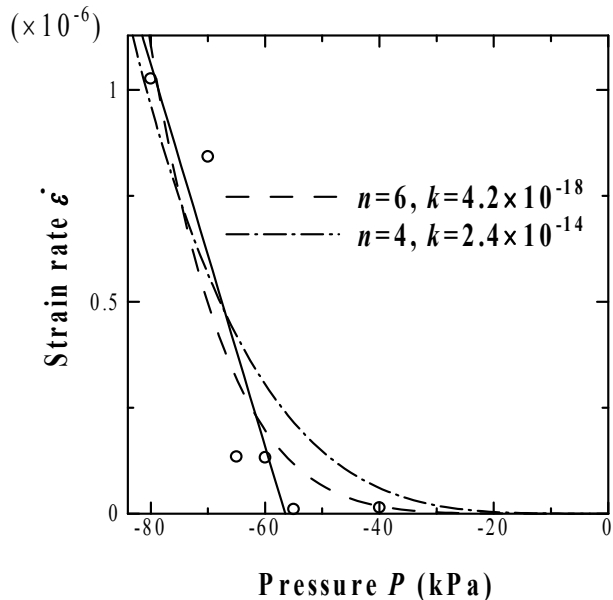


Fig. 7: Relationship between the pressure  $P$  and the constant strain rate  $\dot{\epsilon}$  (Natural rubber (250 $\mu$ m thick))

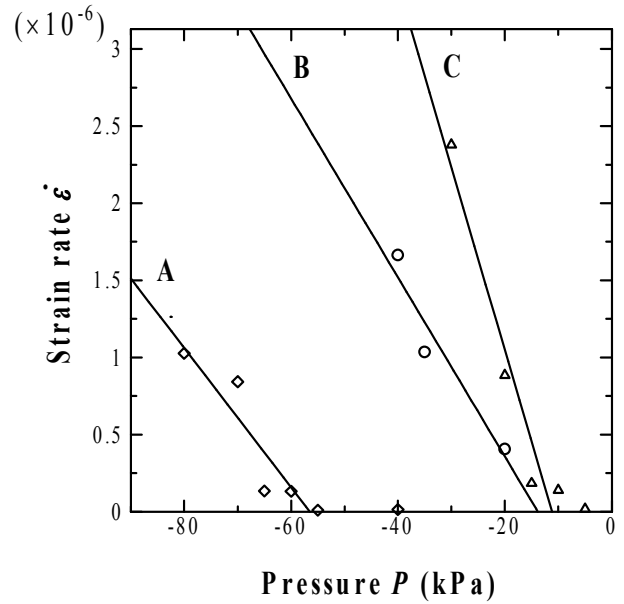


Fig. 8: Relationship between the pressure  $P$  and the constant strain rate  $\dot{\epsilon}$ , A: Natural rubber, B: Natural rubber excluding protein, C: Nitrile rubber

top of the manipulation probe by controlling pressure. It was confirmed that the creep phenomenon occurs on the elastic membrane by pressure. By the result of the experiments, the rubber membrane of different materials shows the same tendency that the constant strain rate  $\dot{\epsilon}$  becomes almost 0 when pressure becomes below a certain value. Because the rubber membrane of different materials has the different characters, the values are also different. When the deformation is controlled, the creep phenomenon can be suppressed if the pressure is below a certain value, which can be obtained from the experiment.

## References

- [1] K. L. Johnson, K. Kendall, and A. D. Roberts: "Surface energy and the contact of elastic solid," Proceedings of the Royal Society of London, A.324, pp.301-313, 1971
- [2] Shigeki Saito, Tomoyuki Motokado, Kenichi J.Obata and Kunio Takahashi: "Capillary force with a concave probe-tip for micromanipulation," Applied Physics Letters 87,234103,2005
- [3] F.K.G. オドクヴィスト, J. ハルト 共著, 村上澄男 訳: "クリープ強さの理論", 培風館
- [4] "ゴム試験法", 日本ゴム協会
- [5] 渋谷寿一, 本間寛臣, 斎藤憲司, "現代材料力学", 朝倉書店,2001
- [6] 久保亮五, "ゴム弾性 [初版復刻版]", 裳華房,1996

# Development of a Stored Channel Model for UWB Link Level System Design and Evaluation

Student number: 05M18165

Name: Huynh Thi Thanh Trieu

Supervisor: Jun-ichi TAKADA

## Abstract

超広帯域 (UWB) 無線は低電力で高速なデータ伝送を実現できる技術として近年注目を集めている。実環境下における UWB 通信の伝送特性評価および設計においては、ストアドチャネルシミュレーションが有効な方法として知られている。本研究は、まずストアドチャネルシミュレーションによる UWB 伝送特性評価の有効性を実機との比較により検証する。次に、伝搬路の特性を面的に網羅するストアドチャネルモデルを構築し、伝搬損失や遅延広がりなど UWB 伝送特性に影響する伝搬パラメタの分布を導出する。さらに、インパルス無線型 UWB 伝送において用いられる Rake 合成法の性能を評価し、その最適設計について指針を与える。

## 1. INTRODUCTION

Ultrawideband (UWB) signals use a large bandwidth with low power emissions. This can lead to new interesting possibilities for both communications and radar applications [1]. For this reason, UWB systems have been investigated for many years. UWB radio is adopted as a physical layer for high and low data rate wireless personal area networks (WPANs). Standardization activities of WPAN have been performed in the IEEE 802.15 Task Group 3a and 4a for high and low data rate systems, respectively. In order to compare standardization proposals, they have developed new standardized channel models [2], [3]. These channel models are stochastic models based on probability theories and thus are not suitable for evaluating the transmission in realistic environments. On the other hand, stored channel simulations are often used to reflect the properties of propagation channels in a real environment for device testing [4]. However, whether the stored channel can exactly simulate the real propagation environment has not been verified. Besides, there have not been many stored channel models [5], [6], [7]. To solve the problems stated above, our research objectives are set to the following three-fold: (1) to verify the effectiveness of the stored channel simulation in evaluating UWB system performance, (2) to develop a stored channel model for an indoor office environment and (3) to evaluate the transmission performance using the developed stored channel model.

## 2. VALIDATING THE EFFECTIVENESS OF UWB TRANSMISSION SIMULATION USING A STORED CHANNEL

### A. Experiment

In order to verify the effectiveness of stored channel simulations, we compared the actual received waveform measured by

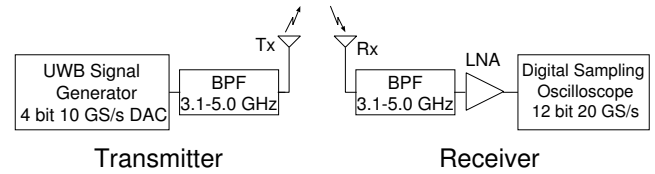


Fig. 1: Block diagram of UWB testbed

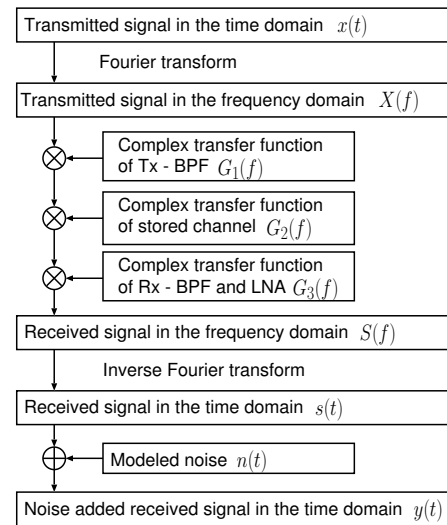
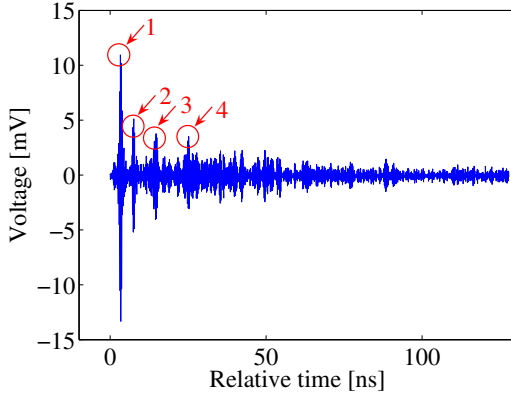


Fig. 2: Flow chart of received waveform simulations using a stored channel

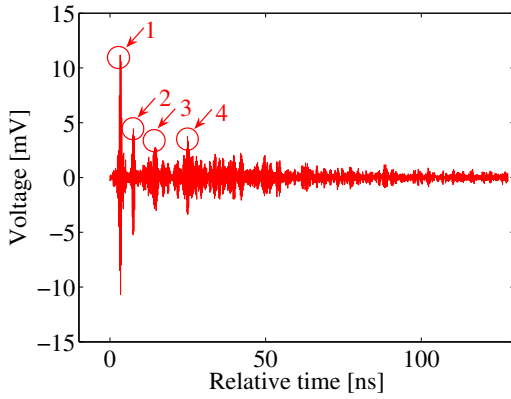
a UWB testbed [8] to the received waveform obtained from stored channel simulations.

We conducted two experiments: transmission experiment and propagation experiment. Both experiments were performed in the same propagation environment with the same antenna position in a rich multipath indoor office environment. There were numerous clutters such as metal partitions, desks, electronic equipments around the transmit and receive antennas.

1) *Transmission experiment*: The transmission experiment was performed using the UWB testbed, whose diagram is described in Fig. 1. On the transmitter side, the signal generator equipped with 10 GS/s, 4-bit DA Converter (DAC) was used to directly generate the UWB signals up to 5 GHz. The transmitted signal was the impulse response of a Root-Raised Cosine (RRC) filter modulated by a sinusoidal wave with frequency  $f_c = 4.05$  GHz [8]. These signals are then sent to the transmit antenna after limiting the bandwidth to 3.1 – 5.0 GHz using the BPF.



(a) actual measurement

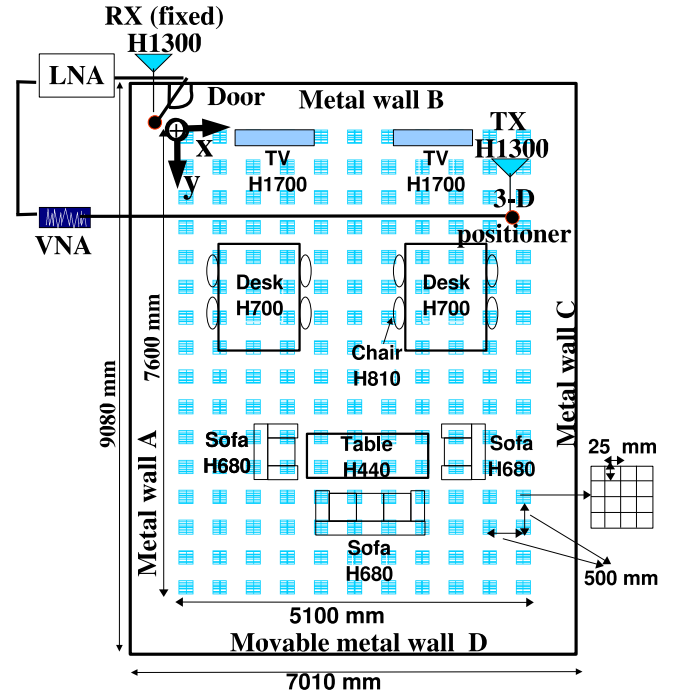


(b) stored channel simulations

**Fig. 3:** Received waveform

On the receiver side, the signal received from the receive antenna passes through the BPF to reduce the out-of-band interference. They are then amplified by LNA and finally time domain waveform was detected at 12 bits, 20 GS/s high-speed DSO. The averaging function of DSO was used in order to improve the signal-to-noise ratio (SNR) in the received waveform.

2) *Propagation experiment:* In order to obtain the received waveform via stored channel simulation to compare with the received waveform in the UWB testbed, we used a vector network analyzer (VNA) to measure the transfer function  $G_2(f)$  of the propagation channels including both transmit and receive antennas. The transfer functions  $G_1(f)$  of BPF on the transmitter side and  $G_3(f)$  of BPF and LNA on the receiver side of the UWB testbed were also measured with the VNA. The measured transfer functions were then used to reconstruct the received waveform as described in Fig. 2. In the reconstruction of the received waveform, the same transmitted waveform as the UWB testbed was considered.

**Fig. 4:** Floor plan of the measurement environment**TABLE 1:** SPECIFICATIONS OF THE MEASUREMENT

Bandwidth	3.1 – 10.6 GHz
Number of sweeping points in the frequency domain	1501 points ( $0 \leq y \leq 4600$ ) 3001 points ( $5000 \leq y \leq 7600$ )
Transmit antenna	UWB monopole antenna
Height of transmit antenna	1300 mm
Receive antenna	UWB monopole antenna
Receive antenna position	(-450, -20, 1300)
Room size	$7015 \times 9080 \times 2700 \text{ mm}^3$
Measured area	plane of $5100 \times 7600 \text{ mm}^2$
Number of array elements	$5 \times 5$
Inter-element space	25 mm
Inter-array interval	500 mm
Number of spatial samples	4205 points

## B. Results and discussion

The waveform obtained from the transmission experiment and reconstructed waveform via stored channel simulations are shown in Fig. 3. Comparison of the two waveforms revealed that multipath signals appeared at the same delayed time compared to the direct signal in both waveforms. In addition, focusing on the four strongest waves, it was found that wave 1 was the direct wave and waves 2, 3, 4 were the reflected waves with the delayed time of 4.3, 11.4, 21.7 [ns] respectively. Moreover, the peak amplitude values in two received waveforms were almost the same. Finally, the correlation of this two waveforms was 0.87, which proved that the received waveform obtained from actual measurement was nearly identical to the one obtained from stored channel simulations.

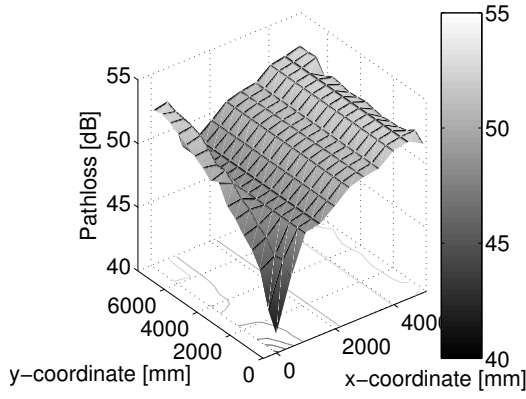


Fig. 5: Spatial distribution of pathloss

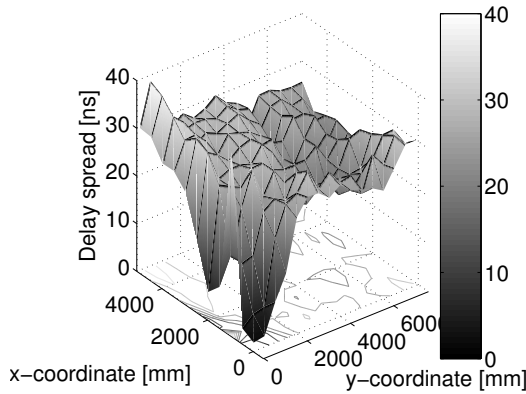


Fig. 6: Spatial distribution of the delay spread

### 3. DEVELOPMENT OF A STORED CHANNEL MODEL FOR THE DESIGN OF UWB COMMUNICATION SYSTEMS IN AN OFFICE ENVIRONMENT

Having verified its effectiveness in the previous section, we next develop stored channel models for transmission simulations. Basic properties of propagation channels, such as pathloss and delay spread, are also shown to facilitate discussion on the relationship between transmission performance and propagation characteristics.

#### A. Measurement campaigns

The spatial transfer functions were measured in a testroom equipped with three-dimensional scanner and a VNA as shown in Fig. 4. There are desks, chairs, televisions and sofas in the room. The walls were made of metal. In Fig. 4, the coordinate system is also shown. The specifications of the measurement are shown in Table 1.

#### B. Extraction of propagation parameters

1) *Pathloss*: The attenuation due to propagation effects between transmitter and receiver is defined as pathloss. It determines the average signal-to-noise ratio (SNR) that a

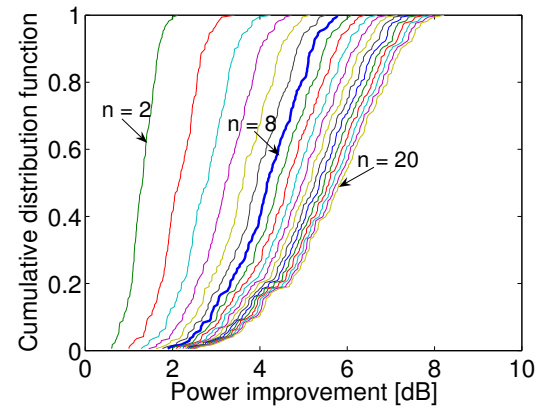


Fig. 7: Cumulative distribution of the improvement when SRake receiver is applied

system can achieve. Figure 5 illustrates the spatial distribution of pathloss.

2) *Delay spread*: The root-mean-square delay spread, which is defined as the normalized second-order central moment of power delay profile (PDP), has a significant influence in the error probability [4]. The area distribution of the delay spread is shown in Fig. 6.

It was found that both parameters were generally dependent on the distance between TX and RX antennas. The pathloss was about  $-40$  dB when TX-RX distance was small. On the other hand, it became more when TX moved far from RX. There was less spread when TX located near RX and more spread when TX was far from RX.

### 4. PERFORMANCE EVALUATION OF A RAKE RECEIVER BASED ON THE STORED CHANNEL MODELS

In this chapter, a practical example in using the stored channel models for link-level simulations is implemented. Particularly, performance of the Rake receiver was investigated using the developed stored channel models.

#### A. Rake receiver

The Rake receiver is designed to combat the effects of multipath fading. The receiver utilizes correlation between the received signal and template waveform, and finds peaks to collect the energy from different Multi Path Components (MPCs) so that receiving SNR improvement is attained. An all Rake (ARake) receiver utilizes all the output from the correlators so that it can perfectly extract received energy. However, because of power consumption and design complexity of the hardware, the implementation of ARake receivers are impractical [5]. Thus, a selective Rake (SRake), a compromise between improvement of SNR and hardware complexity by using only the subset of taps with strong energy, is often used instead. It can achieve reasonable improvement of SNR with less hardware complexity compared to the ARake receiver. We will consider SRake for the subsequent analyses.

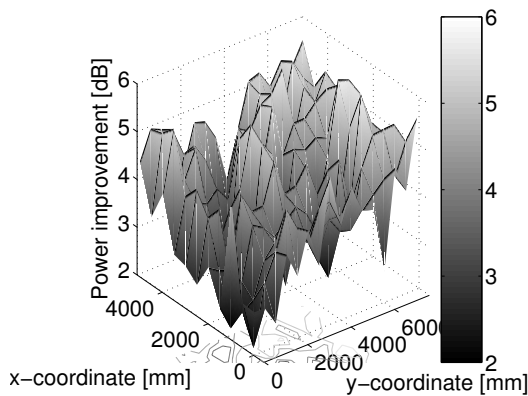


**Fig. 8:** Spatial distribution of the minimum power improvement when a 8-finger SRake receiver is applied

### B. Results and discussion

It is important to choose an appropriate number of Rake fingers to meet both performance and complexity requirements. First, in Fig. 7, we showed the cumulative distribution of the improved power in an array when the number of Rake fingers varied from 2 to 20. It can be seen from the figure that the improvement of the received power significantly changes until 8-finger SRake receiver were used, but the improvement was gradually becoming less when the number of Rake fingers exceeded 8. The improvement reaches 4 dB on average when 8-fingers were used. Thus, we can set the optimum number of Rake fingers to 8, and subsequent analyses were done with 8 fingers.

The improvement of the received power when using an 8-finger Rake receiver is shown in Fig. 8. The farther the distance between TX and RX antennas was, the higher the power could be improved. This was due to the power composition between the strongest MPC and scattered MPCs. When the RX antenna located near the TX antenna, the strongest wave dominated the received power. On the other hand, power contribution from the strongest wave was less remarkable when the RX antenna was far from the TX antenna. Therefore, the power did not improve much when the strongest wave was much stronger than the other waves, i.e., when the distance between antennas was small.

## 5. CONCLUSION

This paper first verified the effectiveness of stored channel simulations. Thus, the stored channel simulations can be used to replace the use of actual devices, which has a great contribution in the reduction of cost in developing new products.

Second, the store channel models have been developed in an indoor office environment. The important propagation parameters have been extracted from this measured data and their distributions in the area have been investigated. We noticed that all of these parameters are strongly dependent on the distance between TX and RX antennas. The result can also help to predict the outage performance inside this room.

Last, the performance of SRake receiver has been evaluated based on the stored channel model. The improvement of receiving signal-to-noise ratio was discussed. The number of Rake fingers was optimized to be 8. It was also found that similarly to the propagation parameters, the distance between TX and RX antennas is a factor that affects these characteristics the most.

## REFERENCES

- [1] A. F. Molisch, "Ultrawideband propagation channels-theory, measurement, and modeling," *IEEE Trans. on Vehic. Technol.*, Vol. 54, No. 5, pp. 1528-1545, Sep. 2005.
- [2] J. Foerster et al., "Channel modeling sub-committee report (final)," IEEE P802.15-02/490r1-SG3a, 2003.
- [3] A. F. Molisch et al., "IEEE 802.15.4a channel model – final report," IEEE P802.15-04/662r0-SG4a, 2004.
- [4] A. F. Molisch, *Wireless Communications*, 1-st edition, John Wiley & Sons, Chichester, 2005.
- [5] M. Z. Win and R. A. Scholtz, "Characterization of ultra-wide bandwidth wireless indoor channels: a communication-theoretic view," *IEEE J. Selected Areas Commun.*, Vol. 20, No. 9, pp. 1613-1627, Dec. 2002.
- [6] <http://ultra.usc.edu/uwb/database/>
- [7] Y. Rikuta, S. Fujita, F. Ohkubo, H. Hosoya, K. Hamaguchi, J. Takada, T. Kobayashi, "Indoor Channel Measurement of 26 GHz Band UWB Communication System," in *Proc. IEEE International Conference on Ultra-Wideband 2006 (ICUWB 2006)*, T2B-4, Waltham, USA, Sep. 2006.
- [8] K. Takizawa, I. Nishiyama and Y. Rikuta, "Experimental evaluation of various UWB signaling by using a UWB test bed," in *Proc. Technical Committee on Wideband System*, WBS2004-8, pp. 37-42, Shizuoka, Japan, 2004 (In Japanese).

# Numerical simulation on Temperature Field for Newtonian Fluid Enclosed in Concentric Sphere

05M18171    Bian Hu    Supervisor: Yoshihiro MOCHIMARU

## 同心二重球殻内のニュートン流体温度場シミュレーション 辺 虎

ニュートン流体でエネルギー式に対象を絞り、三次元空間場の数値解析をスペクトル差分法によって行う。同心二重球殻内の流体内の熱対流を伴う温度場を研究対象とし、レイノルズ数、プラントル数等のパラメータの影響及び強制速度を与えたマクロ的対流の影響による温度場の差異を把握した。

### INTRODUCTION

In engineering fields a variety of heat convection phenomena are treated, e.g., in the field of air conditioning design in an airplane, and of design of electronic device cooling, or of design of light equipment[1]. As an example, if the fluid enclosed in concentric sphere possesses a non-uniform temperature field, natural convection will be produced.

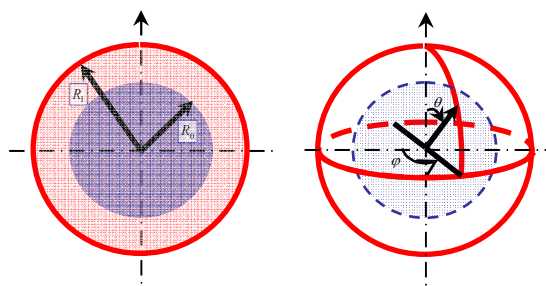


Fig.1 Model

In the current study, attention is focused on the energy equation itself for Newtonian fluid in a three-dimensional sphere, analyzed with the aid of a spectral finite

difference scheme. Effects of a Rayleigh number, a Prandtl number, and a convection flow on a temperature field are discussed.

In analysis, spherical harmonic functions are introduced as a base for spectral decomposition to discretize the equation in a finite difference scheme.

### ANALYSIS

#### Basic Equations

It is assumed that the fluid is Newtonian and possessing constant thermal conductivity, constant viscosity, and a constant coefficient of thermal expansion. No slip conditions on the walls apply. Dissipation terms are neglected. Thus, the system of equations[2] [3](continuity, momentum, energy) are:

$$\nabla \cdot \mathbf{u} = 0 \quad (1)$$

$$\frac{D\mathbf{u}}{D\tau} = -\nabla P + \frac{1}{Re} \nabla^2 \mathbf{u} + \mathbf{e}_r \frac{Gr}{Re^2} T \quad (2)$$

$$\frac{DT}{D\tau} = \frac{1}{PrRe} \nabla^2 T \quad (3)$$



### A Spherical Harmonic Function

A spherical harmonic function used is a function of two arguments,  $\theta$  and  $\varphi$ , connected to Legendre polynomials mathematically. That is[4],

$$Y_{n,m}(\theta, \varphi) = \sqrt{\frac{2n+1}{4\pi} \frac{(n-m)!}{(n+m)!}} P_n^m(\cos\theta) e^{im\varphi} \quad (4)$$

Orthogonality gives

$$\int_{\varphi=0}^{2\pi} \int_{\theta=0}^{\pi} \sin\theta P_n^m(\cos\theta) P_N^m(\cos\theta) d\theta d\varphi = \begin{cases} 0 & [n \neq N] \\ 4\pi(n+m)! / (n-m)!(2n+1) & [n = N] \end{cases} \quad (5)$$

$$\int_0^{2\pi} d\varphi \int_0^{\pi} Y_{n,m}^*(\theta, \varphi) Y_{n,m}(\theta, \varphi) \sin\theta d\theta = 1 \quad (6)$$

where the superscript \* stands for a conjugate. spectral decomposition is as follows

$$T(R, \theta, \varphi) = \sum_{n=0}^{\infty} \sum_{m=-n}^n T_{n,m}(R) Y_{n,m}(\theta, \varphi) \quad (7)$$

### Decomposition of the energy equation

Substituting Eq.(7) into Eq.(3) with the aid of Eqs.(5) and (6) gives

$$\frac{\partial T_{n,m}(R)}{\partial \tau} - \frac{1}{PrRe} \left[ \frac{1}{R^2} \frac{\partial}{\partial R} \left( R^2 \frac{\partial T_{n,m}(R)}{\partial R} \right) - \frac{n(n+1)}{R^2} T_{n,m}(R) \right] = - \iint \left\{ U \frac{\partial T}{\partial R} + \frac{V}{R} \frac{\partial T}{\partial \theta} + \frac{W}{R \sin\theta} \frac{\partial T}{\partial \varphi} \right\} Y_{n,m}^*(\theta, \varphi) \sin\theta d\theta d\varphi \quad (8)$$

where  $U, V$  and,  $W$  stand for velocity

components in the  $R$ -,  $\theta$ - and  $\varphi$ -directions respectively.

### **BOUNDARY CONDITIONS**

The following thermal boundary Dirichlet condition apply:

$$T_0(R = R_0) = 0 \quad (9)$$

$$T_H(R = R_1) = \sin\theta \times (\sin\theta + 0.8 \cos\varphi + 1) \quad (10)$$

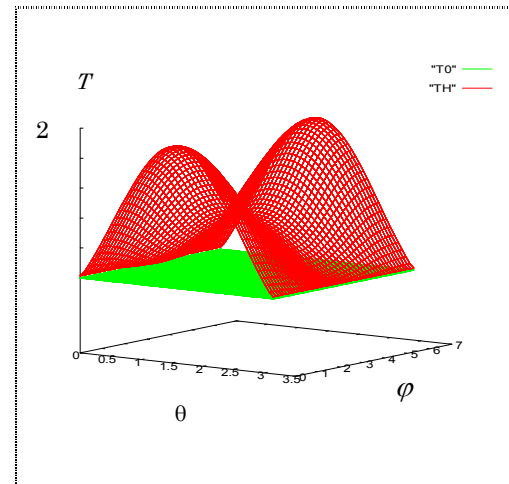


**Fig.2. Temperature distribution on the surface**

For forced flow velocity

$$U = 0 ; \quad V = 0 ; \quad (11)$$

$$W = \sin\theta \times (0.05 + 0.3 \cos\varphi) \quad (12)$$

### **RESULTS OF NUMERICAL ANALYSIS**

In this study, effects of the forced flow on thermal fields are clarified.

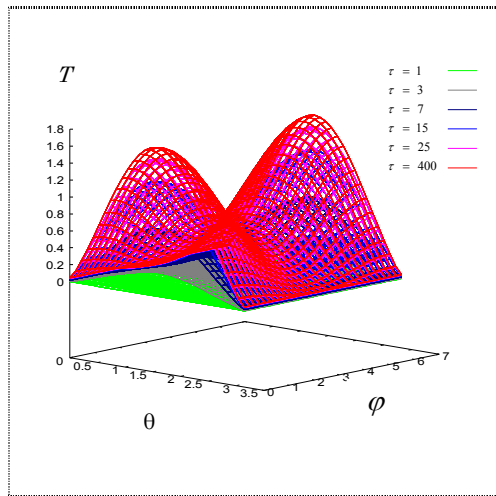


Fig3. Temperature development with time

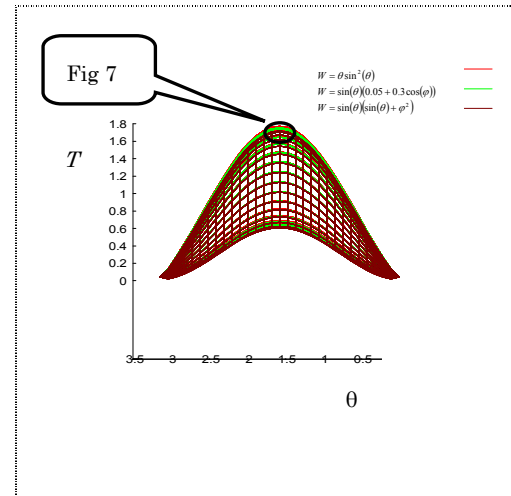


Fig6. Temperature difference with flow velocity at  $R = (R_1 + R_0)/2$

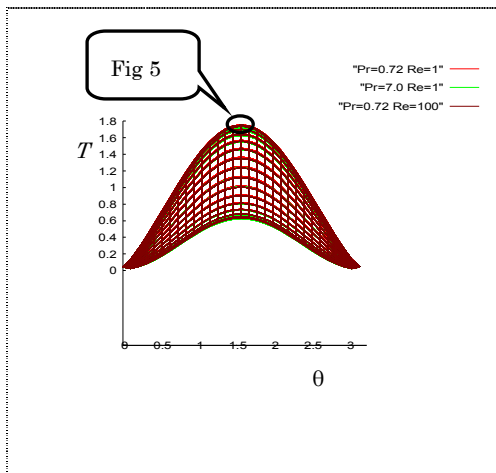


Fig.4 Temperature difference with Parameters at  $R = (R_1 + R_0)/2$

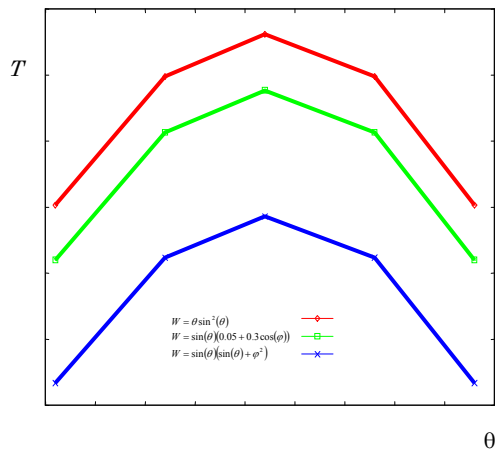


Fig.7 Expansion of temperature field

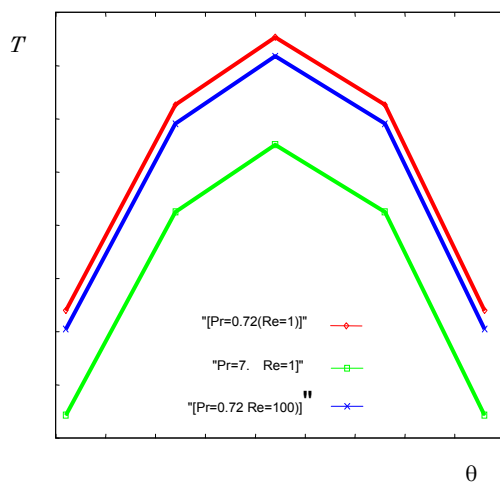


Fig.5 Expansion of temperature field

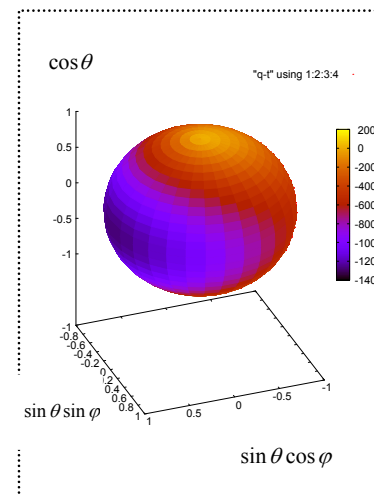
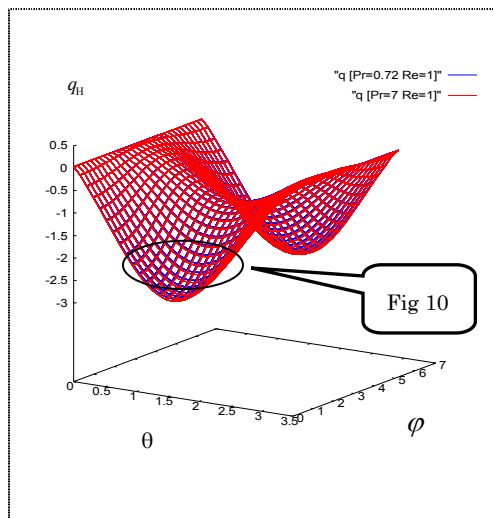
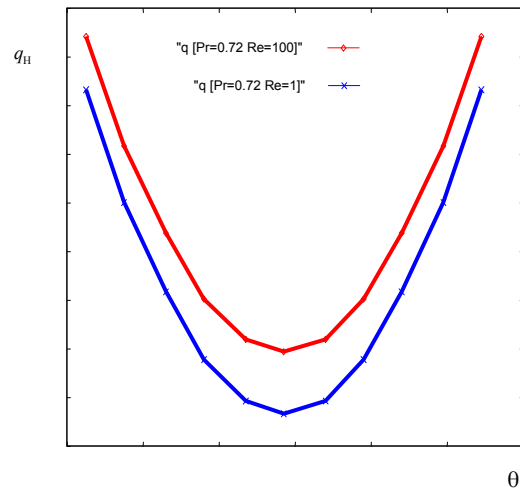


Fig.8 Heat flux distribution on the outer surface



**Fig.9 Heat flux difference with Pr**



**Fig.12 Expansion of temperature field**

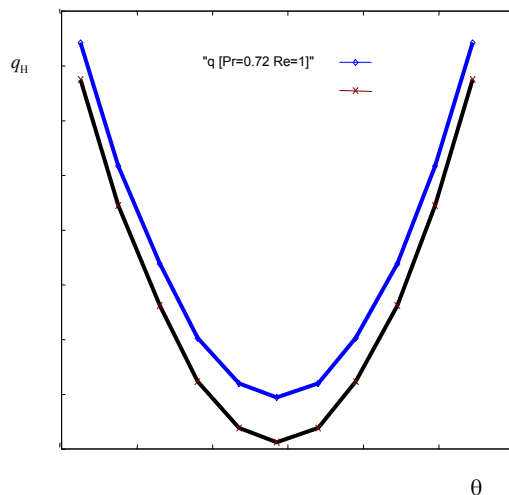


**Fig.10 Expansion of Heat flux**

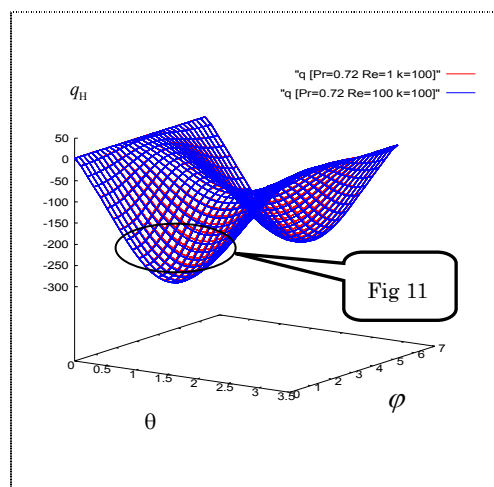


**Fig.11 Heat flux difference with Re**

## CONCLUSIONS

It is found that a spectral finite difference scheme can be applied at least to one case of a three-dimensional thermal field with a prescribed convective flow for a variety of combination of parameters.

## REFERENCES

- [1] Chung-Hyo JUNG, Takahiko TANAHAS-HI, "FEM Analysis of the Thermal Fluid Flows under Coriolis Force and Lorentz Force", 2003, Transactions of JSCES, pp.1-2
- [2] Tetsuya Kawamura, "Application of simulation of a flow", SANKAIDO, 2005.
- [3] Frank M.White, "VISCOUS FLUID FLOW", 1991, McGRAW-HILL, Inc
- [4] Kiyosato Okamoto, "The prospects of Fourier analysis", Asakura Bookstore, 1997

# A Study on Corrosion of Paint-Coated Steel with Defects in Marine Environment

Student Number: 05M18188 Name: Aung Kyaw Min Supervisor: Nobuaki OTSUKI

海洋環境下における塗装鋼材の欠陥の腐食メカニズムに関する研究

アウン・チャー・ミン

現在、港湾構造物においては塗装された鋼材が建設材料として使用される場合がある。このような構造物の耐久性を議論する場合、塩化物イオンによる鋼材の腐食が重要となる。特に、このような塗装鋼材の腐食は施工時あるいは供用時に生じる欠陥部を起点として進行する場合が多い。しかしながら、その速度やメカニズムは不明確である。そこで、本研究では、①鋼材表面におけるマクロセル腐食及びミクロセル腐食の評価手法の提案、②塗装した鋼材の欠陥部の腐食メカニズムの検討、③欠陥部の腐食に与える温度や暴露状況の影響に関する検討、④実構造物における腐食状況の検証を行った。

## 1. Introduction

The steel structures such as in bridges, expressways and port structures are usually exposed to aggressive environments like marine environment that promotes chloride attack. Therefore, without provision of paint coating as protection, the design life of the steel structures will not reach. There are two main corrosion protection mechanisms of paint coating such as (1) preventing the access of corrosion generative substances ( $\text{Cl}^-$ ,  $\text{H}_2\text{O}$ ,  $\text{O}_2$ ) to the steel and (2) providing the high resistant media between cathode and anode area in the formation of corrosion cell on the steel surface. However, still severe corrosion in paint coated steel structures is common in our daily life because corrosion generative substances find ways to reach the steel through the defects on the paint coating or through the deteriorated paint coating. Once the corrosion generating substances reaches the steel and the onset of corrosion process occur. After the corrosion at the paint defects is generated, the proceeding process of corrosion is controlled or accelerated by some influencing factors namely exposure situations and temperature. Nowadays, the corrosion in those paint coated steel structures becomes a serious problem from the durability of infrastructures point of views. Unfortunately, there are only a few studies related to above matter.

From those backgrounds, the objectives of this study became as follow: (1) to propose the divided steel plate evaluation method for detailed investigation of macrocell & microcell corrosion of the steel plate (2) to investigate corrosion mechanism of paint-coated steel with defects exposed to marine environment (3) to investigate the influences of exposure situations and temperature on the corrosion and (4) to propose the estimation method for macrocell corrosion rate in existing structures.

## 2. Outline of experiment

In this section, the outline of the experiments for the study is presented.

### 2.1 Materials used and Manufacturing of Specimens

In this study, mainly two types of specimens were used, divided and undivided steel plates. The divided steel plate was made by connecting 9 steel elements each having a dimension of 1cm x 1cm x 0.5cm with epoxy in the spacing of 0.1cm to form a 3cm x 3cm divided steel plate as shown in Fig. 1. Four lead wires

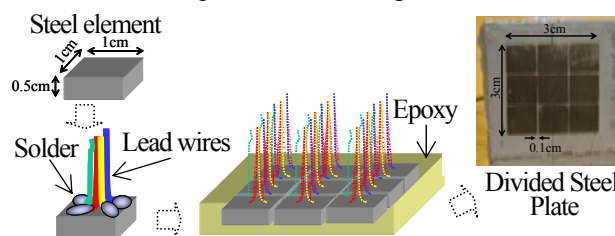


**Fig.1 Outline of Divided Steel Plate**

were connected separately to each steel element by soldering to allow the measurement of corrosion current between each steel element [1]. The surface of divided steel plate was then polished to obtain a smooth and level surface. Moreover, undivided steel plates having the same size and made up of the same material was prepared to do a comparative study between divided and undivided steel plates. All the specimens were brush painted with the paint (JIS-5621 standards oil alkyd resin base paint) for general corrosion except the specimens used for proposing the divided steel plate. The paint condition was set into two types good and poor conditions mainly by means of thickness of paint. The paint coating thickness are (138~188  $\mu\text{m}$ ) for good paint and (45~65  $\mu\text{m}$ ) for poor paint.

## 2.2 Experimental Set Up

### (1) Proposal of Divided Steel Plate

In this experiment, the bare divided and undivided steel plates were submerged in 3%NaCl solution under the same condition. The specimens were submerged in 3%NaCl solution to simulate the marine environment. The corrosion polarization behavior of those two steel plates was compared every week until 1-month.

### (2) Investigation of the corrosion mechanism of paint-coated steel plate with defects

In order to investigate the corrosion mechanism of paint-coated steel plate with defects, the painted divided steel plates with different types of defect (unpainted part) in middle steel element were submerged in 3%NaCl solution. The details of defect types were as shown in **Fig.2**. Then, the corrosion behavior of the specimens was investigated every month until 4-months.

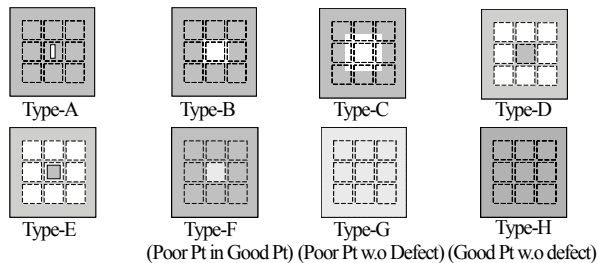


**Fig.2 Painted Divided Steel Plates with defects**

### (3) Investigation of Influences of Exposure Situations

In this experiment, the type-B specimens were exposed to different exposure situations such as vacuum, submerged, air-bubble (near), air-bubble (far), wet/dry and atmosphere situations. In vacuum (simulation of deep submerged situation) situation, the dissolved oxygen (D.O) in 3%NaCl solution was reduced under 1.0mg/l by using vacuum pump and the specimens were exposed in low D.O content 3%NaCl solution. In air-bubble near & far (simulation of direct and indirect wave zone situation) situations, the air-bubble was supplied into the solution near/far (from-15cm) to the specimens surface in the rate of 10cm<sup>3</sup>/sec by using Suisaku Company made SSPP-7 air pump. In wet/dry situation, the specimens were exposed in 3%NaCl solution same as the submerged situation for 1-day (wet situation) and removed the solution and put in environmental control chamber for 1-day (dry situation). For the atmosphere situation, the specimens were sprayed with 3%NaCl everyday and put in environmental control chamber. The temperature was controlled at 20°C to reduce the effect of temperature on the corrosion. Then, the corrosion behavior of the specimens was investigated every month until 4-months.

### (4) Investigation of Influences of Temperature

In this experiment, The solution temperature was controlled at (20, 30, 40°C) for the cases such as submerged, air-bubble near & far and wet condition of wet/dry situation by using automatic heater. In the cases of atmospheric and dry condition of wet/dry situation, the specimens were put in the environmental control chamber and set the temperature at 20,30 and 40°C. Then the

corrosion behavior of the specimens was investigated every month until 4-months

## 2.3 Investigation Items

### (1) Polarization Behavior

The factors expressing polarization behavior such as halfcell potential and polarization resistance were measured by using the Riken Denshi Co., Ltd made CT-7 corrosion monitor.

### (2) Macrocell Corrosion Rate

The macrocell corrosion current was measured between the middle steel element and the surrounding steel elements by using zero resistance ammeters. Then the macrocell current density can be calculated by using Equation (2-1). The macrocell current density can be converted into the macrocell corrosion rate by using conversion factor ( 100  $\mu$  A/cm<sup>2</sup> = 1.16 mm/year) [1].

$$I_{mac} = \frac{I_{in} - I_{out}}{S} \quad (2-1)$$

where,  $I_{mac}$  : macrocell corrosion current density (A/cm<sup>2</sup>)  
 $I_{in}$  : total current flowing in (A)  
 $I_{out}$  : total current flowing out (A)  
 $S$  : surface area of steel

### (2) Microcell corrosion rate

The microcell corrosion current density can be calculated by substituting polarization resistance in the equation (2-2). Finally, microcell corrosion rate can be calculated by using the conversion factor (100  $\mu$  A/cm<sup>2</sup> = 1.16 mm/year).

$$I_{micro} = \frac{K}{R_p S} \quad (2-2)$$

where,  $I_{micro}$  : microcell corrosion current density (A/cm<sup>2</sup>)  
 $K$  : constant (=0.0209V) [2]  
 $R_p$  : polarization resistance ( $\Omega$ )  
 $S$  : surface area of component (cm<sup>2</sup>)

### (3) Calculation of steel mass loss by corrosion

First, the corrosion rate measured at each month was transformed to (g/cm<sup>2</sup>/year). Then, the steel mass loss at each month by macrocell & microcell corrosion was calculated as flows:

$$\text{Corrosion Rate (g/cm}^2\text{/year)} \times \text{Time (1/12yr)} = \text{Mass Loss (g/cm}^2\text{)}$$

Finally, the steel mass loss until 4-months was calculated by summation of mass loss at each month.

## 3. Results and Discussion

### (1) Proposal of Divided Steel Plate

The average halfcell potential and polarization resistance at different measurement points on the surface of divided and undivided steel plates were determined and compared until 4weeks as shown in **Fig.5**. From the results, it was confirmed that the halfcell potential and polarization resistance of the divided steel plate was almost the same as that of undivided steel plate and indicated that the possibility and formation of corrosion reaction on the divided steel plate was same as that of undivided steel plate [3]. Therefore, it can be concluded that the divided steel plate can be used to investigate the corrosion behavior of undivided or normal steel plate and, the proposal of divided steel plate evaluation method for macrocell corrosion of the steel plate was successfully proposed.

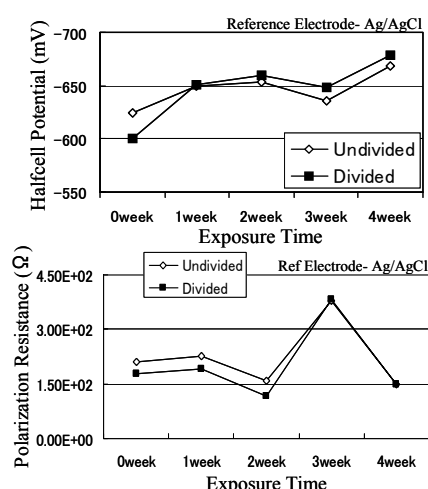


**Fig.5** Halfcell Potential & Polarization Resistance of Divided & Undivided Steel Plate

(2) Investigation of the corrosion behavior of paint-coated steel with defects

The macrocell corrosion current density between the defect and paint part of the specimen type A & B are as shown in **Fig.6**. From the results, it was confirmed that macrocell corrosion occurred at the defect part and, the defect acted as anode and the paint part acted as cathode. Then the paint part became anode as the macrocell corrosion extended to the surrounding. The other specimens had the same trend. In type-F specimen, macrocell corrosion was also detected between good and poor paint parts while poor paint part acted as anode and good paint as cathode. Almost no macrocell corrosion occurred in the case of paint coating without defect (Type-G & H). Therefore, it can be said that the defect part in the paint coating was the main cause of macrocell corrosion.

Moreover, the microcell corrosion current density of type- A & B specimens is as shown in **Fig.7**. From the results, it

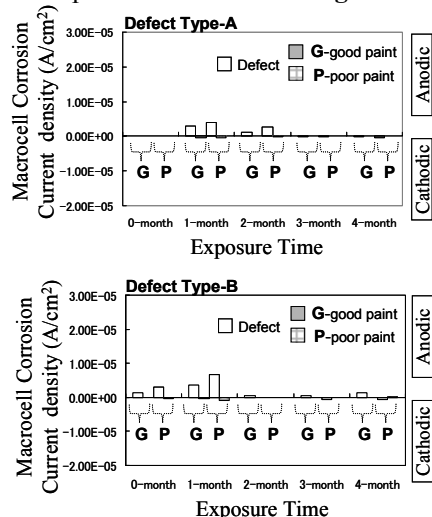


**Fig.6** Macrocell Corrosion Current Density of the Specimens was confirmed that microcell corrosion mainly occurred at defect until 1-month and it spread to the surroundings after the surrounding paint part degraded due to the cathode reaction of

macrocell corrosion in 0-month & 1-month. The same trend was observed in all other specimens. Therefore, it can be concluded that macrocell and microcell corrosion had a relation and the defect was the major cause of both corrosions of the paint-coated steel plate.

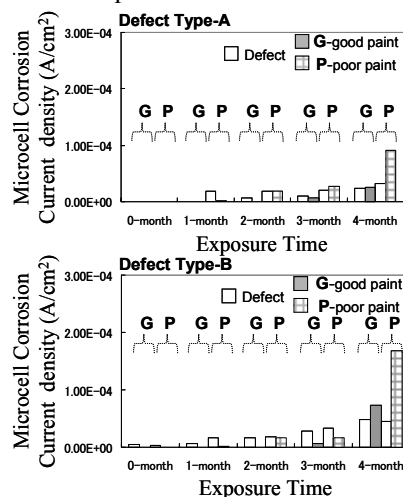
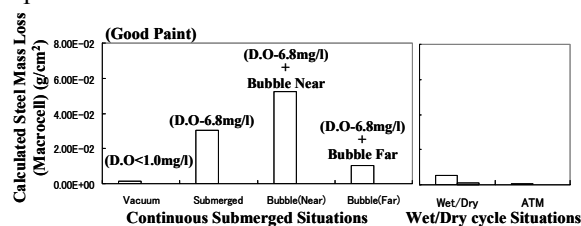


**Fig.7** Microcell Corrosion Current Density of the Specimens

(3) Investigation of Exposure Situations and Temperature

The calculated steel mass loss by macrocell and microcell of the good painted type-B specimen are as shown in **Fig.8**. From the results, it was confirmed that the calculated steel mass loss in the specimens by macrocell and microcell corrosion was influenced by exposure situations. The key factors for influence of exposure situation were the dissolved oxygen content in the solution and surface wetness condition. The vacuum situation with the low D.O content gave the lowest calculated steel mass loss by macrocell and microcell corrosion. The air-bubble (near) situation which had high D.O content (6.8 mg/l) in addition with air-bubble near to the specimens gave the highest steel mass loss by macrocell corrosion and second highest steel mass loss by microcell corrosion. Although the wet/dry situation showed the highest calculated steel mass loss by microcell corrosion, its macrocell corrosion was very low when it was dry. Therefore it can be concluded that the air-bubble (near) situation was the most severe exposure situation for macrocell and microcell corrosion for paint-coated steel.

In order to investigate the influence of temperature, the calculated mass loss by macrocell and microcell corrosion under air-bubble (near) by wet/dry situations at different temperature are compared as shown in **Fig.9**. From the results, it was confirmed that the higher the temperature the higher the calculated steel mass loss by macrocell and microcell corrosion. In the case of the submerged situation, the higher the temperature the lower the D.O content led to lower macrocell





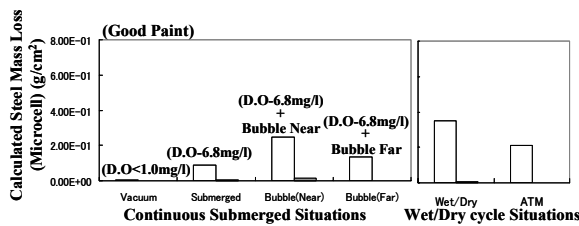


**Fig.8** Calculated Steel Mass Loss by Macrocell & Microcell

Corrosion under Different Exposure Situations and microcell corrosion. From the results, it can be said that the air-bubble near situation at the high temperature was the most severe situation for the corrosion of paint-coated steel with defects.

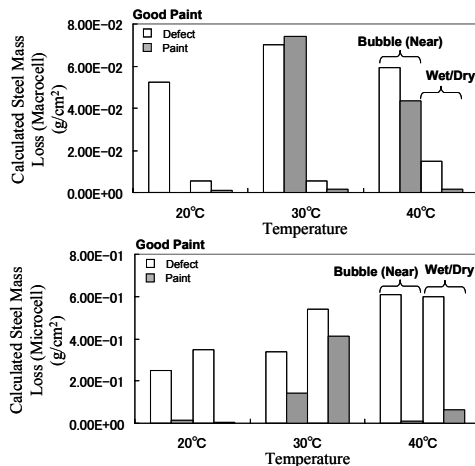


**Fig.9** Calculated Steel Mass Loss by Macrocell & Microcell  
Corrosion under Different Temperature

### (3) Proposal of Estimation Method for Macrocell Corrosion Rate of Existing Paint-Coated Structure

In order to calculate the macrocell corrosion current between individual parts of the steel plate, the circuit diagram was constructed on the steel plate as shown in **Fig.10**. Then the circuit analysis was done based on the Ohm's law ( $V=IR$ ) and

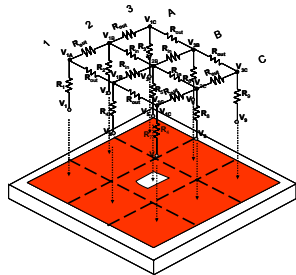
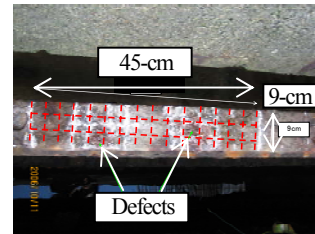


**Fig.10** Circuit Diagram on the Surface of Divided Steel Plate

Kirchhoff's current law (summation of current at any node is zero) [1] and the simultaneous equations were solved by using Mathematica 5.2 software. The input data for circuit analysis were halfcell potential, paint/solution resistance and polarization resistance. Finally the corrosion rate the existing painted structure was estimated by using the proposed method. The results of macrocell & microcell corrosion rate are as shown in **Fig.11**. The estimated results agreed with the

experiment results that the defect parts had the severe macrocell and microcell corrosion rates. It can be said that the corrosion rate of the existing structure was successfully estimated by using the proposed method.



Location - Yokosuka, Japan

Age - 30 Years

Structure - H-Beam

Exposure Situation - Wet/Dry

Paint - Tar Epoxy

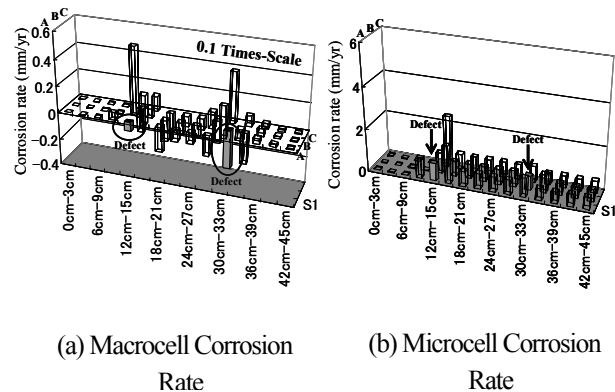


**Fig.11** Estimated Corrosion Rate of the existing Structure

## 4. Conclusions

- (1) The divided steel plate evaluation method for macrocell corrosion of the steel plate was successfully proposed.
- (2) It was confirmed that the macrocell corrosion occurred at the paint defect part, and the defect acted as anode and paint part acted as cathode. Also, the macrocell corrosion was the cause of for spreading of microcell corrosion to the surrounding paint part. The defect was the major cause of the corrosion of paint-coated steel.
- (3) It was confirmed that the exposure situations and temperature greatly influenced the corrosion of paint-coated steel with defects. The air-bubble (near) situations under higher temperature was the most severe condition for the corrosion.
- (4) The estimation method for macrocell corrosion rate of the existing painted structure was successfully proposed. The proposed method was successfully applied in existing structure.

## References

- [1] Miyazato, S., Otuski, N., Kimura, H., Estimation Method of Macrocell Corrosion Rate of Rebar in Existing Concrete Structures Using Non-destructive tests, East Asia-Pacific Conference (EASEC 8), 2, pp.531-542, 2001
- [2] Tsuru, T., Maeda, R., Haruyama, S., Applying of AC method monitor to local corrosion, Technique of Corrosion Prevention 28, pp.638-664, 1979
- [3] Fontana, M., Corrosion Engineering, McGraw-Hill, 1978

# Study on Antennas Embedded in Mobile Phone Housing

Student Number: 05M18194 Name: Jeonghoon HAN Supervisor: Jun-ichi TAKADA

## 筐体組み込み型携帯電話用アンテナの研究

韓 政勲

本研究では携帯電話内部にアンテナのためのスペースを確保する代わりに、薄型アンテナを筐体に組み込むことを提案する。一つの薄型アンテナにおいて2周波共振させることを第一目標とし、各帯域での帯域幅を確保することを第二目標とする。付加接地と切込みによりパッチ上の表面電流を調節することでアンテナの多共振化が図れるが、一方で切込みによる共振は帯域幅が狭く、これらの両立が難しいことが分かった。

## 1 Introduction

For last ten years we have noticed rapid development of wireless communications, especially mobile communications. While a market for fixed telephones is mature, one for mobile phone has still been increasing in developed and developing countries. The requirements of customer and the market of mobile phone cause that mobile phones are small sized and multifunction. These days, mobile phones are handy and have various functions including, for example, an MP3 player, a digital camera, a mobile analog/digital TV and so on. Thus, the circuit of mobile phone has been required to be more downsized and cheaper. This research is concerned with antennas for mobile phones to approach to the solution.

Half-wave dipole antennas are widely used for mobile phones. They have advantages of easy manufacture, low price, and good performance. However, they occupy wide space in the mobile phone and are protruded from the mobile phone housing. These characteristics can be restrictions in designing the mobile phones.

Low profile antennas, such as microstrip antennas (MSA), can solve the problems. They are so thin that they can be implemented in the mobile phones. These antennas are usually placed at an edge of mobile phone and are implemented on dielectric materials with high relative permittivity between 2.2 and 11. The usage of materials with high permittivity can increase the cost of antennas. They also occupy relatively inner space of mobile phones.

This paper proposes a new antenna for mobile phones. The antenna is proposed to be implemented in the mobile phone housing. In order to embed an antenna in the mobile phone housing, the antenna should be very thin. Thus, this research concentrates on MSA because MSA is the low profile antenna. A dielectric material for antenna is not used; even though a dielectric material is not used, there is a permittivity between the substrate and the antenna due to circuits interposed between them, although the equivalent permittivity to the circuits is not considered in this research. Embedding an antenna into mobile phone housing and using the air as the dielectric, it is expected that both the inner space of mobile phone and cost of antenna can be reduced. The complexity of manufacturing process for

Table 1: Operating frequencies of wireless communication systems

Systems	Operating frequency (Uplink and downlink:MHz)	Overall bandwidth (MHz) [Relative BW]
W-CDMA	1920 – 1980, 2110 – 2170	250 [12.2%]
PDC	940 – 956, 810 – 826	146 [16.5%]

mobile phone can be also relieved.

Table 1 shows the operating frequencies of some of the mobile communication systems. Various mobile communication systems are serviced and the bandwidths for them have become wide. Preferably, a mobile phone has the ability to adapt to multiple services. Therefore, the multi-band operation with sufficient bandwidths of small antennas has become a very important design issue.

## 1.1 Objectives

In this research, a new antenna has been designed for a specific model of mobile phones. The size of its upper housing is  $80 \times 50 \times 12 \text{ mm}^3$ . The size of its substrate is  $78 \times 48 \text{ mm}^2$ . The height between the substrate to the housing is 4.5 mm. Therefore, the maximum size of the antennas is restricted to  $78 \times 48 \times 4.5 \text{ mm}^3$ . The detail will be described at Chapter 2 and 3. Further, the mobile phone was assumed to satisfy two wireless communication services in Japan; PDC (810-956MHz) and W-CDMA (1920-2170MHz) bands. Preferably, a MSA should resonate at dual frequencies (around 885MHz and 2045MHz) and cover the PDC band (800MHz band) and the W-CDMA band (2000MHz band). This research focused on resonating a small sized MSA at dual frequency bands.

## 2 Microstrip Antennas (MSA)

The MSA was first proposed by Deschanps [1] in 1953. The MSA is an attractive candidate for the use in mobile communications. The basic geometry of the MSA is shown in Figure 1. The MSA provides advantages such



as low profile, light weight, low cost in manufacturing and various shaped surface. However, the disadvantage is its inherent narrow bandwidth of a few percent due to a high quality factor.

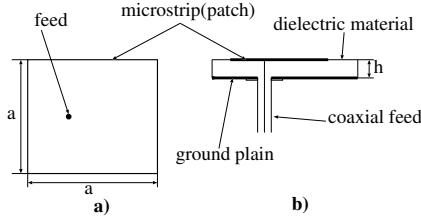


Figure 1: Microstrip Antenna a) top view b) side view

MSA can have various shapes. A rectangular MSA is one of the most commonly used MSA. The transmission line mode in their original forms is applicable to rectangular patches. It is impossible to adapt the transmission line model to other shapes than rectangle. In this thesis, an electromagnetic simulator is used. It is characterized by the patch area, its shape, the height of patch, permittivity of a dielectric material. A resonant frequency ( $f_r$ ) of a rectangular MSA can be obtained by the following formula[2]:

$$f_r = \frac{c}{2a_{\text{eff}}\sqrt{\epsilon_e}} \quad (1)$$

where

$$a_{\text{eff}} = a \left[ 1 + 0.824 \frac{h}{a} \frac{(\epsilon_e + 0.3)\{(a/h) + 0.262\}}{(\epsilon_e - 0.258)\{(a/h) + 0.813\}} \right], \quad (2)$$

$$\epsilon_e = \frac{\epsilon_r + 1}{2} + \frac{\epsilon_r - 1}{2} \left( 1 + 10 \frac{h}{a} \right)^{-\frac{1}{2}} \quad (3)$$

$f_r$  is a resonant frequency,  $c$  is the velocity of light,  $a_{\text{eff}}$  is an equivalent length,  $\epsilon_e$  is an effective permittivity, and  $h$  is a height between the ground and the patch.

Roughly, a resonant frequency of a rectangular MSA is inversely proportional to the size of patch. The length  $a$  of the patch is usually half-wavelength. Achievable relative bandwidth is known as a few percents.

## 2.1 Performance Evaluation of MSA

The MSA is a resonant device. Thus, its impedance varies more easily than its radiation pattern. The antenna impedance is related to the bandwidth of an antenna, which determines an operating frequency range of the antenna.

The bandwidth(BW) can be defined by a voltage standing wave ratio (VSWR) and a Q-factor of antenna as [4]:

$$BW = \frac{VSWR - 1}{Q\sqrt{VSWR}} \quad (4)$$

The Q-factor is defined as follow[3]

$$Q = \omega \frac{W_T}{P_t}, \quad (5)$$

where  $W_T$  is the peak energy stored, and  $P_t$  is the average power radiated.

Q-factor is inversely proportional to the bandwidth. Thus, lower Q indicates a broader bandwidth. Q-factor can be approximately expressed in terms of the input impedance of the antenna as [5]

$$Q = \omega_0 \frac{|Z'_0(\omega_0)|}{2R_0(\omega_0)}, \quad (6)$$

where  $\omega_0$  is the frequency at  $X(\omega_0) = 0$ ,  $Z_0(\omega)$  is the complex input impedance of the antenna,  $R_0(\omega)$  is the real part of  $Z_0(\omega)$ ,  $X_0(\omega_0)$  is the imaginary part of  $Z_0(\omega)$ , and  $Z'_0(\omega_0)$  is the derivative of  $Z_0(\omega_0)$  with respect to  $\omega$ .

The bandwidth can be determined by a frequency range in which return loss is below a certain level. The return loss is defined as the ratio of the reflected power to the incident power. The return loss is usually expressed in dB as shown in the Eq. (7). Typically, a return loss of less than  $-10\text{dB}$  and  $-15\text{dB}$  are often need, which correspond to  $VSWR=2$  and  $1.5$ , respectively. In this research, the bandwidths of antennas are basically evaluated in accordance with the return loss of less than  $-5\text{dB}$ . Thus, it is sufficient to evaluate the resonant frequencies and bandwidths of the antenna by the return loss.

$$\text{ReturnLoss[dB]} = 10\log_{10} \frac{\text{ReflectedPower}}{\text{IncidentPower}} \quad (7)$$

## 2.2 Dualband Structures

In order to accommodate two wireless communication services in a system, dualband antennas have been developed.

One of the dualband structure is a MSA with slots. By adding slots, it is possible to change the flows of current on the patch. Dualband structures are introduced in the L-slotted planar inverted-F antenna (PIFA) [6], the PIFA with H-type slit [7], and so on.

Another dualband structure is a MSA having electrical shorting pins. The shorting pin changes the input impedance of antenna. Thus, it is usually used for impedance matching of antennas. However, adding the shorting pins to antennas, it can also affect resonant frequencies of antennas. Generally, the structures having the shorting pin is used together with slots.

## 3 Simulation

Our objective is to develop a dualband antenna for the specific mobile phone. The requirement for an antenna is that the maximum patch size of the antennas is  $78 \times 48 \times 4.5 \text{ mm}^3$  as shown in Figure 2. An antenna is desirable to resonate around  $885\text{MHz}$  and  $2045\text{MHz}$ .

### 3.1 Effects of a sub-LCD window

The mobile phone under consideration has a sub-LCD window on a side of the upper housing. The space for the sub-LCD window should be prepared on the patch. The slot for the sub-LCD results in the antenna

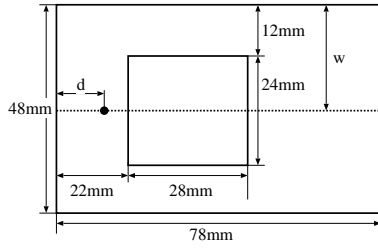


Figure 2: The schematic layout of the upper housing

impedance mismatching at ordinary feeding positions, which are generally on the center line of the patch in a rectangular MSA.

### 3.2 Design of Dualband Structure MSA

This section introduces the dual resonant structure of antennas. It is concentrated on the amendment of patch shape because other factors such as the thickness and permittivity of a dielectric material are restricted to the fixed values.

In the design of a dualband MSA, the following three steps were proposed. The first step is to find a preferable feeding position by moving the feed point. The second step is to match the impedance at a desired resonant frequency by adding electrical shorting plates. The lower design frequency of 885MHz is prior to the upper design frequency of 2045MHz because it is more difficult to resonate a small sized antenna at a low frequency. Finally, the current paths are controlled by slotting a part of the MSA. It is found that the desired dual resonant frequencies can be obtained by designing the MSA following the proposed design rule.

In the first step, the feed was moved on the patch. The feeding position for impedance matching is obtained at the right upper edge with  $d = 63\text{mm}$  and  $w = 6\text{mm}$ . However, its resonant frequency is 2398MHz. This is still high to the desired frequencies.

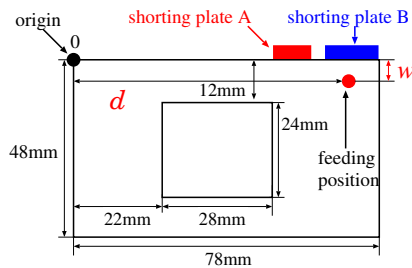


Figure 3: The positions of the shorting plates and the feed

In the second step, the additional shorting plates are provided to resonate the antenna at a desired frequency. The shorting plates were added on the edges. The interesting results were obtained in the case of two shorting plates. One plate was located at  $d = 50\text{mm}$  and  $w = 0\text{mm}$  with its size  $10 \times 4.5\text{mm}^2$  (shorting plate A), and another was placed at  $d = 63\text{mm}$  and  $w = 0\text{mm}$

with the size of the plate  $15 \times 4.5\text{mm}^2$  (shorting plate B). Resonant frequencies at the 800-900MHz were seldom obtained due to the inherent structure of the antenna, i.e. the sub-LCD window and the fixed height. The poor resonance at the lower band was obtained by adding a shorting plate. The antenna with the shorting plate A resonates 820MHz and 2689MHz. The former resonant frequency was closest to the lower design frequency. However, its return loss at the frequency could not satisfy the reference value. On the other hand, the antenna with the shorting plate B resonates at 739MHz and 2689MHz. And the antenna with the shorting plate B has better impedance matching than the antenna with the shorting plate A. These advantages of each shorting plate can be combined by the combination of the shorting plates. Using the combination of the shorting plates, the advantages of the shorting plates A and B could be obtained. The resonant frequencies are 864MHz and 1833MHz. Blue line in Figure 8 indicates the return loss of the antenna with the combination of shorting plates A and B. The resonant frequencies are closer to the design frequencies (885MHz and 2045MHz).

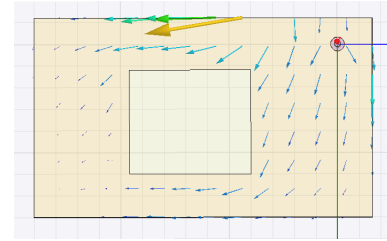


Figure 4: The currents on the patch at 864MHz in the antenna presented in Fig. 3 (length of the arrow corresponds to magnitude)

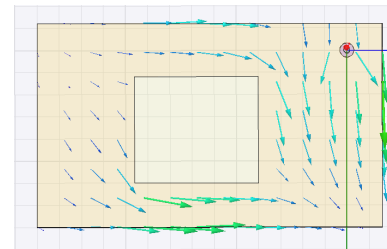


Figure 5: The currents on the patch at 1833MHz in the antenna presented in Fig. 3 (length of the arrow corresponds to magnitude)

The third step is to control current paths by slotting a part of the MSA such that the desired dual resonant frequencies are obtained. In the antenna with both of the shorting plates, the current paths at 864MHz are two ways as shown in Figure 4. One is from the feed to the left upper edge. Another is from the feed to the lower side, as turning at the sub-LCD window. The current does not reach the left lower edge. The current at 1833MHz started at the left upper edge and the feed in Figure 5. The current finally flows to the right lower edge. To raise the upper resonant frequency with-

out changing the lower resonant frequency, an edge of patch is cut out. Red line in Figure 8 indicates the return loss of the antenna whose the right lower edge is cut out. And their current paths are shown in Figure 6 and 7. As expected, cutting the right lower edge affected the upper resonant frequency because the current at the upper resonant frequency flows to the right lower edge; it does hardly effect the lower resonant frequency, because the current at the lower resonant frequency seldom flow at the right lower edge. The upper resonant frequency was shifted by 198MHz, whereas the lower resonant frequency was shifted by 7MHz. Thus, dual resonant frequencies at 871MHz and 2031MHz were obtained.

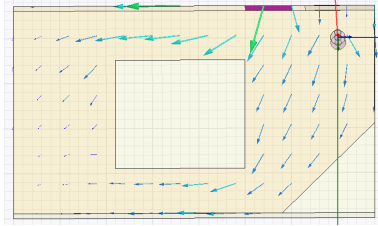


Figure 6: The currents on the patch at 871MHz of the antenna presented in Fig. 3 (length of the arrow corresponds to magnitude)

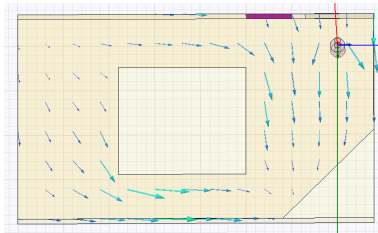


Figure 7: The currents on the patch at 2031MHz of the antenna presented in Fig. 3 (length of the arrow corresponds to magnitude)

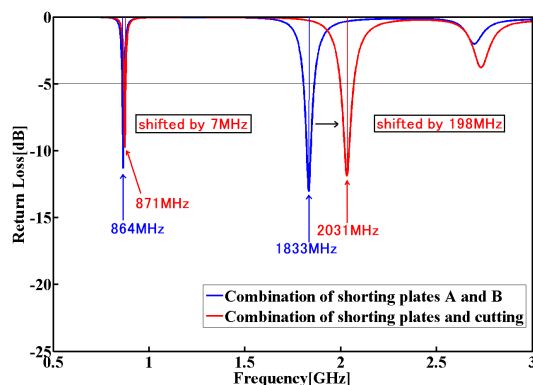


Figure 8: The Return losses of antennas

## 4 Conclusion

This paper proposed a new antenna for mobile phones, an antenna embedded in mobile phone housing. The resonant frequencies at the expected bands were obtained by designing the MSA following the established design rule. Further, antennas having various slots were simulated. However, the bandwidths could not be satisfied. The restrictions imposed by the specifications of the mobile phone housing, such as the ones for the dimension of the patch, and the thickness and permittivity of the dielectric material, are huge obstacles to enhance the bandwidths. In order to achieve the antenna embedded in the mobile phone housing, research on enhancement of bandwidths should be performed without changing the thickness and permittivity of the dielectric material.

## References

- [1] G.A. Deschanps, "Microstrip microwave antennas," 3rd USAR Symposium on Antennas, 1953.
- [2] M. Haneishi, K. Hirasawa, and Y. Suzuki, Compact and Plain Antennas, Tokyo, Japan, IEICE, 1996.
- [3] N. Inagaki, N. Kikuma, and K. Isobe, "Size Reduction of an Inverted F Type Antenna," Technical Report of IEICE, A.P89-27, pp47-52, 1989.
- [4] J.R. James and P.S. Hall, Handbook of Microstrip Antennas, London, United Kingdom, Peter Peregrinus Ltd., 1989.
- [5] D. Yaghjian and Steven R. Best, "Impedance, Bandwidth, and Q of Antennas," IEEE Trans. on Antennas and Propagation, Vol.53, No. 4, pp1298-1324, April 2005.
- [6] C. W. Chiu and F. L. Lin, "Compact dual-band PIFA with multi-resonators," Electronics Letters, Vol.39, No. 12, pp538-540, June 2002.
- [7] Young-hun Lee, "Dual-band FIFa design for mobile phones using H-type slit," IEEE, pp3111-3114, March 2004.